

5

Instrumentation for pulsar observations

Pulsar observations place higher demands on data acquisition systems than most other astronomical observations. High time resolution is necessary to search for millisecond and rapidly rotating pulsars (Chapter 6), to resolve microsecond and nanosecond scale structure in individual pulses (Chapter 7) and to obtain high-precision arrival times (Chapter 8). Since pulsars are generally weak sources, observations covering a wide bandwidth are desirable to maximise sensitivity. As discussed in Chapter 4, the frequency-dependent refractive index of the interstellar medium means that pulses emitted at higher radio frequencies travel faster and arrive earlier than those emitted at lower frequencies. For a finite receiver bandwidth, this dispersion process broadens the pulse so that its signal to noise ratio (S/N) is reduced. Frequency resolution therefore is vital to combat the effects of dispersion. We distinguish between two main approaches to de-dispersion: (a) incoherent devices (filterbanks and correlators) where the phase content of the signal is not recorded; (b) coherent devices (baseband recorders and coherent de-dispersers) which make full use of the incoming signal to properly recover the true pulse shape.

5.1 Example observational set-up

Before discussing the various devices for dispersion removal, we begin with an overview of the signal path from the reception of raw voltages by the telescope to the input of a signal into a data acquisition device. The example shown in Figure 5.1 contains all the essential elements used in single dish pulsar observations discussed here.

After being brought to a focus by the antenna, the radiation is sampled

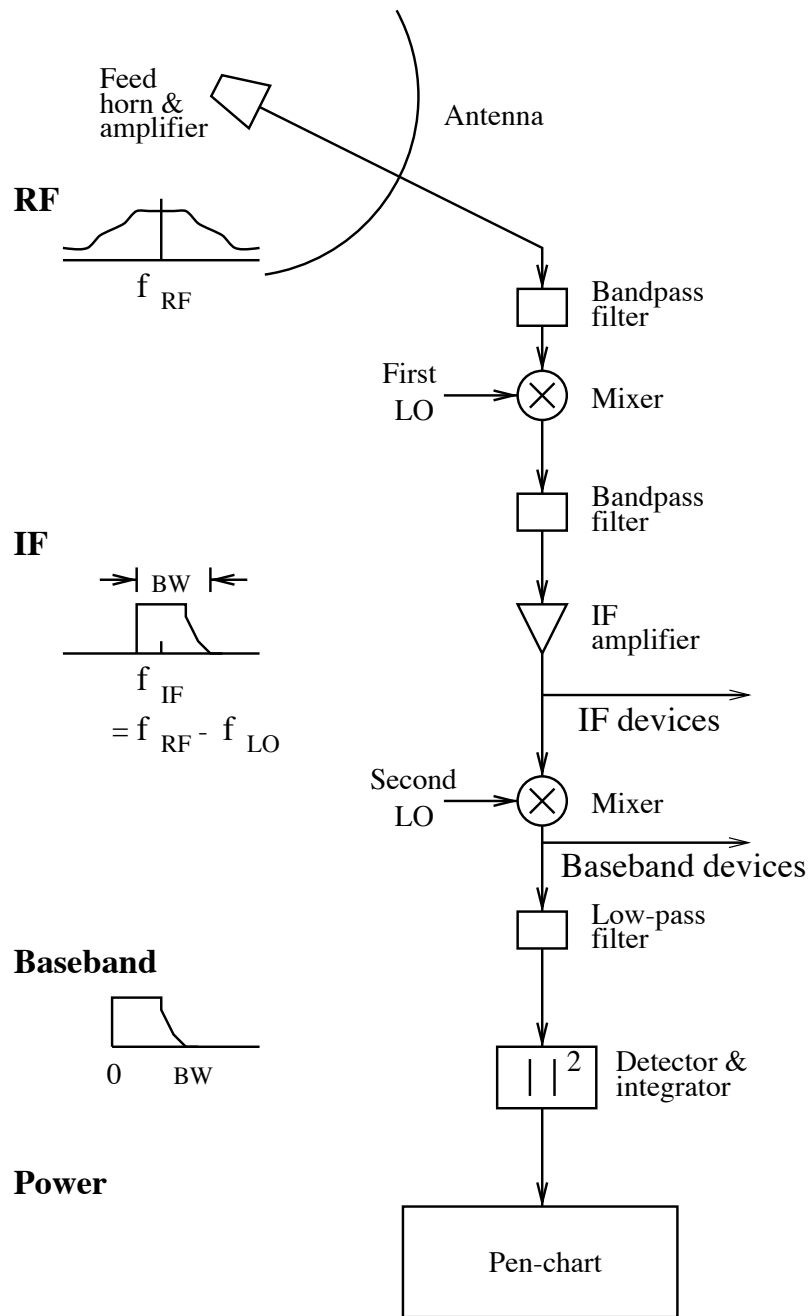


Fig. 5.1. Schematic showing the signal path in a single-dish radio telescope. See text for a discussion of the various stages. Figure adapted from an original version (Bhattacharya 1998) provided by Dipankar Bhattacharya.

by a wave-guide *feed*, usually having two receptors that sample orthogonal senses of polarisation, usually dual linear or dual circular (see Appendix 1). We refer, throughout this chapter, to these orthogonal inputs as *polarisation channels*, and in illustrations show the signal path from just a single channel. The weak radio signal then is amplified by a low-noise amplifier that has a specific frequency response within a band centred at a radio frequency (RF) which we denote by f_{RF} . The amplified signal then is passed through a bandpass filter so that any harmonics from out-of-band interference signals (e.g. from communication devices, TV stations etc.) are rejected. At this point, the RF signal usually is converted to a lower frequency for two reasons: (a) it is more efficient to transmit a low-frequency signal (i.e. cable losses are lower); (b) much of the data-acquisition hardware which we will discuss in later sections accept signals in a certain frequency range.

Frequency conversion is achieved by a device known as a *mixer* that beats the RF signal with a monochromatic signal of frequency f_{LO} provided by a *local oscillator* (LO). The result is an *intermediate frequency* (IF) signal at the sum and difference of f_{RF} and f_{LO} . Although the sum of the frequencies can be used, most of the time we require the difference frequency for *down conversion*, so that $f_{\text{IF}} = f_{\text{RF}} - f_{\text{LO}}$. Usually, $f_{\text{LO}} < f_{\text{RF}}$, so that the resulting IF (known as the *upper sideband*) has the same frequency sense as the RF, i.e. an increase in IF corresponds to an increase in RF. The *lower sideband* case, where $f_{\text{LO}} > f_{\text{RF}}$, produces a frequency inversion, i.e. an increase in IF corresponds to a decrease in RF) and is used less frequently.

The IF signals either may be sent directly to data acquisition devices such as filterbanks or correlators (see Sections 5.2.1 and 5.2.2) or converted to *baseband*, with a further mixing process as shown before being sent to baseband sampling devices (see Section 5.3). As a real-time signal and interference monitor, the signal is traditionally low-pass-filtered and detected (squared) so that the resulting power is plotted on a pen chart recorder. The pen chart recorder was, inadvertently, the first ‘pulsar backend’ used serendipitously by Jocelyn Bell-Burnell to discover pulsars back in 1967. Sadly, these wonderful devices are becoming less common in observatories nowadays as modern data acquisition systems discussed below provide enhanced functionality.

5.2 Incoherent de-dispersion

The simplest way to compensate for the effects of pulse dispersion is to split the incoming frequency band into a large number of independent *frequency channels* using a spectrometer, and apply appropriate time delays to each channel, so that the received pulses arrive at the output of each channel at the same time. This is carried out using either dedicated hardware, or nowadays more commonly, software. In either case, the appropriate time delays should be calculated by recalling the dispersion relationship (see Equation (4.7)) in which the difference in arrival times Δt between a pulse received in a channel with frequency f_{chan} relative to some reference frequency f_{ref} (often chosen to be the centre frequency of the observed band) can be written as simply

$$\Delta t \simeq 4.15 \times 10^6 \text{ ms} \times (f_{\text{ref}}^{-2} - f_{\text{chan}}^{-2}) \times \text{DM}. \quad (5.1)$$

In this equation, as before, the frequencies are measured in MHz and the dispersion measure DM (cm^{-3} pc) is the integrated column density of free electrons along the line of sight. The exact value of the constant in this expression is given in Chapter 4 (see also Appendix 2). As shown in Figure 5.2, the appropriately delayed frequency channels then can be added together to produce a *de-dispersed time series*.

It is apparent from Figure 5.2 that this *incoherent de-dispersion* process is limited by the width of the individual frequency channels that inherently retain a small dispersion delay. Rearranging Equation (5.1) for a finite bandwidth Δf about some centre frequency f , we find, for the practical case in which $f \gg \Delta f$, that the dispersive delay across a frequency channel of width Δf , for the same units as above, is given by

$$t_{\text{DM}} \simeq 8.3 \times 10^6 \text{ ms} \times \text{DM} \times \Delta f \times f^{-3}. \quad (5.2)$$

Careful choice of the channel bandwidths therefore is required to ensure that t_{DM} does not become a significant fraction of the pulse period. At 430 MHz, most current spectrometers have $\Delta f \sim 0.1$ MHz. This translates to $t_{\text{DM}} \simeq 10 \mu\text{s} \text{ DM}^{-1}$ and, in the absence of additional interstellar scattering, is adequate to detect millisecond pulsars with DMs of up to 100 cm^{-3} pc. The strong dependence on observing frequency means that broader channel bandwidths may be used at higher frequencies. For example, a 512×0.5 MHz channel spectrometer currently in use at Parkes has $t_{\text{DM}} = 1.5 \mu\text{s} \text{ DM}^{-1}$ at 1400 MHz. Although the dispersion limit usually dominates time resolution considerations, we note that the fundamental resolution for a filter channel of width $\Delta\nu$ is $1/\Delta\nu$. For $\Delta\nu = 0.5$ MHz, this corresponds to a resolution of $2\mu\text{s}$.

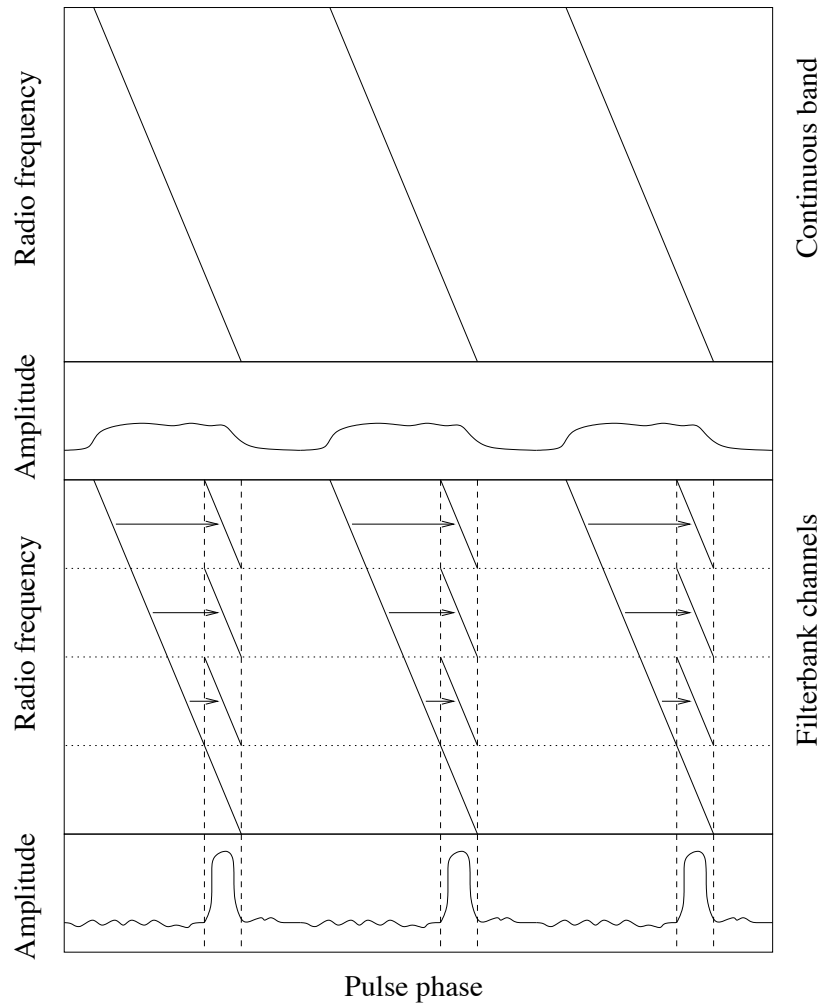


Fig. 5.2. Pulse dispersion and the process of de-dispersion. Simply detecting the pulse over a finite bandwidth results in a significantly broadened profile (top panel). Dividing the passband into smaller bandwidth channels and applying the appropriate delay to each channel considerably reduces the broadening and increases the pulse S/N ratio (lower panel).

5.2.1 Analogue filterbank spectrometers

The simplest and most widely used data acquisition device for incoherent de-dispersion is the analogue filterbank spectrometer. This device per-

forms the task shown in Figure 5.2, in which a broad-band signal is split up into adjacent frequency channels that are passed through narrow-band filters tuned (e.g. using a simple LC circuit) to accept frequencies only within a specific range. Each frequency channel is then digitised separately.

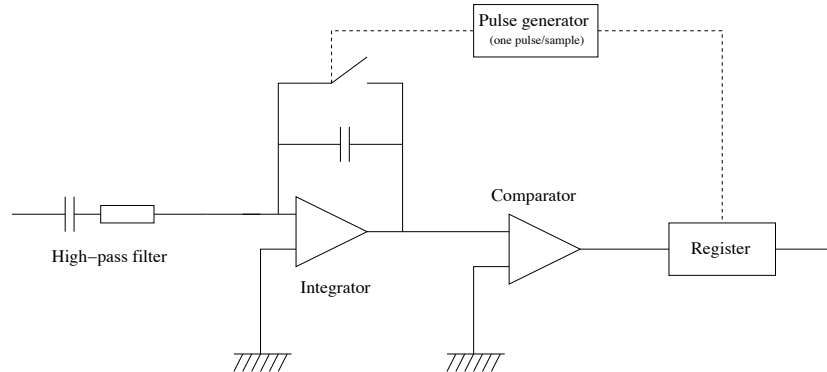


Fig. 5.3. Schematic showing a one-bit digitisation scheme to sample filterbank data. Figure design provided by Andrew Lyne.

The simplest digitisation scheme is one-bit sampling. Shown schematically in Figure 5.3, the incoming narrow-band signal passes through the RC circuit with a time constant of typically ~ 1 s. This effectively filters out low-frequency receiver variations. The integrator outputs the running mean of this signal, which is compared with 0 V by the comparator. Sampling is achieved by clocking the output of the comparator with the register once per sampling interval, t_{samp} , and synchronously closing the switch on the integrator as shown. The resulting output is then either 1 or 0 depending on whether the running mean is positive or negative. It is worth noting that since the integrator effectively convolves the signal with a top-hat function of width t_{samp} , it acts as a low-pass filter rejecting most frequencies greater than $1/t_{\text{samp}}$. This is particularly useful, since it negates the need for specialised anti-aliasing filters developed in earlier implementations of these systems (see, for example, Brinklow (1989)).

At first sight, single-bit digitisation appears to be an overly crude approach to sampling. However, particularly for search projects in which the sampled data from narrow channel bandwidths often are dominated by noise with only a small contribution from the signal, it can be shown

(see, for example, Brinklow (1989)) that the loss of sensitivity relative to perfect sampling is only $(1 - \sqrt{2/\pi}) \simeq 20\%^1$. For large search projects, this relatively minor reduction in sensitivity is often well worth the saving in data storage and reduction. In addition, unlike multi-bit schemes, one-bit digitisation is extremely robust against strong impulsive bursts of interference. Indeed pulsar surveys made using single-bit digitisers sampling the filterbanks at the Parkes and, to a lesser extent, Jodrell Bank radio telescopes have been responsible for the discovery of about two-thirds of all known pulsars (Lyne 2003).

For polarisation studies, the four Stokes parameters from filterbanks can be obtained using an adding polarimeter that we do not discuss here as such systems are generally complicated to calibrate (for details see, for example, von Hoensbroech and Xilouris (1997)).

5.2.2 Autocorrelation spectrometers

An alternative means of obtaining a filterbank-style output is the autocorrelation spectrometer. Shown schematically in Figure 5.4, this device multiplies the signal with a delayed version of itself. The resulting set of *lagged products* in the time domain then can be used to calculate the power in the radio frequency domain. Consider a voltage, $v(t)$, and its complex conjugate, $v^*(t)$, from a radio telescope as a function of time t . The Wiener–Khinchin theorem (see, for example, Rohlfs and Wilson (2000)) states that the autocorrelation function

$$R(\tau) = \lim_{T \rightarrow \infty} \frac{1}{T} \int_0^T v(t)v^*(t + \tau) dt \quad (5.3)$$

and the power spectrum are a Fourier transform pair, i.e.

$$P(f) = \frac{1}{2\pi} \int_{-\infty}^{+\infty} R(\tau) e^{-2\pi if\tau} d\tau. \quad (5.4)$$

Normally, the lagged products are stored on disk for subsequent off-line processing to produce $P(f)$. Note that the number of synthesised frequency channels is equal to the number of lags recorded. Since this number can be varied easily, autocorrelation spectrometry provides variable channel bandwidths and is therefore much more flexible than an analogue filterbank where the width and number of filters are fixed.

¹ Extending Brinklow's (1989) analysis to multi-bit sampling of weak signals, we find that the degradation in S/N to be about 14 and 3 per cent, respectively, for three- and nine-level sampling.

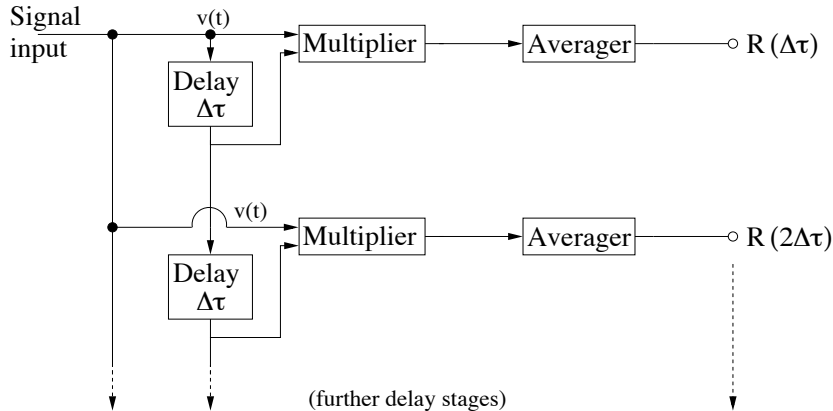


Fig. 5.4. Block diagram of an autocorrelation spectrometer. The input signal here from a single polarisation channel is split and multiplied by delayed versions of itself for a number of different delay times $\Delta\tau$. The resulting signals are passed to an accumulator that outputs the averaged lagged products once per data sampling interval. As mentioned in the text, this approach can be extended easily to form the cross-correlation products for two orthogonal polarisation channels. Figure adapted from an original design by Jon Hagen.

The above discussion assumes autocorrelation of a single polarisation channel. In practice, we sample two orthogonal channels obtaining a spectrum $P(f)$ for each. Denoting these two channels by A and B and the resulting power spectra of the autocorrelation functions by P_{AA} and P_{BB} , the total intensity $I = P_{AA} + P_{BB}$. In addition to autocorrelating each channel, the cross-correlation products also can be formed easily, i.e. P_{AB} and P_{BA} . This provides a very straightforward way to obtain all four Stokes parameters I, Q, U and V (see Appendix 1) for polarimetric observations. For a dual-linear feed:

$$\begin{bmatrix} I \\ Q \\ U \\ V \end{bmatrix} = \begin{bmatrix} P_{AA} + P_{BB} \\ P_{AA} - P_{BB} \\ 2 \operatorname{Re}[P_{AB}] \\ 2 \operatorname{Im}[P_{BA}] \end{bmatrix}, \quad (5.5)$$

while for observations with a dual-circular feed:

$$\begin{bmatrix} I \\ Q \\ U \\ V \end{bmatrix} = \begin{bmatrix} P_{AA} + P_{BB} \\ 2 \operatorname{Im}[P_{BA}] \\ 2 \operatorname{Re}[P_{AB}] \\ P_{BB} - P_{AA} \end{bmatrix}. \quad (5.6)$$

This is far simpler than the corresponding formation of the Stokes parameters from the analogue filterbanks. The Stokes parameters formed from the auto- and cross-correlation products need to be properly calibrated prior to analysis and interpretation. Details of these calibration procedures are discussed in Chapter 7.

As was also necessary for the filterbank data, the auto- and cross-correlation products need to be digitised. Most early correlators used a one-bit (two-level) scheme. Most devices currently in use apply three-level, or, for high dynamic range observations, nine-level sampling. A secondary effect of finite sampling is to bias the measured correlation functions. While S/N losses are unavoidable, the bias can be corrected for. This correction was first developed for one-bit sampling by van Vleck and Middleton (1966) who showed that, for a measured correlation coefficient r , the unbiased correlation coefficient $\hat{r} = \sin(\pi r/2)$. Unfortunately, the generalisation of this so-called *van Vleck correction* to multi-bit sampling becomes rapidly non-trivial. The three-level sampling case (see, for example, Hagen and Farley (1973)) requires a non-analytic solution to the integral

$$r = \frac{1}{\pi} \int_0^{\hat{r}} \left[\exp\left(\frac{-(\varepsilon/\sigma)^2}{1+x}\right) + \exp\left(\frac{-(\varepsilon/\sigma)^2}{1-x}\right) \right] \frac{dx}{\sqrt{(1-x^2)}}, \quad (5.7)$$

where ε is the digitiser threshold and σ is the root mean square voltage. Kulkarni and Heiles (1980) have considered the three-level case in detail and derived a number of useful approximations to the van Vleck formula for the auto- and cross-correlation products.

5.3 Coherent de-dispersion systems

The deleterious effects of interstellar dispersion can be completely removed by making use of the phase of the incoming voltage from the telescope. This technique – known as *coherent de-dispersion* – was pioneered by Hankins and Rickett (1975). After measuring the complex voltage induced in the telescope feed by the incoming electromagnetic radiation, $v(t)$, this method recovers the intrinsic complex voltage as it originated from the pulsar, $v_{\text{int}}(t)$. This then is transformed into a real signal that retains the instrumental (Nyquist) time resolution without being affected by the dispersive effects of the interstellar medium².

² Multi-path scattering, discussed in Chapters 1 and 4, is a different effect that can not be removed in a direct manner. Scattering therefore affects both incoherently and coherently dispersed pulse profiles. Methods to restore the unscattered pulse

The superiority of the coherent de-dispersion scheme versus incoherent de-dispersion is demonstrated clearly for PSR B1937+21 in Figure 1.2.

5.3.1 Principles of coherent de-dispersion

Coherent de-dispersion exploits the fact that the modification of the propagating signal by the interstellar medium can be described as the work of a ‘phase-only’ filter, or *transfer function* H . This relationship becomes particularly simple in the frequency domain. For a signal centred on a frequency f_0 and with a limited bandwidth, Δf , we can write

$$V(f_0 + f) = V_{\text{int}}(f_0 + f)H(f_0 + f), \quad (5.8)$$

where $V(f)$ and $V_{\text{int}}(f)$ are the corresponding Fourier transforms of the raw voltages $v(t)$ and $v_{\text{int}}(t)$. These are non-zero only for $|f| < \Delta f/2$, i.e.

$$v(t) = \int_{f_0 - \Delta f/2}^{f_0 + \Delta f/2} V(f)e^{i2\pi ft} df \quad (5.9)$$

$$v_{\text{int}}(t) = \int_{f_0 - \Delta f/2}^{f_0 + \Delta f/2} V_{\text{int}}(f)e^{i2\pi ft} df. \quad (5.10)$$

From our discussion of the propagation of radio waves in the interstellar medium in Chapter 4, we recall that the delay in the interstellar medium can be represented as phase rotations that depend on frequency and path length travelled, $\Delta\Phi = -k(f_0 + f)d$, where $k(f)$ is the wavenumber and d is the distance to the pulsar (see Chapter 4). Therefore, the transfer function becomes simply

$$H(f_0 + f) = e^{-ik(f_0 + f)d}. \quad (5.11)$$

The idea is now to determine H for a given pulsar and to apply its inverse to the measured, Fourier-transformed voltage. Once this is done, the result is transformed back into the time domain to obtain the desired de-dispersed signal.

In order to obtain a practical expression for the transfer function, we recall the relationship from Chapter 4 between the wavenumber and

shape by deconvolution are discussed by Kuzmin and Izvekova (1993), Löhmer *et al.* (2001) and Bhat, Cordes and Chatterjee (2003).

frequency (see Equation (4.8)). This becomes

$$k(f_0 + f) = \frac{2\pi}{c}(f_0 + f)\sqrt{1 - \frac{f_p^2}{(f_0 + f)^2} \mp \frac{f_p^2 f_B}{(f_0 + f)^3}}, \quad (5.12)$$

where, as before, f_p and f_B are respectively the plasma and cyclotron frequencies. In Chapter 4, we saw that for the interstellar medium $f_p \sim 2$ kHz and $f_B \sim 3$ Hz. Therefore, when the observing frequency f is above a few hundred MHz, we find the sizes of the last two terms in the above expression to be of the order of 10^{-10} and 10^{-18} , respectively. We can approximate, therefore, the above expression by keeping only the first terms in a Taylor expansion, resulting in

$$k(f_0 + f) \approx \frac{2\pi}{c}(f_0 + f) \left[1 - \frac{f_p^2}{2(f_0 + f)^2} \right]. \quad (5.13)$$

While we ignored here the usually minute difference in propagation speed for left- and right-hand circularly polarised signals, it may be necessary in special cases to use different transfer functions for different polarisation channels, which may also mean that we should keep higher-order terms of the Taylor expansion.

Inserting the above expression for the wavenumber into the transfer function, we find

$$H(f_0 + f) = e^{-i\left\{\frac{2\pi}{c}(f_0 + f)\left[1 - \frac{f_p^2}{2(f_0 + f)^2}\right] \times d\right\}} \quad (5.14)$$

$$= e^{i\frac{2\pi}{c}d\left(f_0 + f - \frac{f_p^2}{2(f_0 + f)}\right)}. \quad (5.15)$$

Finally, using the identity

$$\frac{1}{f_0 + f} = \frac{1}{f_0} - \frac{f}{f_0^2} + \frac{f^2}{(f_0 + f)f_0^2}, \quad (5.16)$$

we arrive at the desired result:

$$H(f_0 + f) = e^{-i\frac{2\pi}{c}d\left\{\left(f_0 - \frac{f_p^2}{2f_0}\right) + \left(1 + \frac{f_p^2}{f_0^2}\right)f - \frac{f_p^2}{2(f_0 + f)f_0^2}f^2\right\}}. \quad (5.17)$$

Here, we have sorted the terms that are independent of, linear and quadratic in f , respectively. The first term represents an arbitrary, constant phase offset that cannot be determined as it is lost during the later (square-law) signal detection. The second term depends on f and, according to the shift-theorem (Bracewell 1998), corresponds to a delay in the time domain. We can ignore this term simply by shifting the

arrival time by the appropriate amount. The last term causes phase rotations within the band that are quadratic in f . These need to be unwound in order recover the original pulsar signal. Taking only this term into account, we obtain the transfer function relevant for coherent de-dispersion

$$H(f_0 + f) = e^{+i\frac{2\pi}{c}d\frac{f_p^2}{2(f+f_0)f_0^2}f^2}. \quad (5.18)$$

This expression still includes the distance, d , and the (average) plasma frequency, f_p . We can replace these quantities by the directly observable dispersion measure, DM. Since the dispersion constant, \mathcal{D} , defined in Equation (4.6) is related to the plasma frequency by

$$\mathcal{D} = \frac{f_p^2}{2cn_e}, \quad (5.19)$$

where n_e is the average electron density along the line of sight, we can identify the expression

$$\frac{f_p^2 d}{2c} = \text{DM} \times \mathcal{D} \quad (5.20)$$

which we use to write the transfer function as

$$H(f_0 + f) = e^{+i\frac{2\pi\mathcal{D}}{(f+f_0)f_0^2}\text{DM}f^2}. \quad (5.21)$$

5.3.2 Baseband sampling

By applying to the inverse of the transfer function, H^{-1} , to the sampled voltage data, the originally emitted voltage is recovered. In order to do this, we have to modify the phases of the complex Fourier components of $V(f_0 + f)$ in the way described by H^{-1} . This requires sampling and digitisation of $v(t)$, such that both amplitude and phases are measured using a method called *baseband sampling*.

The bandwidth-limited complex voltage, $v(t)$, can be written as a combination of its (real) amplitude, $a(t)$, a time-varying phase term, $\phi(t)$, and the carrier wave centred at f_0 ,

$$v(t) = a(t)e^{i\phi(t)}e^{i2\pi f_0 t}. \quad (5.22)$$

Now we mix the signal with that of a local oscillator (LO) of frequency f_{LO} , to produce a signal \mathcal{I} . A second signal \mathcal{Q} is produced that uses the same LO but with a phase shift of 90° (or $\pi/2$). We can represent

the derived two signals as being the result of the multiplication with the cosine and sine branch of the mixing carrier wave,

$$\mathcal{I}(t) = a(t)e^{i\phi(t)}e^{i2\pi f_0 t} \cos(2\pi f_{\text{LO}} t) \quad (5.23)$$

$$\mathcal{Q}(t) = a(t)e^{i\phi(t)}e^{i2\pi f_0 t} \sin(2\pi f_{\text{LO}} t). \quad (5.24)$$

Using the Euler identities, we obtain

$$\mathcal{I}(t) = \frac{1}{2}a(t)e^{i\phi(t)} \left\{ e^{i2\pi(f_0+f_{\text{LO}})t} + e^{i2\pi(f_0-f_{\text{LO}})t} \right\} \quad (5.25)$$

$$\mathcal{Q}(t) = \frac{1}{2i}a(t)e^{i\phi(t)} \left\{ e^{i2\pi(f_0+f_{\text{LO}})t} - e^{i2\pi(f_0-f_{\text{LO}})t} \right\}. \quad (5.26)$$

The next step is to low-pass-filter the signal, i.e. to allow only frequencies with $f \leq \Delta f/2$ to propagate further. This removes the frequency parts corresponding to $f_0 + f_{\text{LO}}$, hence,

$$\mathcal{I}(t) = \frac{1}{2}a(t)e^{i\phi(t)}e^{i2\pi(f_0-f_{\text{LO}})t} = \frac{1}{2}a(t)e^{i(2\pi(f_0-f_{\text{LO}})t+\phi(t))} \quad (5.27)$$

$$\mathcal{Q}(t) = \frac{i}{2}a(t)e^{i\phi(t)}e^{i2\pi(f_0-f_{\text{LO}})t} = \frac{i}{2}a(t)e^{i(2\pi(f_0-f_{\text{LO}})t+\phi(t))} \quad (5.28)$$

If we choose the LO frequency such that it is in the centre of our band (i.e. $f_{\text{LO}} = f_0$), the bandpass $[f_0 - \Delta f/2; f_0 + \Delta f/2]$ is shifted to $[-\Delta f/2; +\Delta f/2]$, which is called *baseband*. For the digitised real parts of the signals, we obtain

$$I(t) \equiv \text{Re}(\mathcal{I}(t)) = \frac{1}{2}a(t) \cos(\phi(t)) \quad (5.29)$$

$$Q(t) \equiv \text{Re}(\mathcal{Q}(t)) = -\frac{1}{2}a(t) \sin(\phi(t)), \quad (5.30)$$

giving us access to both the amplitude and phase of the complex voltage $v(t)$. The signals $I(t)$ and $Q(t)$ can be viewed as the real and imaginary part of $v(t)$. This form of baseband mixing with $f_{\text{LO}} = f_0$ is shown in Figure 5.5 and provides *complex sampled* data. Another way of viewing it is to consider $I(f)$ and $Q(f)$ as providing both positive and negative frequencies of the bandpass relative to f_0 in the Fourier domain, $[-\Delta f/2; +\Delta f/2]$.

The data rate required for Nyquist sampling I or Q is $2 \times \Delta f/2 = \Delta f$. As we have to sample both signals I and Q , the total data rate is $2\Delta f$. Choosing f_{LO} to coincide with the upper or lower edge of our observing frequency range, as shown in Figure 5.5, produces a passband at $[-\Delta f, 0]$ when $f_{\text{LO}} = f_0 + \Delta f/2$ (lower-sideband down conversion) or one at $[0, \Delta f]$ when $f_{\text{LO}} = f_0 - \Delta f/2$ (upper-sideband down conversion). For these cases, we have to sample only one signal, but the data rate must

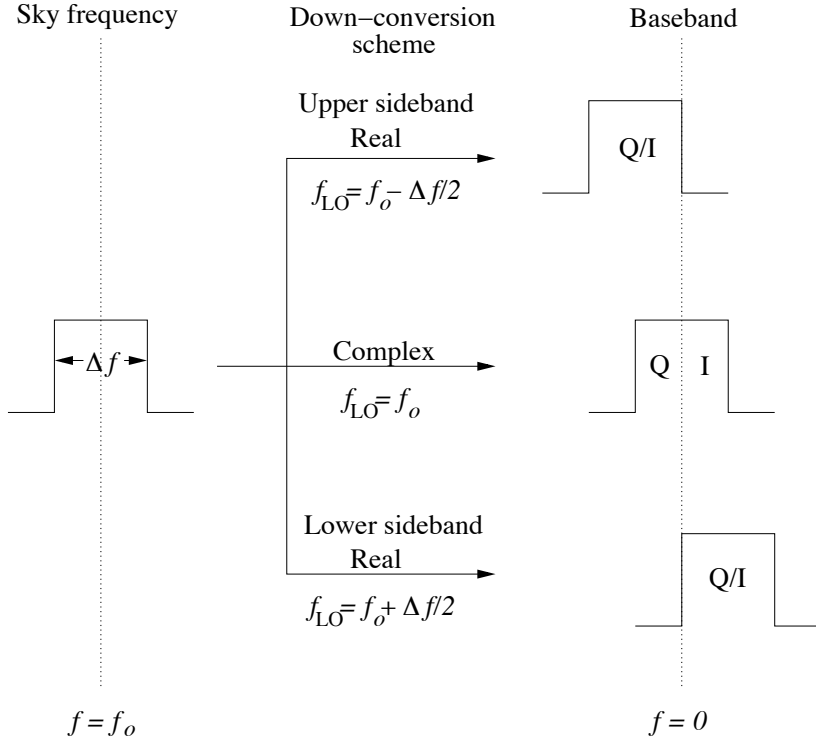


Fig. 5.5. Schematic showing various possible baseband mixing schemes depending on the placement of the local oscillator (see text).

be higher, $2\Delta f$. While this is the same as the total rate as for complex sampled data, the demand on the data-acquisition hardware in terms of speed is higher. Moreover, since we do not sample orthogonal signals, an additional Fourier transform is needed to recover the relative phase information that is needed for polarimetry (Shrauner 1997). Both factors usually lead to the implementation of complex sampling rather than real sampling.

This shift of our passband to baseband does not affect the Fourier transforms of our voltages, so that we can finally apply

$$V_{\text{int}}(f) = V(f)H^{-1}(f_0 + f). \quad (5.31)$$

In practical implementations, the inverse transfer function is combined with a taper, T , that is chosen such that it emphasises anti-aliasing in

the low-pass filtering. The combination of both:

$$C(f_0, f) \equiv T(f)H^{-1}(f_0 + f) \quad (5.32)$$

is known as the *chirp function*.

5.3.3 Implementation

The multiplication of the chirp function with the measured voltage in the Fourier domain corresponds to a convolution in the time domain (see, for example, Bracewell (1998)). This is important for considering the length of the voltage data required for de-dispersion. We certainly need a length of at least the dispersion delay between the upper and lower edge of our bandpass, t_{DM} (see Equation (5.2)). For a bandwidth Δf that is complex sampled at the Nyquist rate, the number of samples needed is $n_{\text{DM}} = t_{\text{DM}}\Delta f$ for each of I and Q . However, since a discrete convolution of each point of a time series of length n depends on $n/2$ points both before and after it, we need to pad our voltage series with another $n_{\text{DM}}/2$ samples at the beginning and at the end. Therefore, the shortest data set we can coherently de-disperse must be at least $2n_{\text{DM}}$ samples long. For efficiency, longer data sets are usually chosen, in particular since past constraints such as memory size become increasingly less important today. In any case, the ‘wings’ of length $n_{\text{DM}}/2$ at the beginning and end of each data set need to be ignored after the convolution.

A typical implementation of coherent de-dispersion is given by the following recipe:

- (i) Mix signals of the observing frequency to baseband, digitise both I and Q by sampling each at a rate Δf .
- (ii) Take a set of data of length n samples.
- (iii) Compute a discretely sampled chirp function for n samples.
- (iv) Fourier transform the data set of n points and multiply the resulting Fourier components with the elements of the chirp function.
- (v) Inverse Fourier transform the result back into the time domain.
- (vi) Ignore the wings of $n_{\text{DM}}/2$ samples at the beginning and end of the time series and save the remaining $n - n_{\text{DM}}$ points as output.
- (vii) Take the next $n - n_{\text{DM}}$ points from the input data and add them to last n_{DM} points of the current set. Proceed with step (iii) on the new set of n samples.

By this cyclic procedure shown also in Figure 5.6, a continuous coherently de-dispersed time-series is formed.

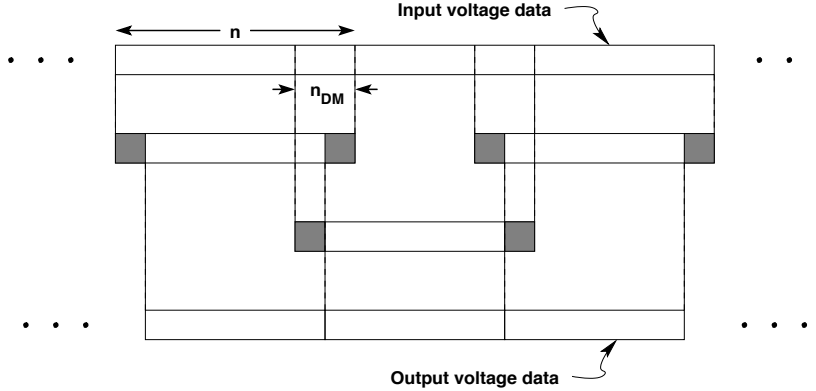


Fig. 5.6. Schematic showing the overlap-save procedure in coherent de-dispersion. The input data are split into overlapping sections of n points. Each section is Fourier-transformed separately and the chirp function is applied before Fourier transforming each segment back into the time domain. Points from the overlapping regions shown in grey are discarded before re-combining the resulting independent segments into a single time series. Figure adapted from an original version (van Straten 2003) provided by Willem van Straten.

Two practicalities to this general scheme are worth noting for completeness: (a) in order to avoid discarding the first $n_{\text{DM}}/2$ samples in the output data, the initial data block is zero-padded with a dummy wing of $n_{\text{DM}}/2$ samples; (b) additional steps to mitigate radio-frequency interference in both the frequency and time domains (see Section 7.5 for details) can be implemented before and after steps (iv) and (v).

5.3.4 Polarimetry

The application of coherent de-dispersion based on complex-sampled data has the additional important benefit that all four Stokes parameters are readily accessible if two orthogonal polarisation channels are sampled by the feed. In a similar way to the correlators described earlier, we can obtain the four Stokes parameters I , Q , U and V from the signals from two orthogonal linear polarisation channels X and Y as follows:

$$\begin{bmatrix} I \\ Q \\ U \\ V \end{bmatrix} = \begin{bmatrix} |X|^2 + |Y|^2 \\ |X|^2 - |Y|^2 \\ 2 \operatorname{Re}(X^* Y) \\ 2 \operatorname{Im}(X^* Y) \end{bmatrix}, \quad (5.33)$$

where $*$ indicates a complex conjugate. All signals can be easily formed by simple computations in memory during step (vi) of the recipe above. For the case of left and right-handed signals from circular feeds L and R , we have:

$$\begin{bmatrix} I \\ Q \\ U \\ V \end{bmatrix} = \begin{bmatrix} |L|^2 + |R|^2 \\ 2 \operatorname{Re}(L^* R) \\ 2 \operatorname{Im}(L^* R) \\ |R|^2 - |L|^2 \end{bmatrix}. \quad (5.34)$$

Calibration of the Stokes parameters will be discussed in Chapter 7.

5.3.5 Baseband recorders

It was not possible, until recently, to perform the required number of floating-point operations necessary for coherent de-dispersion on-line in software. Unless dedicated hardware were built to perform the calculations (see below), a common solution has been to write the sampled data to a fast-recording tape medium. The data then can be ‘played back’ subsequently and analysed by a computer off-line. The advantage of this technique is that the software can be improved constantly and data re-analysed. A disadvantage, however, is that one is observing ‘blindly’ as no immediate feed-back about the quality of the observations is available. Moreover, very often the observing bandwidth had been limited by speed (or price!) of the available tape media. For this reason, some systems are now equipped with a large number of hard disks in which the data are saved for subsequent processing.

5.3.6 On-line coherent de-dispersers

On-line systems provide immediate access to the data and therefore are the most flexible and efficient in terms of observing flexibility. Three main types have been developed over the past years.

In a hardware solution, dedicated processor chips perform the computations in real time. This can be achieved by employing a digital filterbank, so that only small pieces of baseband need to be processed by each chip. In some implementations, the de-dispersion is not achieved by applying the chirp in the frequency domain, but by performing a convolution in the time domain. A disadvantage of some of these systems has been that the de-dispersed data cannot be dumped fast enough, so that a number of pulses have to be integrated to keep the data rate

low. Single-pulse observations therefore are not possible. As for all on-line systems, the baseband data cannot be played back for a second re-processing.

The recent advance in processor speed and the development of easy-to-build *Beowulf clusters* has triggered the birth of a new branch of on-line de-disperser. In one implementation, the data are stored on disks before they are picked up and analysed by a large number of PC processors. For small dispersion measures and bandwidths, this process is sustained in quasi real time. If even further processing power is available, the data can be sent directly to processors without being written to disk in an immediate stage. This can be facilitated by splitting the band into smaller chunks that are easier to process.

In order to get an idea of how the computational requirements scale, consider processing a segment of data of length comparable to the dispersion delay across an observing band Δf . From the dispersion relation, the observation time for this segment $t_{\text{obs}} \propto \text{DM} \times \Delta f$. Complex sampling of the data requires a sampling interval $t_{\text{samp}} = 1/\Delta f$. The resulting number of samples per fast Fourier transform (FFT) $n_{\text{FFT}} = t_{\text{obs}}/t_{\text{samp}} \propto \text{DM} \times \Delta f^2$. Since the time to compute each FFT $t_{\text{FFT}} \propto n_{\text{FFT}} \log_2(n_{\text{FFT}})$, (see, for example, Press *et al.* (1992)) then the ratio of computational time to observing time $t_{\text{FFT}}/t_{\text{obs}} \propto \Delta f \log_2(\text{DM} \Delta f^2)$.

5.3.7 Software filterbanks

The flexibility of modern coherent de-dispersion machines becomes apparent for observing modes other than coherent de-dispersion. For example, by taking short Fourier transforms of the complex-sampled data followed by the computation of the power spectrum, it is relatively straightforward to modify the software in order to simulate an incoherent filterbank. Sorting the samples accordingly, a simple filterbank output is achieved. Performing all the operations in software gives complete flexibility of the channelisation of the data, unlike the simple analogue filterbanks discussed in Section 5.2.1.

In a variation of this approach, one takes the Fourier components of the coarse filterbank channels and performs coherent de-dispersion on them rather than computing simply the power spectrum.

In both cases, care should be taken to avoid contamination of the data of one coarse frequency channel by signals from the others; this is known as *spectral leakage* and occurs because a short Fourier transform is not

very efficient in separating the frequency components. Further details on software filterbanks can be found in Jenet *et al.* (1997).

5.4 Further reading

Most of the techniques to sample and process the pulsar signal presented in this chapter were originally described in the landmark paper by Hankins and Rickett (1975). Many of these ideas are covered in a slightly different style in the very useful review by Bhattacharya (1998).

Further discussion of filterbanks can be found in Jacoby and Anderson (2001) and Lyne (2003). Although remarkably successful over the years, and still in use at many observatories, analogue filterbanks are becoming somewhat dated. One aspect of the rapid development of digital signal processing technology that is starting to be applied to pulsar research is the so-called *digital filterbank* (Foster *et al.* 1996; Backer *et al.* 1997). Based on finite impulse response filters and high-speed Fourier transform chips, much like the correlators, digital filterbanks offer a much more flexible output than their analogue counterparts.

Although often hardware-specific, a number of useful references describing pulsar data acquisition systems often provide a good background in some of the techniques and technology implemented. The Princeton University pulsar group has been active in this area for many years with a number of generations of incoherent devices (see, for example, the filterbank-based ‘Mk III’ system described by Stinebring *et al.* (1992)), or more recently the ‘Mk IV’ baseband recording system (Shrauner 1997; Stairs *et al.* 2000a; Ord 2002). Other recent developments include the Caltech Baseband Recorder at Arecibo (Jenet *et al.* 1997), PuMa, a baseband sampler in use at the Westerbork telescope (Voûte *et al.* 2002) and the CPSR/CPSR2 recording systems at Parkes (van Straten 2003). Beowulf cluster approaches to data reduction either at or close to real-time observing are now becoming more common. At the time of writing (February 2004), a number of systems are in development at Arecibo (ASP; Arecibo Signal Processor), Green Bank (GASP; Green Bank Astronomical Signal Processor) and Jodrell Bank (COBRA; Coherent Online Baseband Receiver for Astronomy), (Joshi *et al.* 2003).

5.5 Available resources

On the book web site (Appendix 3), we maintain an up-to-date table of existing pulsar data acquisition systems that are available for use (ei-

ther freely or by arrangement with the owners) for pulsar observations at most of the large radio telescopes around the world. Where available, links to contact people, relevant documentation, data formats and software are provided. For various reasons, each data acquisition system writes data in its own local format. While attempts to standardise the format of the processed data from these machines are being made, e.g. the EPN format (Lorimer *et al.* 1998) and PSRFITS (Hotan *et al.* 2004), raw data are invariably written in non-standard formats that are unique to each system. Some attempts at generic data recognition are being made: the SIGPROC, PRESTO and PSRCHIVE packages (Lorimer (2001), Ransom (2001) and Hotan *et al.* (2004), respectively) are capable of reading raw data in a variety of formats. These packages are now freely available and can be obtained via the links on the web site.

6

Finding new pulsars

Pulsar searching is conceptually a simple process – the detection of dispersed pulses in noisy data. The first pulsars were discovered serendipitously by visual inspection of the total power output from a radio telescope (Hewish *et al.* 1968). However, only a small fraction of the 1700 pulsars currently known are strong enough to be discovered via their individual pulses. The vast majority of known pulsars, and most that still await discovery, are faint objects which require sensitive telescopes and innovative techniques to reveal their periodic nature. From the discussion in Chapters 1 and 2, the motivation for probing deeper into this population is to discover exotic pulsars (e.g. those in binary systems) and to better characterise the Galactic distribution and evolution of neutron stars.

Since the early days of pulsar astronomy, a lot of effort has gone into developing sophisticated algorithms to maximise the sensitivity and efficiency of the pulsar search process. A summary of most of the resulting techniques we explore in this Chapter is presented in Figure 6.1. We begin by describing the main components of the ‘standard’ frequency domain radio pulsar search procedure which involves de-dispersion, Fourier transformation and candidate selection. We then move on to extensions of this approach to searches for short-period binary pulsars. Searches in the time domain are becoming increasingly popular; we discuss the fast-folding algorithm and single-pulse searches in this context. Virtually all searches of radio data now need to combat the ever-increasing levels of interference present; we discuss briefly time- and frequency-domain mitigation techniques. We conclude with an overview of tried and tested strategies required to optimise a search for the various types of pulsars.

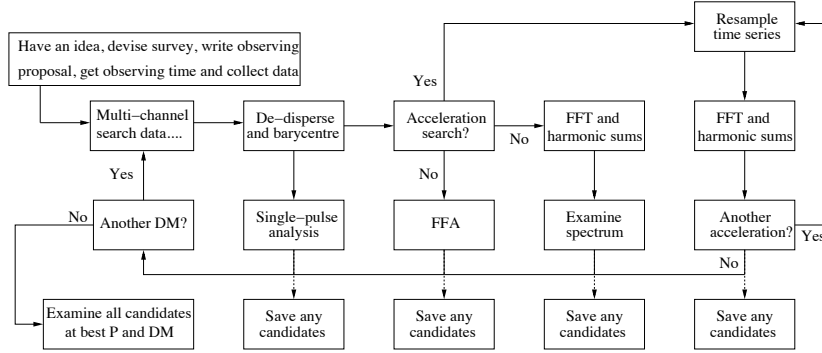


Fig. 6.1. Flow diagram summarising the main steps in a pulsar search and the most commonly used algorithms. Frequency domain acceleration searches and radio frequency excision techniques are not shown here (for clarity) but are described in detail in Sections 6.2.2 and 6.4, respectively.

6.1 Standard search procedure

We begin by describing the most commonly used procedure to find a periodic signal of unknown pulse period and dispersion measure (DM). The data are first de-dispersed to form a number of time series spanning a wide range of trial DM values. Each time series then can be independently searched for the presence of periodic signals. The standard procedure is to Fourier transform the time series and search the resulting amplitude or power spectra for significant features. The best candidates from the analysis are saved and the whole process is repeated for another trial DM. After processing all of the time series in this way, a list of pulsar candidates is compiled and the de-dispersed data are folded modulo each candidate period for further inspection.

6.1.1 The de-dispersion stage

Now we expand on these steps in detail, beginning with a description of the basic algorithms for dispersion removal, optimal choice of trial DM step and an efficient de-dispersion scheme.

6.1.1.1 Simple de-dispersion

Considering the raw data as a two-dimensional array of time samples and frequency channels, we write the j^{th} time sample of the l^{th} frequency channel as \mathcal{R}_{jl} . For n_{chans} frequency channels, the j^{th} sample of the

de-dispersed time series, \mathcal{T}_j , is then

$$\mathcal{T}_j = \sum_{l=1}^{n_{\text{chans}}} \mathcal{R}_{j+k(l),l}, \quad (6.1)$$

where $k(l)$ is the nearest integer number of time samples corresponding to the dispersion delay of the l^{th} frequency channel relative to some reference frequency. Labelling the l^{th} frequency channel of the data by f_l , and recalling the dispersion relation (see Equation (4.7)), we can write $k(l)$ in terms of the trial DM, the data sampling interval t_{samp} and the channel frequencies as follows:

$$k(l) = \left(\frac{t_{\text{samp}}}{4.15 \times 10^6 \text{ ms}} \right)^{-1} \left(\frac{\text{DM}}{\text{cm}^{-3} \text{ pc}} \right) \left[\left(\frac{f_l}{\text{MHz}} \right)^{-2} - \left(\frac{f_1}{\text{MHz}} \right)^{-2} \right]. \quad (6.2)$$

Here we have assumed that the channel ordering in \mathcal{R} starts at the highest frequency ($l = 1$) and proceeds in descending frequency order. The channel frequencies are therefore given by

$$f_l = f_1 - (l - 1)\Delta f_{\text{chans}}, \quad (6.3)$$

where Δf_{chans} is the channel bandwidth.

6.1.1.2 Choice of dispersion step size

Some consideration needs to be made in order to choose the most appropriate interval between trial DM values. This should not be so large that a real pulsar with a true DM lying between two trial values is significantly broadened and sensitivity is lost. Conversely, the interval should not be too small that computing power is wasted on producing and searching de-dispersed time series that are virtually identical for neighbouring trial DMs. In order to quantify this, consider a simple top-hat pulse of intrinsic width W_{int} . De-dispersion at an incorrect trial DM value that differs by ΔDM from the true value broadens the pulse across the entire bandwidth. When $\Delta f \ll f$, the resulting effective pulse width

$$W_{\text{eff}} = \sqrt{W_{\text{int}}^2 + (k_{\text{DM}} \times |\Delta\text{DM}| \times \Delta f/f^3)^2}, \quad (6.4)$$

where $k_{\text{DM}} = 8.3 \times 10^6 \text{ ms}$ if pulse widths are measured in ms and, as usual, DM is in units of $\text{cm}^{-3} \text{ pc}$ and the bandwidth Δf and centre frequency f are in MHz. In Appendix 1, we derive the observing sensitivity to pulse signals. Ignoring constant system-dependent factors in

Equation (A1.22) of Appendix 1, we find a simple relationship between signal to noise (S/N) ratio, effective pulse width W_{eff} and period P :

$$\text{S/N} \propto \sqrt{\frac{P - W_{\text{eff}}}{W_{\text{eff}}}}. \quad (6.5)$$

Combining the above two equations, we can calculate the response of a data acquisition system to incorrect de-dispersion. This is shown in Figure 6.2, in which we plot S/N versus trial DM for a variety of different pulse periods relative to the S/N value for a true DM of $50 \text{ cm}^{-3} \text{ pc}$. As expected, the choice of DM step becomes critical when attempting to detect dispersed pulsars with periods below a few hundred ms.

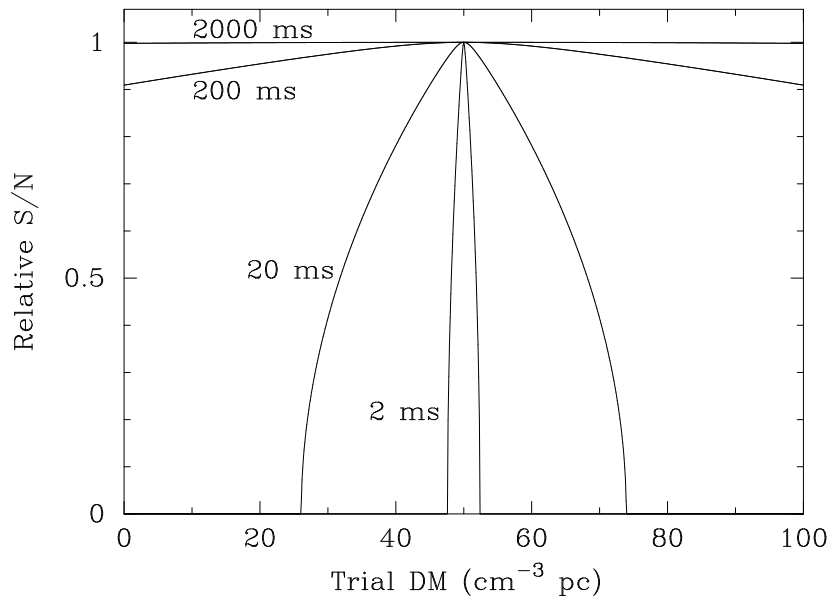


Fig. 6.2. Relative S/N as a function of trial DM for a hypothetical data acquisition system spanning an 8 MHz band centred at 430 MHz. Each curve corresponds to a different pulse period as indicated. In each case the true DM value is assumed to be $50 \text{ cm}^{-3} \text{ pc}$ and the intrinsic pulse duty cycle (W_{int}/P) is assumed to be 5 per cent. Effects of scattering and dispersion across filterbank channels are assumed to be negligible.

A sensible choice of DM step is to set the delay between the highest and lowest frequency channels equal to the data sampling interval. Again, starting with the dispersion relation, the i^{th} DM value can be written in terms of the total bandwidth Δf (MHz), centre frequency f

(MHz) and sampling time t_{samp} (ms) as

$$\text{DM}_i = 1.205 \times 10^{-7} \text{ cm}^{-3} \text{ pc } (i - 1)t_{\text{samp}}(f^3/\Delta f). \quad (6.6)$$

The case $i = 1$ corresponds to the ‘zero DM’ time series – simply combining all the frequency channels without any time delays. This time series is used primarily to identify sources of interference (see Section 6.4). When $i = n_{\text{chans}} + 1$, the so-called ‘diagonal DM’ value is reached. At this DM, the total delay across the band is equal to $n_{\text{chans}} \times t_{\text{samp}}$ and the broadening across an *individual frequency channel* is equal to t_{samp} .

Above the diagonal DM the effective time resolution starts to become dominated by the broadening in the individual channels. Usually when $i = 2n_{\text{chans}}$ or $i = 3n_{\text{chans}}$, adjacent time samples are added together so that the rest of the processing requires fewer computations. Since dispersion broadening is now the dominant effect, halving the effective time resolution does not impact on the sensitivity to short-period pulsars. The entire process now can be repeated on the new coarser data to produce time series with higher dispersion measures out beyond the now higher value of the diagonal DM until the desired DM limit is reached. Typically, we expect DMs in excess of 1000 cm^{-3} pc for surveys along the Galactic plane and $\lesssim 50 \text{ cm}^{-3}$ pc for high Galactic latitudes. As a general rule, we recommend using a reasonable model of the electron density distribution (see, for example, Section 4.4) to estimate the maximum DM for the lines of sight sampled by the survey and multiply this by a factor of two to account for uncertainties in the electron density model.

6.1.1.3 Tree de-dispersion

The simple de-dispersion process described above is rather computationally expensive, since it requires n_{chans}^2 floating-point operations to de-disperse every n_{chans} time samples. Inspired by the fast-folding algorithm developed by Staelin (1969); (see Section 6.3.1), Taylor (1974) proposed a more efficient de-dispersion scheme known as the ‘tree algorithm’. As shown in Figure 6.3, the tree algorithm derives its name from the fact that it can be built from successively smaller components which all start from simple two-channel ‘branches’. For example, a four-channel tree can be built from a pair of two-channel branches; an eight-channel tree derives from two four-channel branches etc. As a result, the tree algorithm requires a base-two number of frequency channels.

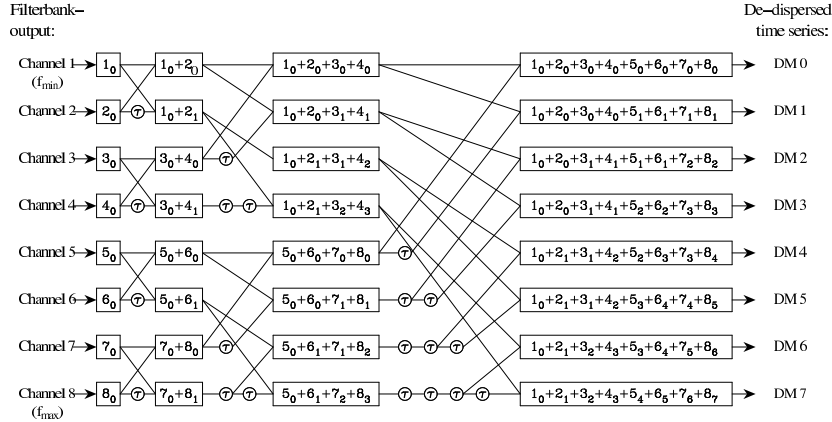


Fig. 6.3. Taylor's tree algorithm for de-dispersion showing the eight-channel case. Figure provided by Bernd Klein.

Rather than requiring n_{chans}^2 operations, the identification of redundant and repeated operations reduces the overall computational requirement to $n_{\text{chans}} \log_2 n_{\text{chans}}$ operations. In general, the resulting number of time series produced by the tree algorithm is equal to the input number of frequency channels. When the time delay is set to be equal to t_{samp} , the DM steps are the same as in Equation (6.6).

An implicit assumption in the tree de-dispersion process is that the dispersion delay across the frequency band is linear. While the exact form of the dispersion law (see Equation (4.7)) is a quadratic function of frequency, the relatively narrow bandwidths employed mean that this assumption is often adequate. For some searches, however, the data need to be corrected before the tree algorithm can be used. For example, in the Parkes multibeam survey (Manchester *et al.* 2001) where $f = 1374$ MHz and $\Delta f = 288$ MHz, the ninety-six channel filterbank data were padded by an additional thirty-two channels across the band. This ‘linearisation’ process changes the effective channel frequency slightly so that the dispersion delay more closely approximates a straight line. In this case, the total number of channels becomes a base-two number as required.

In practice, the additional computations required to linearise the data before the tree stage, as well as the computational input/output requirements demanded by the tree algorithm in producing multiple de-dispersed time series, mean that it may not always be optimal to imple-

ment a tree algorithm. Benchmarking brute-force de-dispersion schemes against tree de-dispersion is often advisable during the planning phases of a pulsar survey.

6.1.2 Barycentric correction for long time series

Most radio pulsar search data are of relatively short (< 30 min) duration. Over this time, the effects of the rotation of the Earth and its motion around the Sun can be safely ignored. For deep radio searches (see Sections 6.5.4 and 6.5.5), and searches at X-ray and γ -ray wavelengths carried out with orbiting satellites, the relative motion between the observatory and the target becomes important and should be corrected prior to attempting a periodicity search. As for pulsar timing applications (see Chapter 8) the standard approach is to refer the observed (topocentric) data collected at the telescope to the solar system barycentre (SSB) which, to a very good approximation, is an inertial reference frame.

To transform a topocentric time series to the SSB, first we must delay or advance the start time of the observation, t_{start} , appropriately to match the arrival time of the first sample at the SSB, $t_{\text{start,SSB}}$. This is identical to the correction applied to pulse arrival times described in detail in Chapter 8. The arrival time of subsequent samples then needs to be monitored so that it does not differ significantly from the expected arrival time at the SSB. Specifically, we compare the arrival time of the i^{th} sample $t_i = t_{\text{start,SSB}} + (i - 1)t_{\text{samp}}$ with the arrival time corrected for the relative motion between the observatory and the SSB: $\tau_i = t_{\text{start,SSB}} + (i - 1)t_{\text{samp,SSB}}$. The corrected sampling time $t_{\text{samp,SSB}}$ is a variable quantity due to the continually changing relative motion and can be calculated using a pulsar timing program such as TEMPO (see Chapter 8). The correction then proceeds by adding or subtracting whole samples from the time series so that $|\tau_i - t_i| < t_{\text{samp}}$. Added samples are usually chosen to be the mean value of the time series.

6.1.3 Periodicity searches using the Fourier transform

Given a de-dispersed time series T_j that, if necessary, has been appropriately barycentred, we need an algorithm to search it for the presence of periodic signals. One of the most efficient and widely used techniques is to take the Fourier transform of the time series and examine the Fourier

(frequency) domain. In the following subsections, we review the salient properties of Fourier transform for pulsar searching.

6.1.3.1 The discrete Fourier transform

Since the de-dispersed time series \mathcal{T}_j is a set of N independently sampled data points, rather than the continuous form of the Fourier transform, we compute the discrete Fourier transform (DFT). By definition, the k^{th} Fourier component of the DFT

$$\mathcal{F}_k = \sum_{j=0}^{N-1} \mathcal{T}_j \exp(-2\pi i j k / N), \quad (6.7)$$

where $i = \sqrt{-1}$ and N is the number of elements in the time series. Throughout this chapter, we will assume that all Fourier components \mathcal{F}_k have been normalised by the factor $(N\overline{\mathcal{T}_j^2})^{1/2}$ (see, for example, Ransom *et al.* (2002)). As we shall see later, this turns out to be convenient when estimating significance levels of pulsar candidates. For equally-spaced data in the time domain with a sampling interval t_{samp} , the frequency of the k^{th} Fourier component $\nu_k = k/(Nt_{\text{samp}}) = k/T$, where T is the length of the observation and $1 < k < N/2$. The width of each frequency ‘bin’ therefore is simply $1/T$ and the highest frequency component is the Nyquist frequency $\nu_{\text{Nyq}} = 1/(2t_{\text{samp}})$.

It is apparent, from Equation (6.7), that the computation of an N -point DFT requires N^2 floating-point operations. For modern applications, in which we deal often with time series for which $N \geq 2^{25}$, this can become very time consuming, even for current-day computers. Fortunately, there are two ways to reduce the computation time. The first of these is the fast Fourier transform (FFT), which requires only $N \log_2 N$ operations to transform an N -sample time series. A further improvement comes from the fact that the time series is a set of purely real numbers. As a result, while the highest frequency in the Fourier domain is nominally $1/t_{\text{samp}}$, the DFT is symmetric about the Nyquist frequency, ν_{Nyq} . Fourier components above ν_{Nyq} are just the complex conjugates of their low-frequency counterparts:

$$\mathcal{F}_{N-k} = (\mathcal{F}_k)^*, \quad (6.8)$$

where the asterisk denotes the complex conjugate. This redundancy can be exploited (see, for example, Press *et al.* (1992)) to calculate the DFT of two N -point real data sets simultaneously, or a single data set of length $N/2$.

6.1.3.2 Searching for periodic signals in the Fourier domain

Displaying either the amplitudes ($\mathcal{A}_k = |\mathcal{F}_k|$) or powers ($\mathcal{P}_k = |\mathcal{F}_k|^2$) of the Fourier components as a function of frequency is an extremely sensitive means of revealing a periodic signal. This is illustrated in Figure 6.4, in which we have sampled a 25 Hz sine wave in the presence of purely Gaussian noise with a standard deviation that is 3 times the amplitude of the signal. As a result, the sinusoidal signal is essentially undetectable by examining the time domain. The ‘power spectrum’ in the Fourier domain, however, shows a clearly visible line at 25 Hz.

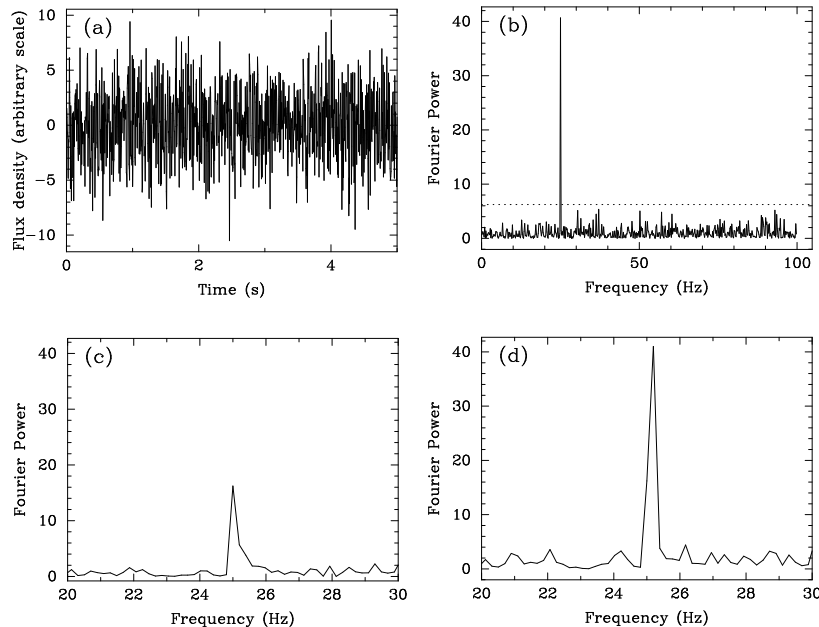


Fig. 6.4. (a) A noisy time series containing a 25 Hz signal; (b) the power spectrum of the DFT of this time series (i.e. $|\mathcal{F}_k|^2$ as a function of k). The dashed line shows the detection threshold based on the number of independent estimates of spectral power; (c) an expanded view of the spectrum showing the DFT response to a 25.125 Hz signal in which the effects of scalloping reduce the power by about 60 per cent; (d) recovery of the power by Fourier interpolation (see text).

One limitation of the DFT is that its frequency response is not uniform and is in fact only ideal for signals that match exactly the centre frequencies of the Fourier bins. As mentioned above, each bin in the frequency domain is characterised by its central frequency $\nu_k = k/T$

and width $\Delta\nu = 1/T$. The result of this ‘scalloping’ effect is a reduction in sensitivity to signals away from ν_k . Consider a signal of frequency $\nu_r = r/T$, where r is now a real number such that ν_r lies within the frequency range of bin k , i.e. $|\nu_k - \nu_r| < \Delta\nu/2$. Starting from the definition of the DFT, it can be shown (see, for example, Ransom *et al.* (2002)) that

$$\mathcal{F}_r = \mathcal{F}_k \operatorname{sinc}[\pi(k - r)]. \quad (6.9)$$

In the extreme case, when the signal frequency falls midway between two bins ($|k - r| = 0.5$), the Fourier amplitude is reduced by 36 per cent and the corresponding power by 60 per cent. This reduction can be seen in Figure 6.4(d) where the frequency of the original 25 Hz sinusoid has been changed to 25.125 Hz.

The main methods to recover this loss in sensitivity are zero padding, Fourier domain interpolation and interbinning. Zero padding – simply the addition of zero-valued elements to the time series – is the most straightforward procedure. Since this process adds no noise or signal into the time domain data (i.e. Parseval’s theorem); (see Bracewell (1998)) the Fourier components are unaffected by this operation. This increases N and reduces $\Delta\nu$ accordingly. While this reduces the effects of scalloping somewhat, it does, of course, mean that the required FFTs are larger. For long time series, this can become computationally too costly.

When the expected frequency of the signal is known, or has been found from a preliminary search, the signal can essentially be recovered completely by correlating the nearest integer bin to r , which we denote by $[r]$, with the inverse of the sinc response, i.e.

$$\mathcal{F}_r \simeq \sum_{k=[r]-m/2}^{[r]+m/2} \mathcal{F}_k \exp(-i\pi(r - k)) \operatorname{sinc}[\pi(r - k)]. \quad (6.10)$$

Typical values for the range of bins around r might be $m = 32$ (see Ransom *et al.* (2002) for further details).

A less computationally expensive version of *Fourier interpolation* is known as ‘interbinning’, in which the power at half-integer frequencies can be estimated from just the two neighbouring bins (i.e. $m = 2$ in the above expression). In this case, the half-integer power $\mathcal{P}_{k+\frac{1}{2}} = |\mathcal{F}_{k+\frac{1}{2}}|^2$, where

$$\mathcal{F}_{k+\frac{1}{2}} \simeq \frac{\pi}{4} (\mathcal{F}_k - \mathcal{F}_{k+1}). \quad (6.11)$$

Using this simple technique, the Fourier amplitude of a signal lying midway between two independent bins is reduced by only 7 per cent.

A related approach also in use is to compare the power in each Fourier bin with those of its two nearest neighbours and replace it according to

$$\mathcal{P}_k = \max \left\{ \frac{|\mathcal{F}_{k-1} + \mathcal{F}_k|^2}{2}, |\mathcal{F}_k|^2, \frac{|\mathcal{F}_k + \mathcal{F}_{k+1}|^2}{2} \right\}. \quad (6.12)$$

As a result, a signal split between two bins is combined into a single bin. This method is used to great effect in Figure 6.4(d). One result of all these schemes is that the resultant Fourier components are not independent quantities. This turns out to have a relatively small effect on the noise statistics discussed later.

6.1.3.3 Removing low-frequency noise

Our example time series and its Fourier transform in Figure 6.4 assumed purely Gaussian noise. The Fourier spectrum of Gaussian noise is ‘white’, i.e. the Fourier power is distributed uniformly over the entire frequency range. Well-behaved white noise is ideal, because the estimation of the significance level of any signal is relatively simple (see below). Although time series obtained from real pulsar search data closely resemble Gaussian noise, fluctuations in the receiver and/or data acquisition systems often manifest themselves via a significant low-frequency or ‘red noise’ component when viewed in the Fourier domain. An example of this is shown in Figure 6.5.

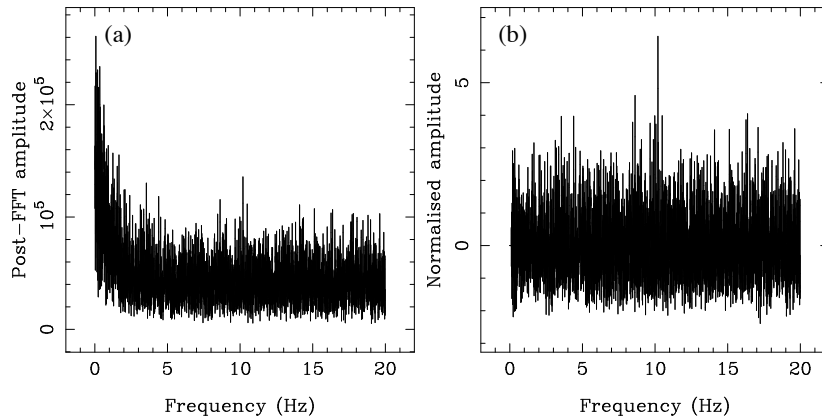


Fig. 6.5. (a) Amplitude spectrum from data collected using the Parkes telescope. (b) Spectrum after a whitening procedure has been applied to remove the red noise component. The whitened spectrum then has been normalised so that it has a zero mean and unit root mean square (see text).

Before attempting to estimate significance levels of any signal present in these data, it is standard practice to whiten the spectrum so that the response to noise is as uniform as possible. The most common technique in use is to break the spectrum up into a number of contiguous pieces, calculating the mean and root mean square value for each one. Care must be taken at this stage to avoid biasing the mean and root mean square values from outlying points, and often the median is used rather than the mean. Subtracting a running median and normalising the local root mean square will result in the whitened spectrum having a zero mean and unit root mean square. With this normalisation scheme, the S/N ratio of any spectral feature is simply its amplitude.

6.1.3.4 Increasing sensitivity to narrow pulses

Our discussion so far has considered purely sinusoidal signals that appear in the Fourier domain as a single line at the fundamental frequency of the sinusoid. In reality, however, the pulsed signals we are trying to detect have a duty cycle (i.e. the pulse width divided by the period) that is typically only a few per cent. In the Fourier domain, the power from such a narrow pulse is distributed between the fundamental frequency and a significant number of harmonics.

In order to estimate the number of harmonics present, consider the time series as a train of top hat pulses of width W spaced by the pulse period P . In the time domain, this can be viewed as a single top hat function convolved with a train of delta functions separated by P (i.e. the Shah or comb function). In the Fourier domain (see, for example, Bracewell (1998)) this convolution is just the product of the Fourier transforms of the two functions. The Fourier transform of the top hat is proportional to $\text{sinc}(\pi f W)$, that has a first null when the Fourier frequency $f = 1/W$. The Shah function Fourier transforms to another Shah function with spacing of $1/P$. The resulting Fourier transform of our pulse train is simply a series of delta functions harmonically spaced by $1/P$ with amplitudes that are bounded by the envelope of the sinc function. Taking the extent of the harmonics as being roughly the width of the sinc envelope to its first null, the number of harmonics is roughly P/W , i.e. the reciprocal of the pulse duty cycle.

For typical pulse duty cycles of order 5 per cent, the expected number of harmonics is of order 20, as shown in the example spectrum for PSR B2303+30 (Figure 6.6(a)). In order to take full advantage of the power contained in these harmonics, a technique known as ‘incoherent harmonic summing’, first devised by Taylor and Huguenin (1969), is

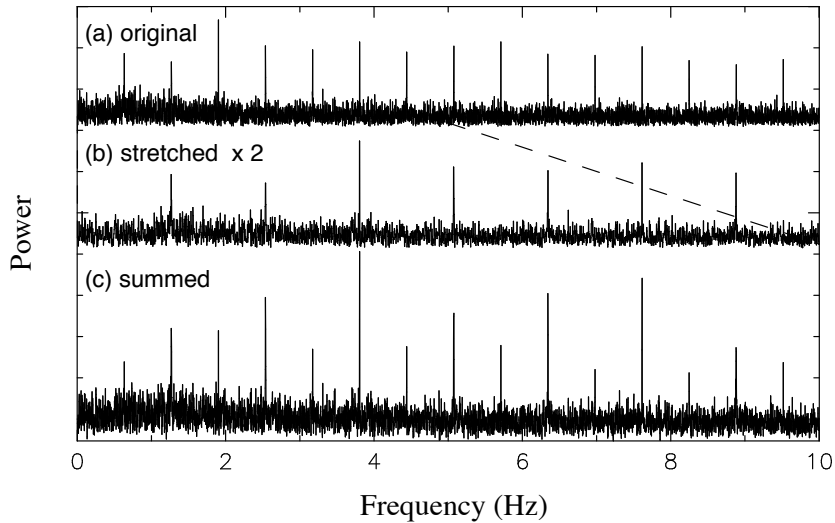


Fig. 6.6. The process of harmonic summing illustrated in the power spectrum of an observation of PSR B2303+30 collected with the Ooty radio telescope at 327 MHz (see text for further details). Figure provided by Dipankar Bhattacharya.

used. In the example shown in Figure 6.6, the lower half of the original spectrum is stretched by a factor of 2 (Figure 6.6(b)) and then added to the original unstretched spectrum. As a result, all second harmonics are added to their corresponding fundamentals. Although this summation process increases the noise in the folded spectrum by a factor of $\sqrt{2}$, the amplitudes of two harmonics add directly. For two harmonics of roughly equal power, the net gain in S/N is of order $\sqrt{2}$. By repeating this process several times, and taking care to add in odd-numbered harmonics, the S/N to a narrow duty cycle pulse increases significantly.

A good illustration of the improvement gained by harmonic summing is shown in Figure 6.7 which is the result of an analysis assuming idealised pulses described by Ransom *et al.* (2002). This shows the various duty cycle regimes in which harmonic summing is effective. While the single harmonic sensitivity is adequate for duty cycles wider than 30 per cent, it is clear for narrower pulses that the harmonic summing schemes are essential in order to retain full sensitivity. Most pulsar search codes produce a total of five spectra that are searched independently: the spectrum of the DFT itself, and four subsequent harmonically folded versions which contain the sum of the first two, four, eight, and sixteen

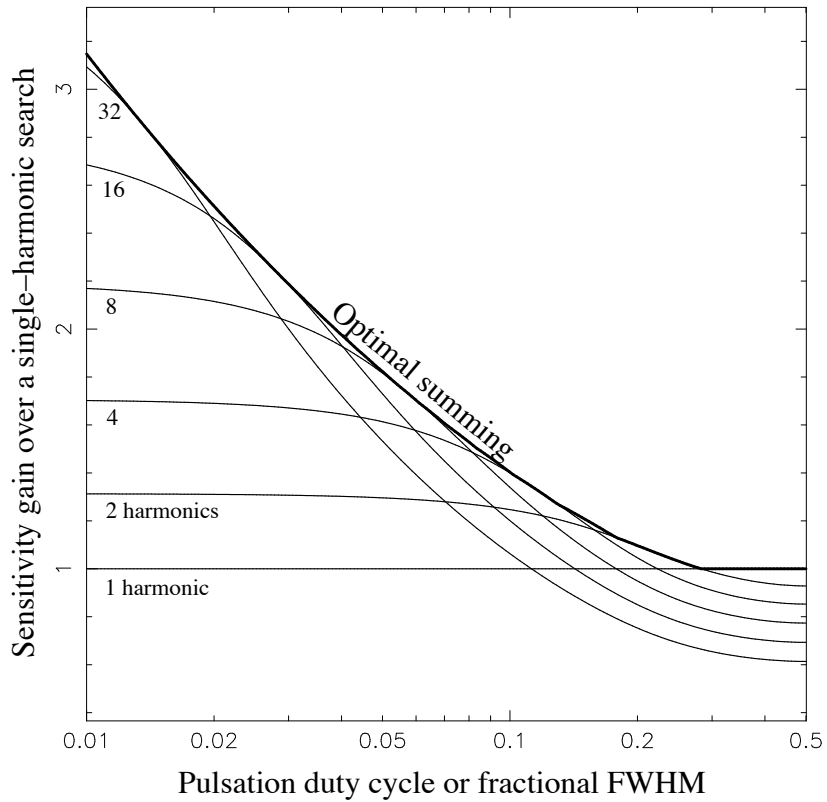


Fig. 6.7. An illustration of the gain in sensitivity due to harmonic summing (thin curves) over a single-harmonic DFT analysis (horizontal line) as a function of pulse duty cycle. The thick solid line shows the optimal harmonic sum. Figure and analysis provided by Scott Ransom.

harmonics, respectively. As Figure 6.7 shows, this choice guarantees that most of the range of pulse duty cycles are searched with optimal sensitivity. However, for duty cycles less than 2 per cent, some improvement in sensitivity can be made by summing up to thirty-two harmonics.

6.1.3.5 False-alarm probabilities and S/N ratios

In order to calculate the significance of signals in the Fourier domain, we need to know the response of the DFT to random noise. In the ideal case¹ for a time series containing pure Gaussian noise, the probability

¹ As discussed earlier, in reality the noise does not follow strictly a Gaussian distribution. Also, the Fourier interpolation discussed above means that the amplitude

density function (PDF) of the real and imaginary parts of the Fourier components also follow a Gaussian PDF. In the spectral analysis, we deal either with Fourier power (the sum of the squares of the real and imaginary components) or the amplitude (square root of the power). In general, the sum of the squares of n independent variables with Gaussian PDFs is the χ^2 distribution with n degrees of freedom. In our case, where $n = 2$, the powers follow an exponential PDF that can be integrated easily to show that the probability that the power in an individual bin \mathcal{P}_k exceeds some threshold \mathcal{P}_{\min} is simply proportional to $\exp(-\mathcal{P}_{\min})$. This is sometimes called the *false-alarm probability*, i.e. the chance of a candidate being the result of noise fluctuations rather than a real event. For the single harmonic shown in Figure 6.4(b), the normalised power level is ~ 40 . The corresponding false-alarm probability $p_{\text{false}} = \exp(-40) \simeq 4 \times 10^{-18}!$

For the more general case, in which harmonic folding has been performed m times, the PDF follows a χ^2 distribution with $2m$ degrees of freedom. The corresponding false-alarm probability can be written as

$$p_{\text{false}}(\mathcal{P} > \mathcal{P}_{\min}) = \sum_{j=0}^{m-1} \frac{(\mathcal{P})^j}{j!} \exp(-\mathcal{P}_{\min}). \quad (6.13)$$

Here, it is assumed that the powers have been normalised by the factor $N\bar{\mathcal{T}}_j^2$ where, as before, N is the number of samples in the time series \mathcal{T}_j (see, for example, Ransom *et al.* (2002)).

We can estimate a reasonable detection threshold for any given search based on the false-alarm probability of a single event and the number of trials. For the sinusoidal signal in Figure 6.4, the number of points in the time series is 1024, resulting in 512 separate samples of power in the Fourier domain. The expected number of false alarms above a given power threshold \mathcal{P}_{\min} is simply $512 \exp(-\mathcal{P}_{\min})$. Setting this number to be less than one event, it follows that $\mathcal{P}_{\min} = -\ln(1/512) \simeq 6.2$. This threshold power level is shown by the dashed line in Figure 6.4(b).

For analyses that work with Fourier amplitudes (\mathcal{A}) rather than powers, it is more common to quote S/N thresholds. Since S/N values are calculated from the Fourier amplitudes by subtracting a mean value ($\bar{\mathcal{A}}$) and dividing by the local root mean square ($\sigma_{\mathcal{A}}$) the false-alarm proba-

and power values are not strictly independent quantities. Fortunately, the departure from a χ^2 distribution due to these effects is small and can be ignored safely.

bility that the S/N will exceed a threshold S/N_{\min} is given by

$$p_{\text{false}}(S/N > S/N_{\min}) = \exp(-[\sigma_{\mathcal{A}} S/N_{\min} + \bar{\mathcal{A}}]^2). \quad (6.14)$$

Integrating the exponential PDF in terms of amplitude rather than power, we find $\bar{\mathcal{A}} = \sqrt{\pi/4}$ and $\sigma_{\mathcal{A}} = 1 - \pi/4$. Using these values, we can repeat the above threshold calculation in terms of S/N. In general, for a search with n_{trials} independent S/N estimates, a suitable threshold is:

$$S/N_{\min} = \frac{\sqrt{\ln[n_{\text{trials}}]} - \sqrt{\pi/4}}{1 - \pi/4} \simeq \frac{\sqrt{\ln[n_{\text{trials}}]} - 0.88}{0.47}. \quad (6.15)$$

For the 512-sample DFT in Figure 6.4, the corresponding threshold S/N would be 3.4. In a real pulsar search, the number of trials is much greater than 512, and S/N_{\min} is appropriately larger. For example, in a recent Arecibo drift-scan survey (Lorimer *et al.* 2004a) an analysis used 492 trial DM values, each of which produces 2^{18} Fourier components which, for the harmonic summing analysis, were analysed independently five times. As a result, $n_{\text{trials}} \sim 6.4 \times 10^8$ and $S/N_{\min} \simeq 7.7$. In practice, because of radio-frequency interference (see Section 6.4), a slightly higher threshold is required (for example, in their search, Lorimer *et al.* (2004a) set $S/N_{\min} = 8$).

6.1.3.6 Reconstructed profiles

No use of the phase information in the Fourier components is made when forming amplitude or power spectra. This information can be used to eliminate ‘signals’ from the harmonic summing analysis that result from random superposition of noise features. Unlike the harmonics produced by a train of pulses, random superposition will result in a random phase relationship between the ‘harmonics’. This can be tested by taking the inverse DFT of the harmonics to form a pulse profile. To ensure that this ‘reconstructed profile’ is entirely real, the DFT is doubled in size to include the complex conjugates of each harmonic used. If the Fourier components are truly phase related, this ‘reconstructed’ profile should have a S/N in the time domain that is comparable to the spectral S/N. A spurious candidate often will show up at this stage with a profile that has a much reduced S/N.

6.1.3.7 Two-dimensional Fourier analysis

The procedure discussed so far is essentially a one-dimensional Fourier analysis that repeats on different de-dispersed time series. An alterna-

tive approach is to consider the raw data as a two-dimensional array of time samples and frequency channels. The two-dimensional Fourier transform of such an array is the space of fluctuation frequency and dispersion delay. A dispersed periodic signal plotted in this phase space appears as a set of harmonically spaced dots in a graph of delay versus frequency. The slope of the dots is proportional to the dispersion measure. Interpolating along lines of constant dispersion measure then would produce amplitude or power spectra that can be analysed with the harmonic summing techniques described above. Although this method has been implemented (see, for example, Camilo *et al.* (1996)), and is in principle more computationally efficient than the one-dimensional approach, the simplicity of brute-force one-dimensional de-dispersion and Fourier transforms usually is preferred.

6.1.3.8 Discontinuities in the time series

The techniques outlined so far assume the time series to be continuous. Unforeseen interruptions in the observation (e.g. due to parking of the telescope in high winds or power outages) can result in a number of discontinuous time series. While these data can be analysed separately, the ideal solution is to perform a coherent Fourier transform over the entire observation. This is achieved by appropriately zero padding the missing time samples.

6.1.4 Candidate selection

The result of all the de-dispersion and Fourier transform stages described above is a list of candidate periods and S/N ratios for all harmonic folds and DMs. A real pulsar usually will appear many times in this list at a variety of S/N values, with the maximum ideally being at the DM that is closest to the true DM value. At this stage, the standard practice is to de-disperse and fold the raw data at the candidate period and DM, and produce diagnostic plots for visual inspection. The details of the folding process are discussed in Chapter 7.

A typical pulsar candidate is shown in Figure 6.8. This example is the original discovery observation of PSR J1842–0415, one of four pulsars discovered in a search using the 100 m Effelsberg radio telescope (Lorimer *et al.* 2000). The integrated profile (top left) has a well defined narrow pulse that appears consistently throughout the integration (bottom left) and in all frequency channels (bottom right). The S/N of the integrated profile should compare well with the S/N in the amplitude or

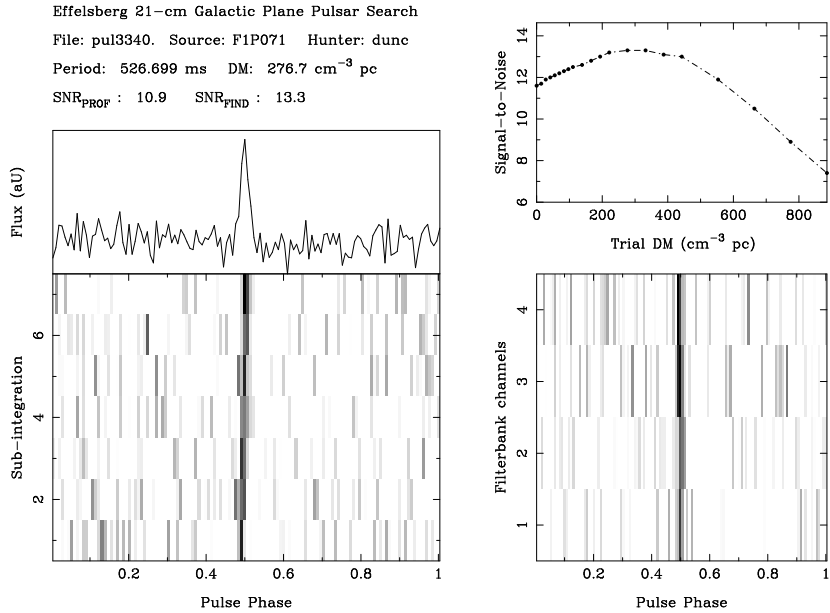


Fig. 6.8. Sample search code output for PSR J1842–0415, the first pulsar discovered using the Effelsberg telescope. See text for further details.

power spectrum and (if calculated) the reconstructed S/N. In addition to the folded profiles, perhaps the most useful diagnostic is S/N versus trial DM shown on the top right as a clear peak at a non-zero DM. As we showed in Section 6.1.1 and Figure 6.2, every pulsar produces a characteristic shape in the S/N–DM plane that depends primarily on the pulse width, period, observing frequency and bandwidth. Good agreement between the observed and theoretical S/N–DM responses is an essential test that any viable pulsar candidate should pass.

6.2 Searches for pulsars in binary systems

Although the Fourier transform is extremely good at finding periodic signals, as noted by a number of authors (see, for example, Middleditch and Priedhorsky (1986) and Johnston and Kulkarni (1991)), the frequency domain analyses discussed above have reduced sensitivity to pulsars in short-period binary systems. The effect of binary motion is to cause a change in the apparent pulse frequency during the integration, spreading the emitted signal power over a number of neighbouring Fourier

bins. As a result, the sharpness of the spectral features and, hence, the S/N ratio and sensitivity of the search are reduced significantly. All is not lost, however, since there are now a number of techniques in use to compensate for, and in some cases fully recover, the loss of sensitivity due to binary motion. These techniques described below generally work optimally under certain conditions and often demand significant computational resources.

6.2.1 Time domain resampling

One approach to signal recovery is to resample the time series to the rest frame of an inertial observer with respect to the pulsar. A straightforward periodicity search of the corrected time series then would detect the pulsar as if it were a solitary object without loss of sensitivity. The correction to the time series is a simple application of the Doppler formula to relate a time interval in the pulsar frame, τ , to the corresponding interval in the observed frame, t :

$$\tau(t) = \tau_0(1 + V_l(t)/c), \quad (6.16)$$

where $V_l(t)$ is the radial velocity of the pulsar along the line of sight, c is the speed of light and we have neglected terms in (v/c) higher than first order. The constant τ_0 is used for normalisation purposes (see, for example, Camilo *et al.* (2000b)). Given a functional form for $V_l(t)$, the re-sampling process proceeds by calculating the time intervals in the new frame from Equation (6.16). New sample values then are created based on a linear interpolation running over the original time series (see also Middleditch and Kristian 1984). Alternatively, the correction can be carried out by adding or removing samples to compensate for the relative phase drift between τ and t as described in Section 6.1.2 for the barycentre correction.

If the orbital parameters of the binary system are known (e.g. if a search is being made for a pulsar in a known binary system) $V_l(t)$ can be calculated from Kepler's laws (see Section 8.3.1.2) and the effects of orbital motion can be removed entirely from the time series. Following unsuccessful attempts on other systems (see, for example, Prince *et al.* (1991)), this technique may well prove fruitful following the discovery of the 2.7 s pulsar companion in the J0737–3039 system (Lyne *et al.* 2004). While this pulsar did not require an exhaustive search, given the stunning applications of J0737–3039 (see Chapter 2), deeper searches for companions in other systems should be carried out.

For the purposes of a blind search, in which the orbital parameters are a priori unknown, assuming a Keplerian model for $V_l(t)$ would require a five-dimensional search of all the parameter space. In practice, computing requirements demand a simpler solution. Although dropping orbital eccentricity and longitude of periastron would allow a three-dimensional search for circular orbit binaries, the simplest model is to assume a constant orbital acceleration a_l during the integration, i.e. $V_l(t) = a_l t$. The so-called ‘acceleration search’ then can be carried out on time series corrected assuming different trial values of a_l in order to cover a region of acceleration space.

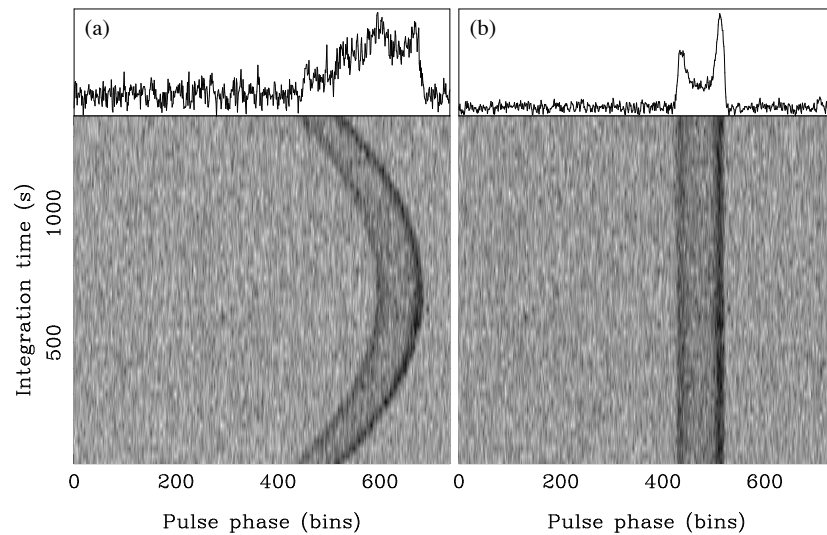


Fig. 6.9. (a) Folded pulse profiles as a function of time for a 22 min Arecibo observation of PSR B1913+16 showing the effects of a changing apparent pulse period. (b) The same time series now folded assuming $a_l = -16 \text{ m s}^{-2}$.

An example of the improvement from the use of an acceleration search is shown in Figure 6.9 for a 22 min observation of the original binary pulsar B1913+16. Although the pulsar is strong enough to be detectable in the observation without any acceleration searching, folding the data at the nominal period from the search results in the heavily smeared profile shown on the left. A search in acceleration space shows a much stronger detection at $a_l \sim -16 \text{ ms}^{-2}$. Folding the acceleration-corrected time series as shown on the right effectively has removed the deleterious

effects of Doppler smearing and the true pulse shape is seen with greater significance.

Some care is required in choosing an appropriate acceleration step size in these searches to compromise between unnecessary processing incurred by over-sampling the parameter space and the loss of sensitivity caused by under-sampling. To quantify this, we need to calculate the number of Fourier bins an accelerated signal will occupy if no correction is applied. Applying the Doppler equation again, the observed pulse frequency $\nu(t) = \nu_0(1 - V_l(t)/c)$, where ν_0 is the true spin frequency of the pulsar in its rest frame and $V_l(t)$ is the line of sight velocity as before. Under the simple assumption that the acceleration approximation is valid (i.e. $V_l(t) = a_l t$), we find that the corresponding frequency drift $|\dot{\nu}| = a_l \nu_0 / c$. For an observation of length T where the width of a Fourier bin $\Delta\nu = 1/T$, the number of frequency bins drifted by the signal

$$N_{\text{drift}} = \dot{\nu}T/\Delta\nu = a_l \nu_0 T^2/c. \quad (6.17)$$

For an acceleration search, the step size Δa_l should be such that the corresponding number of frequency bins drifted $\Delta N_{\text{drift}} < 1$, i.e. $\Delta a_l < cP/T^2$, where P is the spin period. As an example, in 17.5 min analyses of data from the globular cluster 47 Tucanae, Camilo *et al.* (2000b) chose $\Delta a_l = 0.3 \text{ m s}^{-2}$ which guarantees that any pulsars with $P > 2 \text{ ms}$ do not drift by more than one spectral bin.

6.2.2 Frequency-domain techniques

For relatively small numbers of samples ($< 2^{23}$), time domain acceleration searches have been used to good effect to search for pulsars in globular clusters (see, for example, Anderson (1992) and Camilo *et al.* (2000b)). For longer data sets, however, the need to FFT repeatedly after each correction to the time series means that the computational time becomes dominated by FFTs that are very similar to one another. A more efficient approach developed by Ransom *et al.* (2002) is to work entirely in the frequency domain so that only one FFT need be carried out per DM trial.

6.2.2.1 Correlation method

The response of the DFT to a signal of varying frequency can be thought of as the idealised response to a stationary signal convolved with a finite impulse response (FIR) filter which spreads the power over a number of spectral bins. In a similar manner to coherent de-dispersion (Chapter 5)

where an inverse chirp function is applied to the Fourier coefficients, the correlation technique applies an inverse FIR filter (the complex conjugate of the Fourier response) which effectively ‘sweeps up’ the power into a single Fourier bin. If the Fourier response can be written as \mathcal{F}_{k-r_0} , where $|k - r_0|$ is the frequency offset of the k^{th} bin with respect to a reference frequency bin r_0 , the corrected Fourier component

$$\mathcal{F}_{r_0} = \sum_{k=r_0-m/2}^{k=r_0+m/2} \mathcal{F}_k \mathcal{F}_{r_0-k}^*. \quad (6.18)$$

The exact form of the template $\mathcal{F}_{r_0-k}^*$ is a phase rotation term and a set of Fresnel integrals which are functions of the centre frequency bin r_0 and its derivative \dot{r} . Calculating this template for a range of \dot{r} values is equivalent to the time domain acceleration correction, but is computationally much cheaper. This technique was first used to discover PSR J1807–2459, a 1.7 h binary in NGC 6544 (Ransom *et al.* 2001).

6.2.2.2 Stack/slide searches

Both the time-domain resampling and correlation techniques allow a fully coherent search in acceleration space. For large-scale searches (e.g. the Parkes multibeam survey (Manchester *et al.* 2001)), even the correlation approach becomes computationally expensive. A faster acceleration search used for this purpose that works in the frequency domain is the ‘stack/slide’ technique, which follows the orbital motion of a binary pulsar by breaking the integration up into a number of contiguous subsets, each of which is Fourier-transformed separately. This approach has two benefits: (a) the width of a Fourier bin in each segment is larger than for the entire observation; (b) an accelerated signal has less time to drift in frequency during each segment. As a result, the number of Fourier bins through which an accelerated signal will drift is reduced by the square of the number of segments used (see also Equation (6.17)).

Analogous to the time delays applied to compensate for dispersion (see Chapter 5), the effects of a changing frequency can be compensated for by applying frequency shifts (slides) to each spectra before adding (stacking) them together. The resulting stacked spectrum then can be searched for periodicities in the usual way. For an observation of length T split into n_{seg} segments, the change in frequency between two segments due a constant acceleration is simply $\nu_0 a_l T / (n_{\text{seg}} c)$ Hz. While this simple incoherent stacking is less sensitive than a fully coherent acceleration search (typically 20 per cent according to Faulkner

(2004)) it offers a considerable improvement over the standard search. An excellent example is the recent discovery of the 7.7 hr binary pulsar J1756–2251 (Faulkner *et al.* 2004). This highly relativistic system was completely missed in the standard search analyses and only detectable as a result of the stack/slide technique.

6.2.2.3 Phase-modulation searches

For orbital periods comparable to, or much less than, the integration time, the use of one-dimensional acceleration searches is clearly far from optimal, since the orbital motion can no longer be approximated as $V_1(t) = a_{1t}$. Although acceleration derivatives can be added to the search, this soon becomes computationally prohibitive. As an alternative approach, Jouteux *et al.* (2002) and Ransom *et al.* (2003a) developed a ‘phase-modulation search’ which becomes optimal when the observation encompasses several complete orbits. This is often the case for globular cluster searches with typical integration times of 2–10 h.

The phase-modulation search utilises the fact that the amplitude or power spectrum of an observation covering several orbits of a binary system has a characteristic shape imprinted by the constantly changing signal frequency. A high S/N example of this is shown in Figure 6.10(a). Ransom *et al.* (2003a) demonstrated that the imprint can be described by a family of regularly spaced Bessel functions forming a set of sidebands about the spin frequency of the pulsar. The beauty of this result is that the spacing of the sidebands is simply the orbital period. A straightforward DFT of the region of interest will detect the orbital period (Figure 6.10(c)). Just like the search for signals in the time domain, the DFT is an extremely sensitive means of detecting the periodicity in the sidebands, even when they are not readily apparent (as shown in Figure 6.10(b) and (d)).

Once the orbital period is known, the orbital semi-major axis and epoch of ascending node can be determined from the width and phases of the sidebands. For weak pulsars, this often requires specialised techniques to make full use of the phase information of the Fourier components. If the orbit is circular, these three parameters can be used by the correlation technique to determine the appropriate template to recover the power as before. Full details of this procedure can be found in Ransom *et al.* (2003a). A number of current searches of globular clusters are now routinely utilising the phase-modulation technique and may perhaps soon break the 96-min record held for the shortest radio pulsar binary (Camilo *et al.* 2000b).

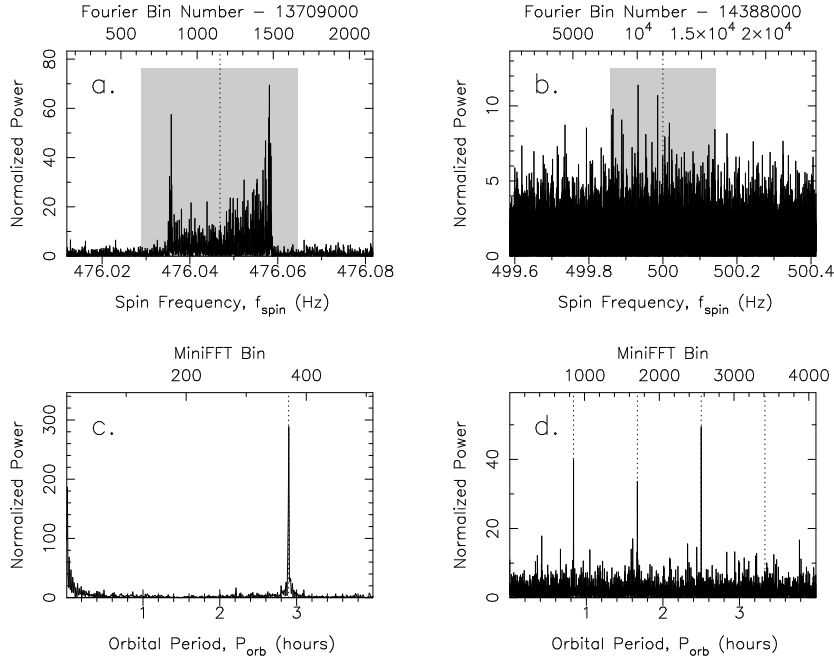


Fig. 6.10. (a) Power spectrum of an 8 h observation of PSR J0023–7203J in the globular cluster 47 Tucanae. (b) Power spectrum of simulated data for a weak 2 ms pulsar in a 50 min orbit about a $0.2 M_{\odot}$ companion. (c) FFT of the shaded region in (a) showing the expected modulation at the 2.9 h orbital period of the pulsar. (d) FFT of the shaded region in (b) showing the 50 min orbital period and two harmonics. Figure provided by Scott Ransom.

6.2.2.4 Dynamic power spectrum search

The various acceleration techniques discussed so far perform optimally for distinct ranges of orbital periods relative to integration time, T . For systems with orbital periods greater than a few times T , coherent one-dimensional acceleration searches (either in the time or frequency domain) usually are adequate. When computational demands are large, and some loss of sensitivity can be tolerated, the stack/slide approach also performs well. When the orbital period is significantly less than T , phase modulation techniques provide a very efficient means of detecting ultra-compact systems. In between the two extremes, there is something of a ‘sensitivity gap’ to pulsars with orbital periods of the order of T .

A promising means of filling this gap is the ‘dynamic power-spectrum’ search. As in the stack/slide search, the time series is split into a num-

ber of smaller contiguous segments which are Fourier-transformed separately. The individual power/amplitude spectra can be summed harmonically and plotted as a two-dimensional (frequency versus time) image. Orbitally modulated pulsar signals appear as sinusoidal signals in this plane (as shown in Figure 6.11).

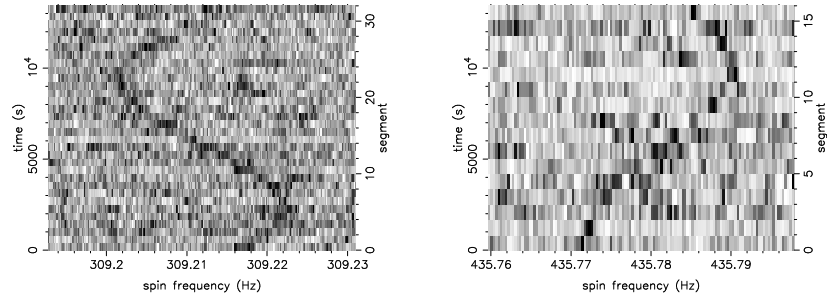


Fig. 6.11. Dynamic power spectra showing two recent pulsar discoveries in the globular cluster M62 showing fluctuation frequency as a function of time. Figure and analysis provided by Adam Chandler.

This technique has been used by various groups where spectra are inspected visually (see, for example, Lyne *et al.* (2000)), or transformed into another representation, e.g. using the Hough transform (Aulbert 2004). Recently, Chandler (2003) has developed a hierarchical scheme for searching these spectra that removes some of the human intervention. This was recently applied to a search of the globular cluster M62 resulting in the discovery of three new pulsars shown in Figure 6.11. One of the new discoveries – M62F, a faint 2.3 ms pulsar in a 4.8 h orbit, was detectable only using the dynamic power spectrum technique.

6.3 Searching for pulsars in the time domain

While the frequency domain techniques described above generally are the most effective and efficient means to find pulsars, there are alternative approaches based in the time domain. Originally developed in the late 1960s, time-domain techniques (fast-folding and single-pulse algorithms) are becoming increasingly popular additions in modern analyses that seek to maximise the volume of phase space covered in pulsar searches.

6.3.1 Fast folding analyses

An essential procedure to check the validity of any good pulsar candidate is to fold² the de-dispersed data modulo the candidate period and examine the resulting pulse profile. This suggests that an alternative means of finding pulsars is to fold each de-dispersed time series modulo many different trial periods and look for statistically significant pulse profiles. Such a simple approach would be extremely effective were it not for the fact that the computational power required to fold over all possible periods of interest is enormous. If, however, we can restrict the search to a limited range of periods then folding provides an attractive alternative to the standard Fourier-based algorithms described above.

Shortly after the development of the FFT, Staelin (1969) devised a clever algorithm that avoids the many redundant operations involved in simple folding analyses. The ‘fast-folding algorithm’ (FFA) works by dividing a time series T_j of N samples into contiguous groups of n samples chosen such that N/n is an integer power of 2. The simplest folding of these data is at a period P_0 that is n times the data sampling interval, i.e. $P_0 = nt_{\text{samp}}$. The folded profile p then consists of n bins, where the k^{th} bin is simply

$$p_k = \sum_{j=0}^{(N/n)-1} T_{k+jn}. \quad (6.19)$$

The FFA works by splitting this summation into $\log_2 n$ stages which can be combined in different ways to fold the data at n slightly different periods. The scheme is best understood with the simple example shown in Figure 6.12 when $N = 16$ and $n = 4$. In this case, there are two stages at which the data are summed to produce four pulse profiles. At each stage, groups of samples are combined with a variable number of time sample shifts between each group. The resulting products represent the accumulated pulse profiles over the appropriate fraction of integration. For example, after the first of the two stages in Figure 6.12, the profiles represent the folded data over half of the integration.

Repeating the FFA procedure over a range of combinations of N and n results in a range of P_0 values that can be searched. The results are best displayed in a periodogram that shows a figure of merit for each folded pulse profile (e.g. reduced χ^2 or S/N; see Chapter 7) versus folding

² The folding procedure is described in detail in Chapter 7.

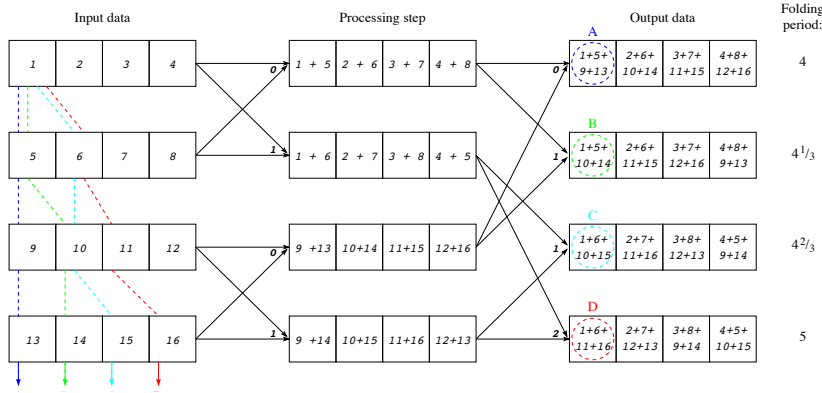


Fig. 6.12. Schematic representation of the fast-folding algorithm applied to a sixteen sample time series that is optimally folded at four different trial periods. Figure provided by Bernd Klein.

period. For a given P_0 , the effective folding period of the l^{th} profile

$$P_l = P_0 + \left(\frac{n+1}{N} \right) l t_{\text{samp}}, \quad (6.20)$$

where $0 < l < (n-1)$. As seen in Figure 6.12, the case $l=0$ reduces to our simple result for P_0 in Equation (6.19). Rather than the $N[(N/n)-1]$ additions required for simple folding, the FFA needs only $N \log_2(N/n)$ additions and therefore becomes very efficient when N is large.

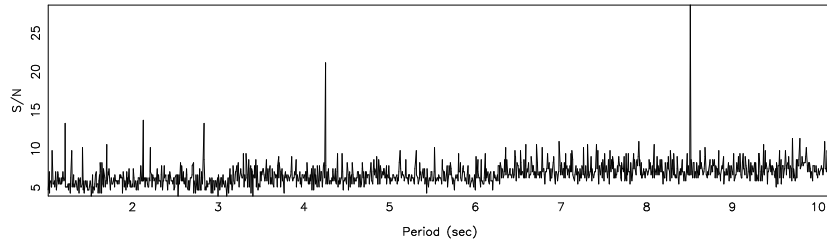


Fig. 6.13. Periodogram output from an FFA showing S/N as a function of trial folding period for an observation of the 8.5 s pulsar J2144–3933. The most significant peak occurs at the pulsar’s true period. Most FFT-based codes enforce a long-period cutoff at around 5 s in order to minimise the effects of red noise in the Fourier domain. This results in the detections of sub-harmonics which are less significant, as shown here.

Even with the efficiency of the FFA over simple folding, the high data sampling rates of current surveys mean that searching the entire

period range of de-dispersed time series is computationally expensive. The FFA can be used to good effect, however, in the search for long-period ($P > 2$ s) pulsars. The standard FFT-based search means that the signals from such pulsars occupy only a small part of the Fourier spectrum at low frequencies. Due to the physical processes mentioned above, this typically can contain a large amount of red noise, which makes such signals hard to detect. Working in the time domain, the FFA reveals the long-period phase space in much greater detail. This is highlighted by Figure 6.13, which shows an FFA periodogram from an observation of the 8.5 s pulsar J2144–3933, the longest period pulsar so far known.

6.3.2 Single-pulse searches

Throughout this chapter we have concentrated on techniques that find pulsars by virtue of their highly periodic nature. The radiation from some pulsars, however, can vary greatly in amplitude so that *detectable* pulses are not strictly periodic. In such cases, the techniques discussed so far cease to become effective. Indeed, by implicitly assuming an underlying periodicity, we may be selecting against the detection of an important part of the neutron star population. Two classes of pulsars for which this is known to be the case are the giant-pulse emitters, from which pulses with between 100 and 1000 times the mean pulse intensity are occasionally emitted, and the nulling pulsars that emit no pulses for extended periods of time (see Chapter 1). The best known giant-pulse emitter – the Crab pulsar – was first discovered through its giant pulses (Staelin & Reifenstein 1968). Many nulling pulsars that emit only a few pulses during an integration would not be detectable in a periodicity search. This was demonstrated by the discovery of J1918+08, a 2.1 s pulsar discovered by a single-pulse analysis of an Arecibo survey of the Galactic plane (Nice 1999). The pulsar was not detected in the original Fourier analysis of the data (Nice, Fruchter & Taylor 1995).

Searching for single pulses in a time series is basically an exercise in matched filtering. Given a time series of predominantly Gaussian noise of known mean and standard deviation, we seek individual events that deviate by several standard deviations from the mean. Consider a rectangular pulse of amplitude S_{peak} and width W . For the optimal case when W is equal to the sampling time t_{samp} , it can be shown (Cordes

& McLaughlin 2003) that the S/N ratio of the pulse

$$\text{S/N} = \frac{S_{\text{peak}}W}{S_{\text{sys}}} \sqrt{\frac{n_p \Delta f}{W}}, \quad (6.21)$$

where S_{sys} is the system equivalent flux density, n_p is the number of polarisations summed and Δf is the receiver bandwidth. For a fixed pulse area (i.e. $S_{\text{peak}}W = \text{const.}$) it follows that $\text{S/N} \propto 1/\sqrt{W}$, i.e. narrow pulses are easier to detect than broader ones. In general, W will not usually be a good match to t_{samp} and the S/N will be less than expected from Equation (6.21). In order to match optimal detection more closely, the time series is ‘smoothed’ by successively adding groups of neighbouring samples and searching for statistically significant events.

As in the Fourier-based searches, a sensible choice of S/N threshold should be made to avoid recording too many candidate pulses that most likely are caused by random noise fluctuations. For the ideal case of Gaussian noise with zero mean and unit standard deviation, Cordes and McLaughlin (2003) show that the number of events expected to occur by chance above some threshold S/N_{\min} is simply

$$n(> \text{S/N}_{\min}) \sim 2n_{\text{samples}} \int_{\text{S/N}_{\min}}^{\infty} \exp(-x^2) dx, \quad (6.22)$$

where n_{samples} is the number of samples in the time series. Requiring that $n < 3$ usually leads to $\text{S/N}_{\min} = 4$. In practice, however, radio frequency interference (Section 6.4) usually increases the number of false detections so that a more practical S/N threshold might be 5–6.

Figure 6.14 shows the single pulse search applied to data from the Parkes multibeam survey. As well as a clear excess of low DM pulses caused by interference, an excess at a DM of $223 \text{ cm}^{-3} \text{ pc}$ is also apparent. No signal was seen in the periodicity search at this DM. Subsequent observations at the same position showed these pulses to have an underlying periodicity of 871 ms and confirmed the existence of a new pulsar J1624–4616. This is one of a number of new pulsars to be confirmed in this way and demonstrates the effectiveness of the single pulse search as a complementary strategy to periodicity searches. Given the simplicity of the algorithm and relatively modest additional computational requirements of a single pulse search, it should soon become a standard part of the pulsar searching procedure.

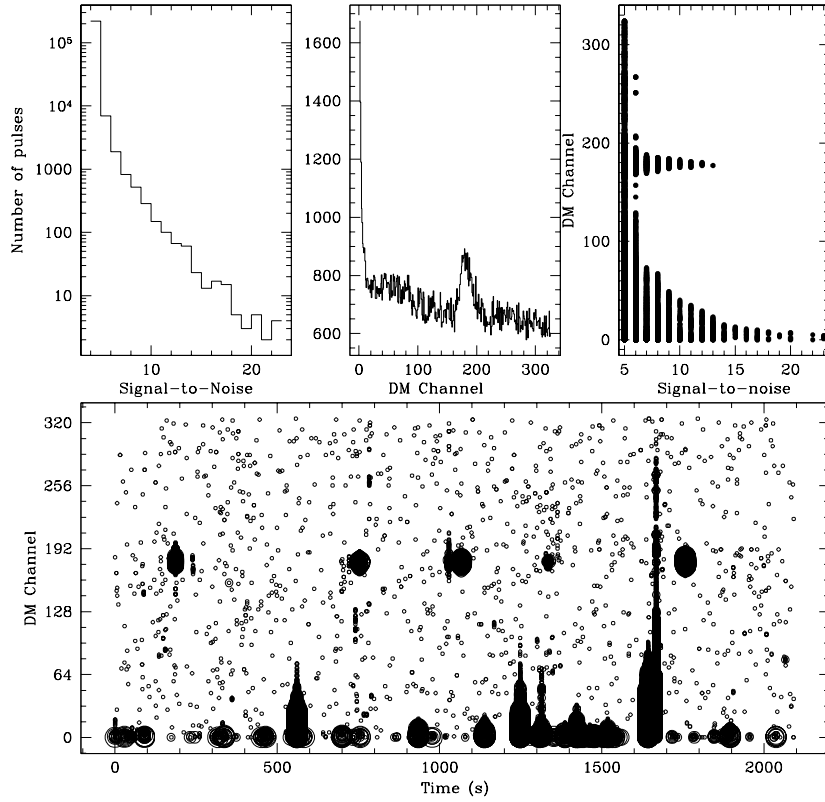


Fig. 6.14. Example output from a single pulse search of data from the Parkes multibeam survey. The top plots show the S/N distribution of the detected pulses, the number of pulses as a function of trial DM as well as S/N as a function of DM. The lower plot shows the individual dispersed pulses as a function of time. The size of the symbols is proportional to the pulse S/N. In addition to the presence of dispersed pulses from, in this case, PSR J1624–4616, persistent interference at low DMs is also apparent. Figure and analysis provided by Maura McLaughlin.

6.4 Radio frequency interference

Even in the remote areas where most radio telescopes are located, terrestrial sources of radio frequency interference (RFI) can have a significant impact on our ability to detect pulsars close to the nominal sensitivity limits of the search. Most search codes have a limit to the number of candidates stored from the analysis. If a particular observation contain-

ing a pulsar is affected badly by RFI, the pulsar may not be strong or persistent enough to be saved as a candidate.

Apart from electrical storms (which can saturate the receiver) the main interference problem arises from persistent broadband signals that mimic the periodic and sometimes even dispersed nature of pulsars. Such sources arise predominantly from nearby electrical devices (the mains power line AC frequency usually is detectable) and communications systems such as airport radar systems. Potential sources of RFI at the observatory, such as desktop computers (which now have clock speeds high enough to radiate in the radio band), also need to be monitored. Fortunately, since most sources of RFI are not dispersed they are detectable in the FFT of the zero-DM time series. Two main approaches to excising these unwanted signals are carried out: time domain clipping and frequency domain masking.

6.4.1 Time domain clipping

Since most searches are expecting to find weak sources, sporadic bursts of interference represent an unwelcome intrusion on the time series. Such samples can be identified easily by comparing them with the expected mean and standard deviation of the zero-DM time series. As an example, a 1-bit filterbank (see Chapter 5) with n_{chans} channels produces time series with an expected mean and standard deviation of $n_{\text{chans}}/2$ and $\sqrt{n_{\text{chans}}}/2$, respectively. A sample is deemed unsuitable for analysis if it differs from the mean value by more than two standard deviations. In such cases, each of the n_{chans} channels are set to zero ('clipped') to exclude them from influencing all subsequent analyses.

Keeping a count of the number of independent samples provides a measure of how badly effected the data are. If this becomes a significant fraction of the total number of samples (e.g. 20 per cent easily can be reached during a bad electrical storm) the observation should be repeated on a subsequent date. This simple procedure is important for time domain analyses like the FFA, particularly for long-period pulsars, in which the integrated profiles can be significantly biased by sporadic RFI.

6.4.2 Frequency domain masking

Most pulsar surveys collect many hundreds or even thousands of observations with the telescope pointing at different parts of the sky. The key

signature of RFI is that it will occur frequently and is independent of sky position. In some cases, the signal is seen predominantly when the telescope is pointing toward the source of the source of RFI, e.g. the local airport! Analysing a large number of zero-DM time series from observations of widely spaced sky positions will show persistent RFI sources occurring at the same frequencies in many or even all of the observations. Usually some sort of conservative threshold is placed, e.g. a signal will be considered to be RFI if it occurs in at least ten out of a hundred independent positions with $S/N > 7$.

This analysis takes place usually on a convenient block of observations, e.g. all those taken in a single observing session or saved to the same magnetic tape. Based on the list of RFI signals that trigger the occurrence threshold, a spectral ‘mask’ is created. This simply is a list of all Fourier bin numbers corresponding to each RFI frequency. The mask then is applied to all subsequent processing by flagging the relevant Fourier bins so that they are ignored by the analysis software.

The spectral mask is an efficient and effective method of RFI excision. A typical mask usually will require less than 1 per cent of all spectral bins to be ignored. While this does leave a small chance that a pulsar with a frequency coincident with a zero-DM RFI signal could be excised from the analysis, masking usually allows data to be analysed that would be otherwise swamped with candidate signals of RFI origin.

6.5 Pulsar search strategies

Having described the various search techniques in use, we now conclude with a brief discussion of the most profitable search strategies. As we shall see, how a pulsar survey is designed determines to a large extent what type of objects are found. It is important to bear in mind the lessons learnt from previous experiments when planning new ones.

6.5.1 Searches close to the plane of our Galaxy

Young pulsars are most likely to be found near to their place of birth, close to the Galactic plane. This is the target region of one of the Parkes multibeam (PM) surveys and has already resulted in the discovery of over 700 new pulsars, almost half the number currently known. Such a large haul inevitably results in a number of interesting individual objects such as: PSR J1141–6545, a young pulsar in a relativistic 4 h orbit around a white dwarf (Kaspi *et al.* 2000b); PSR J1740–3052, a young

pulsar orbiting an $\gtrsim 11 M_{\odot}$ star (Stairs *et al.* 2001); several intermediate mass binary pulsars and two double neutron star systems. For a review on this survey and its major discoveries, see Manchester (2001).

Due to the severe propagation and sky background effects on the sensitivity at low frequencies (< 1 GHz), most Galactic plane surveys are now carried out in the 1–2 GHz band. The centre frequency of the Parkes multibeam system is 1.37 GHz. The generally high pulsar density along the Galactic plane means that deep searches like the PM survey are rewarded by a large yield. One reason for the depth of the PM survey is its relatively long integration time (35 min). While this is an ideal means to maximise the sensitivity to faint isolated pulsars, and those that null, the sensitivity to binary systems is compromised. In order to combat this, the PM survey applies a stack/slide acceleration search similar to that described in Section 6.2.2.2.

6.5.2 All-sky searches for millisecond pulsars

The oldest radio pulsars form a virialised population of stars oscillating in the Galactic gravitational potential. The scale height for such a population is at least 500 pc, about 10 times that of the massive stars that populate the Galactic plane. Since the typical ages of millisecond pulsars are several Gyr or more, we expect, from our vantage point in the Galaxy, to be in the middle of an essentially isotropic population of nearby old and low-luminosity neutron stars.

All-sky searches for millisecond pulsars at high Galactic latitudes have been very effective in probing this population. Much of the initial interest and excitement in this area was started at Arecibo when Wolszczan discovered two exciting pulsars at high latitudes: the double neutron star binary B1534+12 (Wolszczan 1991) and PSR B1257+12 (Wolszczan & Frail 1992), a millisecond pulsar with three orbiting planets. Surveys carried out at Arecibo, Parkes, Jodrell Bank and Green Bank by other groups in the 1990s found many other millisecond pulsars in this way.

Since the interstellar propagation effects (scattering and dispersion) are much less severe away from the Galactic plane, the optimal frequency for these surveys is less than 1 GHz to take advantage of the generally higher flux densities of pulsars at these frequencies (see Section 1.1.3) and the larger telescope beam widths (see Appendix 1). In addition, the short integration times necessary to cover a reasonable area of sky mean that the effects of binary acceleration are far less problematic than deep searches of the Galactic plane.

6.5.3 Searches at intermediate Galactic latitudes

In order to probe more deeply into the population of millisecond and recycled pulsars than possible at high Galactic latitudes, Edwards *et al.* (2001) used the PM system to survey intermediate latitudes in the range $5^\circ < |b| < 15^\circ$. Among the fifty-eight new pulsars discovered, eight are relatively distant recycled objects, including two mildly relativistic neutron star-white dwarf binaries (Edwards & Bailes 2001). The success of this survey has lead to an extension of the search area by two groups. One of these surveys lead to the discovery of the double-pulsar binary system J0737–3039 (Burgay *et al.* 2003; Lyne *et al.* 2004).

6.5.4 Targeted searches of supernova remnants

Ever since the discovery of pulsars, numerous deep surveys of supernova remnants for pulsations from young neutron stars have been carried out. With a few exceptions, these have been surprisingly unsuccessful. The main problem faced by these surveys has been the uncertain position of the putative pulsar, which could lie anywhere within, or around, the vicinity of its associated remnant. This positional uncertainty was quite often much larger than an individual telescope beam width (see Appendix 1) that therefore required a grid of pointings to cover properly the target area. Given that telescope time is always hard-fought, this ultimately leads to a compromise in sensitivity.

This situation has, however, changed quite dramatically with the new generation of X-ray telescopes such as the *Chandra* observatory revealing point-like X-ray emission from within a number of Galactic supernova remnants. These observations suggest strongly the presence of the young neutron star associated with the supernova explosion and, for the first time in most cases, localise the position of the neutron star candidate to sub-arcsecond precision. A number of searches by Camilo and collaborators (see Camilo (2003) for a review) have utilised these positions to carry out very deep searches for pulsations. So far, four young, < 3000 yr old neutron stars have been discovered in these searches. Perhaps not surprisingly, these are all extremely faint objects that are well below the detection threshold of current large-scale surveys. Currently a significant effort is being made to systematically search the known neutron star point sources as deeply as possible.

6.5.5 Targeted searches of globular clusters

Globular clusters have long been known as breeding grounds for millisecond and binary pulsars. The main reason for this is the high stellar density in globular clusters relative to most of the rest of the Galaxy. As a result, low-mass X-ray binaries are almost 10 times more abundant in clusters than in the Galactic disk. In addition, exchange interactions between binary and multiple systems in the cluster can result in the formation of exotic binary systems.

Since a single globular cluster usually fits well within a single telescope beam, deep targeted searches can be made without the positional uncertainty that plagued earlier supernova remnant searches. In addition, once the DM of a pulsar is known in a globular cluster, the DM parameter space for subsequent searches essentially is fixed. This allows computation power to be invested in acceleration searches for short-period binary systems. Multiple observations of clusters also benefit from the occasional boosting of otherwise weak pulsars due to scintillation. To date, searches have revealed eighty pulsars in twenty-four globular clusters. Highlights include the double neutron star binary in M15 (Prince *et al.* 1991), and a low-mass binary system with a 96 min orbital period in 47 Tucanae, one of over twenty millisecond pulsars currently known in this cluster alone (Freire *et al.* 2003). On-going surveys of other clusters continue to yield new discoveries (see, for example, Possenti *et al.* (2003)). It is worth pointing out in this regard that the periodicity searches discussed above do not require any special modification to detect multiple signals in the time series, i.e. provided that the signals are above the noise threshold, the pulsars do not ‘interfere’ with one another.

6.5.6 Searches of the Galactic centre region

A blank spot on the Galactic map of pulsar discoveries has been the Galactic centre region. Not a single radio pulsar has been found in the inner 500 pc around Sgr A*. This is in contrast to the large population of massive stars expected in this region, which is believed to be a site of past and current star formation (see, for example, Mezger *et al.* (1999)). Due to the extreme environment of the Galactic centre (i.e. tidal forces, magnetic field pressure, high gas densities, high temperatures and turbulences) it is believed that the initial mass function should be peaked at a higher mass than in the Galactic disk. This favours more massive

stars probably created by externally triggered star formation (e.g. compression of clouds via collisions). Such massive stars are indeed observed (see, for example, Figer *et al.* 1999).

The increase in the relative importance of high-mass star formation toward the Galactic centre also leads naturally to the expectation of a much larger number density of neutron stars and stellar black holes in comparison to the disk. Moreover, the remnants of massive stars have been detected in the form of supernova remnants (Ekers *et al.* 1983; Kassim & Frail 1996) and possibly neutron stars (Muno *et al.* 2003). Therefore we can expect to find a population of pulsars that would be extremely useful in probing the Galactic centre and its conditions (Kramer *et al.* 1996a; Cordes & Lazio 1997): their number and age distribution would probe the past star formation history (Hartmann 1995); their period derivatives can constrain the gravitational potential in the Galactic centre (see Chapter 8); pulsar timing would enable us to probe the space-time around the super-massive black hole in the Galactic centre due to a variety of relativistic effects (Wex & Kopeikin 1999). The high stellar density of the Galactic centre makes it, like the globular clusters, a possible site of a millisecond pulsar orbiting a stellar-mass black hole. A recent summary can be found in Pfahl and Loeb (2004).

The potential rewards for finding a pulsar in the Galactic centre are high, and searches have been performed. The large distance of ~ 8 kpc to the Galactic centre means that large-area surveys are usually not sensitive enough. The PM survey did have the sensitivity, however, and was still, despite its tremendous success elsewhere, unsuccessful in this region. The reason for the difficulties of finding pulsars around Sgr A* is given by the large amount of interstellar scattering expected for Galactic centre pulsars (Cordes & Lazio 1997). The scattering is so severe that it renders all periodicity searches useless at frequencies below a few GHz. The only way to combat the effects of scattering – which has approximately an f^{-4} dependence (see Chapter 4) – is to search at higher frequencies. Such surveys have been attempted by Kramer *et al.* (1996a; 2000) and Klein (2004) at 4.85 GHz and for a number of selected point sources at 8.5 GHz by Klein (2004). However, increasing system temperatures and the steep spectrum of pulsars (see Chapter 1) worsen the prospects of finding a pulsar at high frequencies. Balancing such effects with the frequency dependence of scattering, Cordes and Lazio (1997) computed an optimal frequency for periodicity searches of Galactic centre pulsars, concluding that the best frequency would lie around 10 GHz. An updated analysis presented by Kramer *et al.* (2000)

is shown in Figure 6.15. At these optimal frequencies the telescope beam usually is too small to cover a large area, in particular for the large telescopes that are required to achieve a sufficient sensitivity. Cordes and Lazio (1997) therefore suggested to find pulsars in targeted searches of steep-spectrum polarised point-sources identified from imaging observations. Ultimately, the best prospects of finding Galactic centre pulsars will be with the Square Kilometre Array (SKA).

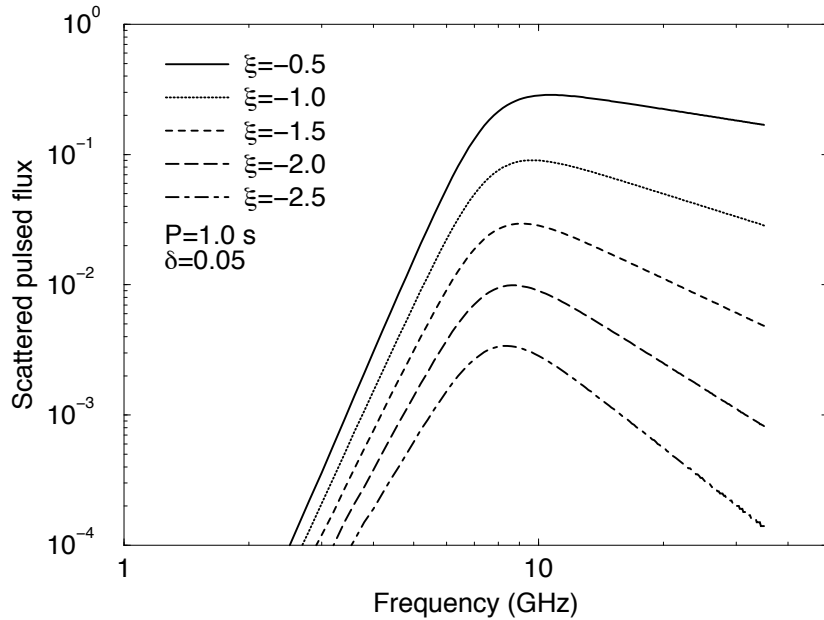


Fig. 6.15. Relative scattered pulsed flux that would be picked up by a periodicity search for a 1 s pulsar in the Galactic centre. Scattering is so severe that it renders the 50 ms wide pulse undetectable at low frequencies. At high frequencies the pulsar spectrum, here shown for various spectral indices ξ , dominates. The optimal search frequencies lies at about 10 GHz.

6.5.7 Searches with the Square Kilometre Array

All the surveys that have been conducted in the past or will be conducted in the next few years appear to be only the prelude to what will be possible with the future SKA. As for other areas in modern astronomy, the SKA will revolutionise the field of pulsar astrophysics. Not only will new science be made possible by the sheer number of pulsars discovered,

but also by the unique timing precision achievable with the SKA. The special property of the SKA will be its unique sensitivity. Current design figures indicate that a $1.5 \mu\text{Jy}$ source will be detectable with $\text{S}/\text{N} = 8$ in a 1 min integration. This will enable not only the discovery of most pulsars in the Milky Way but also allow present-day survey sensitivities to pulsars in the closest galaxies. With the single-pulse search techniques described in Section 6.3.2, it should be possible to detect giant pulses from pulsars as distant as the Virgo cluster.

Pulsar surveys with the SKA essentially could discover all pulsars in our Galaxy that are beaming toward the Earth. From a simulation of a hypothetical all-sky SKA survey we estimate that between 10 000 and 20 000 pulsars, including over 1 000 millisecond pulsars, could be discovered. This impressive yield also samples effectively every possible outcome of the evolution of massive binary stars, thereby guaranteeing the discovery of very exciting systems. Since the integration times of these surveys will be short (5 min or less), compact binaries should be relatively simple to detect. As a result, we expect at least a hundred compact relativistic binaries, including the elusive pulsar–black hole systems. The search, discovery and study of such systems is one of the main science drivers of the SKA.

6.6 Further reading

Although a large number of articles on pulsar searching have been written over the years, we have attempted in this chapter to bring together the various techniques in a single resource. For the reader wishing to gain a deeper insight into the underlying mathematical and signal processing issues discussed throughout this chapter, the excellent text books *Numerical Recipes: The Art of Scientific Computing* (Press *et al.* 1992) and *The Fourier Transform and its Applications* (Bracewell 1998) are highly recommended.

Nowadays, a large number of reliable FFT routines are freely available. Press *et al.* (1992) provide an excellent discussion of why the FFT is so much faster than a DFT, and provide some excellent subroutines in a number of languages. Perhaps the best of the publicly available set of FFT tools is the `fftw` library (www.fftw.org), which is not restricted by the usual power of 2 length requirements.

Early work on pulsar search methodologies was summarised by Burns and Clark (1969) and Hankins and Rickett (1975). An excellent introduction to pulsar searching also can be found in the review by Bhat-

tacharya (1998). Further discussions of the two-dimensional Fourier transform search can be found in Lyne and Smith (2005). Two seminal papers (Ransom *et al.* 2002; 2003a) contain excellent discussions on Fourier domain search techniques. Many of the results quoted in Sections 6.1.3 and 6.2 were developed or discussed in detail for the first time in these papers. Further discussion on the phase-modulation search technique can be found in Jouteux *et al.* (2002). The single-pulse search methods described by Cordes and McLaughlin (2003) and McLaughlin and Cordes (2003) are highly recommended for those wishing to explore these techniques in more detail. A number of aspects concerning pulsar search design and optimisation not discussed here can be found in the excellent review by Cordes (2002). Camilo (1995; 1997; 1999) has written several reviews of pulsar surveys that are good starting points for further reading.

6.7 Available resources

While numerous pulsar search software packages have been developed over the years, only a few are freely available for use. Two currently available packages are PRESTO, developed by Scott Ransom, and SEEK developed by one of us (DRL). Both programs are well tested and have a complementary approach to pulsar searching in the Fourier domain. PRESTO makes full use of the phase information and can be used to carry out sophisticated acceleration and phase modulation searches for pulsars. To date it has been used to great success by Ransom and collaborators (Ransom *et al.* 2003b). SEEK closely follows the standard search approach and has been used successfully in a wide range of different projects. Also incorporated into the package are time domain resampling routines to carry out acceleration searches (used to great effect in searches of 47 Tucanae; see Camilo *et al.* (2000b)) as well as the single-pulse search routines developed by Cordes and McLaughlin (2003). Peter Müller has written an FFA program that has been adapted by one of us (MK) for general use in pulsar searches. Links to all of the above programs and sample data sets that can be used as starting-points for those wishing to develop and test their own software can be found on the book web site, (see Appendix 3).

7

Observing known pulsars

Once a pulsar has been discovered, it is subject to many different types of follow-up observations first in order to characterise its basic properties and later to study it in more detail. In this chapter, we discuss the most commonly used techniques necessary to carry out these observations. A fundamental procedure underpinning most pulsar observations is the synchronous averaging (folding) of the data at the pulse period. Following a description of this process, we discuss the various preliminary observations required to refine pulsar parameters for future observations. These amount basically to an optimisation of the pulse period, dispersion measure and position, as well as determining whether the pulsar is in a binary system. Then we discuss flux density and polarisation calibration procedures, before moving on to review the most commonly used modes of observation and data analyses: single-pulse studies, polarisation and Faraday rotation measurements, scintillation observations and measurements of neutral hydrogen absorption. Finally, some techniques to remove radio-frequency interference from the data are discussed.

7.1 Folding

As pulsars are generally very weak radio sources, the addition (folding) of many pulses so that the signal is visible above the background noise is vital for studying them in detail. Folding can be summarised as follows:

- (i) De-disperse the data either coherently (see Section 5.3) or incoherently (see Sections 5.2 and 6.1.1.1). The resulting time series has a sampling time t_{samp} .
- (ii) Create an array for storing the folded profile with n_{bins} equally spaced elements (known as ‘bins’) across the pulse period. Each

bin therefore corresponds to a particular phase of the pulse, where the phase centre of bin i is simply $(i - 0.5)/n_{\text{bins}}$.

- (iii) Take a sample of the time series and calculate its phase relative to the pulse period. In the simplest case of a constant pulse period, P , the phase of the j^{th} sample is jt_{samp}/P , where t_{samp} is the data sampling interval.
- (iv) Find which bin in the profile array has the closest phase to this sample and add the sample to this bin.
- (v) Repeat step (iii) for the next sample.

At the end of this process, each phase bin in the folded profile is normalised by the number of samples accumulated per bin. The resulting *integrated pulse profile* represents the average emission from the neutron star as a function of its rotational phase. This algorithm can be extended easily to write out profiles corresponding to short contiguous segments of data (*sub-integrations*), or single pulses (see Section 7.4.2).

The above approach to folding using a constant pulse period usually applies to early observations of a pulsar for which only the discovery period is known. More generally, when high-precision ephemerides are available from timing observations (see Chapter 8), the phase of each sample can be calculated directly. For computational efficiency, an intermediate program is used to interpolate the ephemeris into a set of polynomial coefficients. These then can be used to calculate the phase with sufficient accuracy for the epoch of the observation to avoid any smearing of the pulse due to drifting (see Section 7.2.1). Software packages to carry out these tasks are detailed at the end of this chapter.

7.1.1 Profile significance tests

A quantitative figure of merit for a pulse profile is useful both for calibration issues discussed later and for assessing the significance of weak detections. Representing the profile as an array of n_{bins} phase bins for which the amplitude of i^{th} bin is labelled p_i , in the following we consider two significance measures that are in common use: (a) the profile signal to noise ratio, S/N; (b) the chi-squared statistic, χ^2 .

Both measures of significance require the off-pulse mean¹, \bar{p} , and standard deviation, σ_p . These quantities may be calculated by isolating the on- and off-pulse emission in a process known as pulse *windowing* or *gating*. An alternative method is to calculate the mean and standard devia-

¹ This is sometimes referred to as the profile baseline, DC level or offset.

tion of a short (~ 1 s) segment of the raw time series which is essentially dominated by noise. This is particularly useful for broad pulse profiles where there is little off-pulse emission in the folded profile. If we denote these ‘raw’ values by \bar{r} and σ_r , for a folding scheme where the resulting pulse profiles are normalised by the number of samples accumulated per phase bin, it can be shown that $\bar{p} = \bar{r}$ and $\sigma_p = \sigma_r / \sqrt{(n_{\text{samples}}/n_{\text{bins}})}$, where n_{samples} is the total number of samples in the time series.

7.1.1.1 Signal to noise ratio

The most commonly-used measure of profile significance is the signal to noise ratio, S/N, usually defined as follows:

$$\text{S/N} = \frac{1}{\sigma_p \sqrt{W_{\text{eq}}}} \sum_{i=1}^{n_{\text{bins}}} (p_i - \bar{p}), \quad (7.1)$$

where W_{eq} is the equivalent width (in bins) of a top-hat pulse with the same area and peak height as the observed profile. As defined in Chapter 3, W_{eq} is simply the area under the observed pulse divided by its peak height. Assuming the noise distribution follows Gaussian statistics, the probability of obtaining a profile with a particular S/N by chance

$$\text{Prob}(> \text{S/N}) = \frac{1}{\sqrt{2\pi}} \int_{\text{S/N}}^{\infty} e^{-x^2/2} dx = \frac{1}{2} \left[1 - \text{erf} \left(\frac{\text{S/N}}{\sqrt{2}} \right) \right], \quad (7.2)$$

where the error function $\text{erf}(x) = (2/\sqrt{\pi}) \int_0^x \exp(-t^2) dt$ can be solved numerically (see, for example, Press *et al.* (1992)).

7.1.1.2 Chi-squared statistic

An alternative measure of a profile’s significance is to consider its deviation from pure Gaussian noise with mean \bar{p} and variance σ_p^2 . This test was first used to quantify folding analyses of X-ray data by Leahy *et al.* (1983) who defined a version of the χ^2 statistic

$$\chi^2 = \frac{1}{\sigma_p^2} \sum_{i=1}^{n_{\text{bins}}} (p_i - \bar{p})^2, \quad (7.3)$$

which, for this simple model, has $n_{\text{bins}} - 1$ degrees of freedom. The significance level for a given χ^2 value can be calculated readily by noting that the probability of exceeding a given χ^2 value by chance

$$\text{Prob}(> \chi^2) = \frac{1}{\Gamma(a)} \int_{\chi^2/2}^{\infty} e^{-t} t^{a-1} dt, \quad (7.4)$$

where $a = (n_{\text{bins}} - 1)/2$ and $\Gamma(a) = \int_0^\infty t^{a-1} e^{-t} dt$. Press *et al.* (1992) provide routines to integrate this function numerically.

7.2 Preliminary measurements

Following a pulsar's discovery, its period, dispersion measure and position usually are rather crudely known. Periods and dispersion measures often are limited to the resolution of the search technique (see Chapter 6). Positional uncertainties usually are at the level of the resolution of the radio telescope beam (typically ~ 10 arcmin; see Appendix 1). By reducing the uncertainties in all these parameters through preliminary measurements, we can facilitate greatly the planning and efficiency of subsequent observations. In addition, if a pulsar is a member of a binary system, an initial orbital ephemeris can often be determined.

7.2.1 Improving the pulse period

As well as the limited precision from the search, the pulsar's period may have altered from the discovery/confirmation observation due to the presence of an orbiting companion, a high spin-down rate or period glitch. As the grey-scale plot of sub-integration against pulse phase in Figure 7.1 shows, folding the data at a slightly incorrect period will cause the accumulated profile to drift in phase so that the integrated pulse will appear significantly broadened and with reduced S/N.

The period can, however, easily be corrected by measuring the drift rate of the pulse in the incorrectly folded data. To quantify this, consider folding a time series at period P that differs by δP from the true period P_{true} . The drift rate in one period $\dot{P} = \delta P/P$ is small but easily measurable through its accumulation over a longer period of time. If the pulse is observed to drift by an amount Δt over an observation of length t_{obs} , then $\dot{P} = \Delta t/t_{\text{obs}}$ and, hence,

$$P_{\text{true}} = P + \delta P = P + P\dot{P} = P \left(1 + \frac{\Delta t}{t_{\text{obs}}} \right). \quad (7.5)$$

For the drift rate of 111.95 ms measured in Figure 7.1, the data can be re-folded at the correct period to restore the true pulse shape as shown. Any residual drifts when folding the data with period P_{true} are now within a phase bin and the uncertainty of the corrected period $\Delta P_{\text{true}} = P_{\text{true}}^2/(n_{\text{bins}} t_{\text{obs}})$. The period is now sufficiently precise to produce a folded profile for use in timing analyses (see Chapter 8).

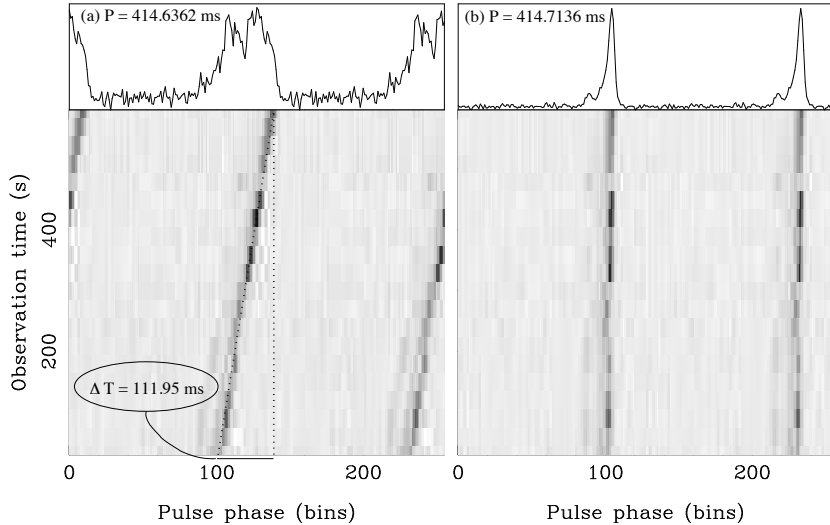


Fig. 7.1. (a) A time series for PSR J0137+1654 folded at a slightly incorrect period. The pulse drifts by ~ 112 ms during the integration. (b) The same time series folded at the period corrected using the measured drift rate.

Looking at this simple analysis another way: for a pulsar of constant period, the fractional folding period uncertainty as a function of time required to keep phase drifts within a single bin is $P/(n_{\text{bins}}t_{\text{obs}})$. This is shown for 512-bin profiles of different pulse periods in Figure 7.2 and gives an idea of the precision required and achievable in folding analyses.

For pulsars in binary systems, as we saw in Chapter 6, the apparent pulse period changes due to time-variable Doppler shifts as the pulsar moves about the centre of mass of the binary system. The simple approximation of a constant folding period is therefore no longer valid. This is noticeable particularly for observations of short orbital period binaries ($P_b \lesssim 24$ h) and long integration times ($t_{\text{obs}} \gtrsim 5$ min). First and higher order period derivatives are often required to avoid drifts due to binary motion when folding the data, i.e.

$$P(t) = P_{\text{true}} + \dot{P}_{\text{bin}}t + \frac{1}{2}\ddot{P}_{\text{bin}}t^2 + \dots, \quad (7.6)$$

where the ‘bin’ subscripts denote period derivatives due to binary motion. For example, the 22 min observation of the 7.75 h binary pulsar B1913+16 discussed in Section 6.2.1 requires an additional $\dot{P}_{\text{bin}} \simeq 3 \times 10^{-9}$ in order to fold the data correctly. These derivatives can be used

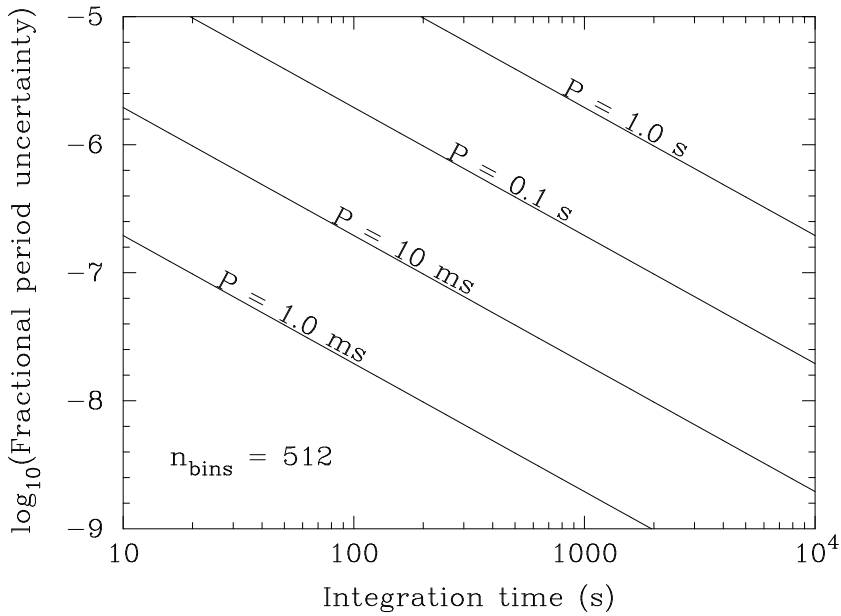


Fig. 7.2. Graph showing the fractional folding period uncertainty required to produce a 512-bin pulse profile for various pulse periods as a function of integration time.

to constrain the orbital parameters of the binary system, in particular \dot{P}_{bin} , which we will discuss further in Section 7.2.4.

7.2.2 Improving the dispersion measure

Although the dispersion measure (DM) resolution of a periodicity search usually is chosen to provide a good indication of a pulsar's DM (see Section 6.1.1.2) it is often useful to refine the estimate by de-dispersing the data into a number of sub-bands and folding at the best period obtained from the above analysis. By analogy with the period optimisation, an improved estimate for DM can be found if the pulse profile is delayed across the de-dispersed sub-bands. For a delay Δt (s) over a total bandwidth Δf (MHz), a better DM estimate

$$\text{DM}_{\text{improved}} = \text{DM} + 1.21 \times 10^{-4} \left(\frac{\Delta f^3}{f} \right) \Delta t \text{ cm}^{-3}\text{pc}, \quad (7.7)$$

where f (MHz) is the centre frequency. This improved estimate usually is quite adequate to de-disperse all subsequent observations. For high

precision DM determinations, observations at widely spaced frequencies can be used directly in a timing analysis (see Chapter 8).

At this point it is worth mentioning that when attempting to get the best resolution out of incoherent devices such as filterbanks and correlators (see Sections 5.2.1 and 5.2.2) it is often preferable to fold the individual frequency channels separately. If a single de-dispersed profile is required, the most precise method is to Fourier-transform the resulting profiles and apply the shift theorem in the Fourier domain to rotate the phase of each profile to a common reference frequency. For example, denoting the k^{th} Fourier component of a single profile by

$$\mathcal{P}_k = \sum_{j=0}^{n_{\text{bins}}-1} p_j \exp(-2\pi ijk/n_{\text{bins}}), \quad (7.8)$$

where as usual $i = \sqrt{-1}$, and an arbitrary time shift t_0 is achieved by multiplying each \mathcal{P}_k by the factor $\exp(2\pi ikt_0/P)$. Choosing t_0 appropriately using the dispersion relation (see Equation (4.6)), the profile corresponding to each frequency channel then can be shifted relative to some common reference frequency. The resulting Fourier coefficients of each shifted profile then are summed before applying the inverse Fourier transform to obtain a single de-dispersed profile back in the time domain. For detailed observations, this more exact approach is preferable over a ‘search-mode’ de-dispersion where integer bin shifts are used (see, for example, Section 6.1.1.1).

7.2.3 Improving the position

Aside from pulsars discovered in targeted searches of radio or high-energy point sources where positions are known to high precision (see, for example, Camilo (2003)), the initial position of most newly discovered pulsars has an uncertainty comparable to the size of the radio telescope beam. Since even a small error in position produces large effects in timing analyses (see Chapter 8), pulsar timing is simplified greatly when the positional uncertainty is small.

Although interferometric determinations of pulsar positions offer one means of improving the position (see Chapter 9), a useful means of reducing the positional uncertainty via single-dish observations is the so-called ‘gridding’ scheme developed for pulsars discovered in the Parkes multibeam survey (Morris *et al.* 2002). As part of the confirmation procedure, each pulsar from the survey was observed in five positions:

the nominal search position, and four offset² pointings: north, south, east and west of the true position. Folding the data at each position results in several detections clustered around the nominal position. The average position of the detections, weighted by the profile S/N, provides a more accurate determination of the true position.

By comparing these positions with the final values determined from timing observations, Morris *et al.* (2002) demonstrated that the gridding procedure reduced the root mean square scatter between estimated and true positions by a factor of about 4.4. As well as the reduced uncertainties in the timing analysis, the improved positions reduce the pointing offset between the telescope and the pulsar and therefore provide greater S/N in subsequent observations. This reduces the subsequent amount of observing time required to obtain a satisfactory detection and therefore increases the overall observing efficiency.

7.2.4 Orbital determination

In the case of binary pulsars, the orbital parameters need to be taken into account to provide an ephemeris suitable for correctly folding the data. As these parameters initially are unknown, their determination begins as an iterative procedure. Several observations, ideally closely spaced, are used to determine the pulse period at each epoch using the period optimisation procedure described in Section 7.2.1.

Care should be taken at this stage to remove the effects of the motion of the Earth from the data that will Doppler-shift the observed pulse periods with a 1 year orbital period! Unless the time series has already been corrected for this effect prior to folding (see Section 6.1.2), the observed pulse periods and epochs should be converted appropriately to the equivalent values at the Solar System barycentre (SSB). Software tools to perform this conversion are available on the book web site (see Appendix 3).

For a binary orbit, a graph of observed period P_{obs} versus time can be fitted to a simple Keplerian model:

$$P_{\text{obs}} = P_{\text{int}}(1 + V_l(t)/c). \quad (7.9)$$

Here P_{int} is the intrinsic period of the pulsar and $V_l(t)$ is its projected velocity along the line of sight as a function of time t . Full details of the Keplerian orbital prescription for $V_l(t)$ are given in Chapter 8.

² In this case, based on the 14 arcmin half-power beam width of the Parkes telescope, the offset was chosen to be 9 arcmin.

Figure 7.3(a) shows an example orbital fit to a set of data points for the long-period binary pulsar J0407+1607 (Lorimer *et al.* 2004b).

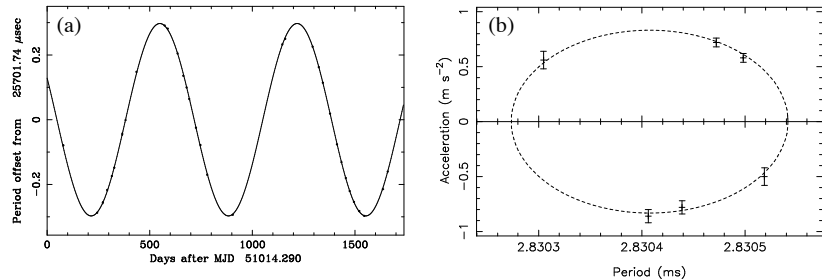


Fig. 7.3. (a) Keplerian orbital fit to the 669-day binary pulsar J0407+1607 showing the observed barycentric periods as a function of time. (b) Orbital fit in the period–acceleration plane for the globular cluster pulsar 47 Tuc S.

For pulsars that are less frequently detectable, (e.g. weak pulsars in globular clusters which are prone to scintillation) the density of observations may not be sufficient to resolve orbital period ambiguities using the above technique. In these cases, Freire *et al.* (2001) demonstrated that if, in each observation a significant period derivative due to orbital motion can be detected (as described in Section 7.2.4), the data points for any given orbit will map out a closed loop in \dot{P} – P space. Alternatively, since the line of sight component of the orbital acceleration $a_l = \dot{P}c/P$ can be determined through an acceleration search (see Section 6.2.1), the orbit also can be viewed in a_l – P space. For a circular orbit, the loop is an ellipse as shown in Figure 7.3. Fitting a model ellipse to these data points, Freire *et al.* (2001) were able to determine the orbital period and semi-major axis from these sparsely-sampled data points. Without the use of this technique, it would have been practically impossible to obtain an initial timing solution.

7.3 Calibrating pulsar data

As with most areas of astronomy, pulsar data do not automatically come from the telescope in physically meaningful units. In particular, the output of pulsar data acquisition devices is designed to be compact. The data are quantised and, depending on the data acquisition device, recorded with a range of precision ranging between 1 and 32 bits per sample. The post-observation treatment of pulsar data is not truly complete before some sort of calibration from ‘machine units’, which we will

hereafter refer to simply as *counts*, to flux density in Janskys (Jy) measured by the telescope. Although for some applications (e.g. timing and scintillation studies) one can often ‘get away’³ without performing any calibration procedures, for other studies (e.g. polarimetry and spectral measurements) calibration is essential. In general, we recommend that calibration is carried out routinely so that data can be used for many purposes, e.g. flux density determinations from data taken originally for timing observations.

In the following discussion, we begin in a fairly simple manner by considering various schemes to calibrate the flux density scale (see Sections 7.3.1 and 7.3.2). Although these simple estimates are instructive, we recommend that observers make use of a noise diode signal, as we describe in Section 7.3.3, to calibrate more reliably their data wherever possible. Polarisation calibration then will be discussed relative to this flux density scale in Section 7.3.4. Those unfamiliar with the radio-astronomical terminology used below should consult Appendix 1.

7.3.1 Flux density estimates from the signal to noise ratio

Two particular quantities are of interest: (a) the peak flux density (i.e. the maximum point on the folded profile); (b) the mean flux density (i.e. the area under the pulse divided by the period). The mean flux density represents the flux density of a pulsar if it were a continuum source, and is sometimes known as the *equivalent continuum flux density* and is the standard quantity used to interpret the strength of the signal.

The simplest way to estimate the flux density of a folded profile is from its S/N ratio and the (presumed known) local observing system parameters. In Appendix 1 we show that if a pulsar of period P (s) and equivalent width W (s) is observed with a given S/N, then its mean flux density

$$S_{\text{mean}} = \frac{(S/N) \beta T_{\text{sys}}}{G \sqrt{n_p t_{\text{obs}} \Delta f}} \sqrt{\frac{W}{P - W}}. \quad (7.10)$$

Here, β is a correction factor accounting for imperfections in the system due to finite digitisation (Chapter 5), T_{sys} is the system noise temperature (K), G is the gain of the telescope (K Jy⁻¹), n_p is the number of polarisations summed, Δf is the observing bandwidth (MHz) and t_{obs} is the observation length (s). With this choice of units, we find S_{mean} in mJy from this expression.

³ The authors are as guilty of this crime as others!

As well as measuring S/N and equivalent width (see Section 7.1.1.1), care should be taken to obtain the most appropriate values for the other parameters in Equation (7.10). As explained in Appendix 1, the system noise is the sum of the receiver noise temperature T_{rec} (typically > 20 K), sky background temperature T_{sky} and the ‘spillover’ noise from the ground T_{spill} . The sky background temperature, a strong function of observing frequency and position, can be estimated from the Haslam *et al.* (1982) all-sky survey. The spillover noise T_{spill} and telescope gain G usually depend on the telescope elevation.

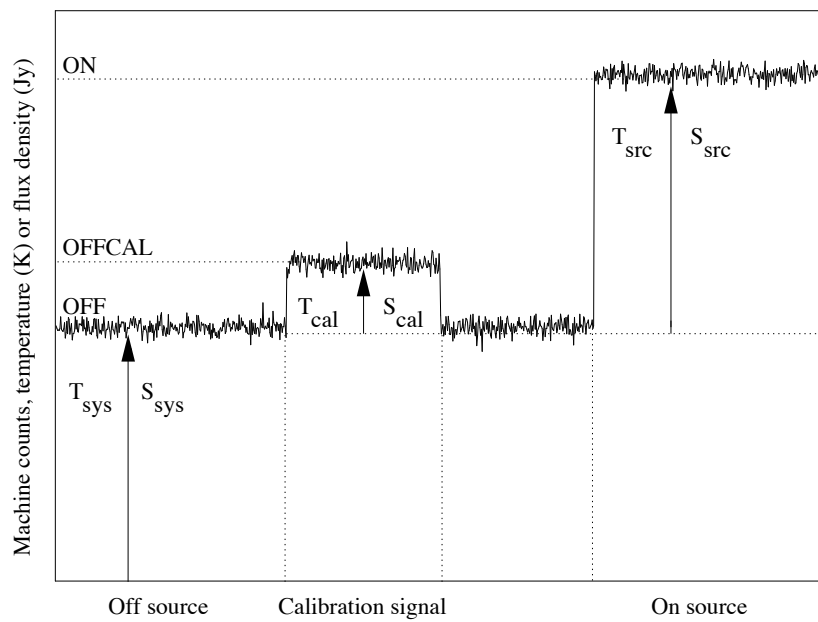


Fig. 7.4. Schematic showing the relationship between machine counts, antenna temperature and flux density during a typical system calibration measurement.

A straightforward means of determining T_{sys} for the purposes of this calculation is to observe a stable radio continuum source with a well-known flux density S_{src} and record the mean number of machine counts received in an *off-source* position, i.e. a nearby patch of sky containing no strong radio sources. As shown in Figure 7.4, the on-source counts (ON) are proportional to the system noise plus the source, while the off-source counts (OFF) represent just the system noise. This means

that

$$\frac{\text{ON} - \text{OFF}}{\text{OFF}} = \frac{T_{\text{src}}}{T_{\text{sys}}}, \quad (7.11)$$

where $T_{\text{src}} = GS_{\text{src}}$ is the antenna temperature due to the source.

7.3.2 Flux density estimates from the system noise

Strictly speaking, Equation (7.10) is valid for top-hat pulses. A more general approach is to note that the DC level (off-pulse mean) of a pulse profile, \bar{p} , corresponds in counts to the system equivalent flux density of the observing system $S_{\text{sys}} = T_{\text{sys}}/G$ in Jy (see Appendix 1). If T_{sys} and G of the telescope are known, a Jy scale for the profile can be established readily by subtracting the DC offset from the uncalibrated profile and multiplying the result by the factor $G\bar{p}/T_{\text{sys}}$. The peak flux density can be read off the scale directly. The mean flux density is simply the area under the pulse divided by the number of bins across the profile.

A similar procedure makes use of the standard deviation of the off-pulse part of the profile, σ_p . From the radiometer equation (see Appendix 1), we expect the root mean square noise fluctuations in Jy

$$\Delta S_{\text{sys}} = \frac{T_{\text{sys}}}{G\sqrt{n_p t_{\text{obs}} \Delta f}} = C\sigma_p, \quad (7.12)$$

where C is the required scaling factor in units of Jy per count. The profile can be calibrated into Jy by simply subtracting \bar{p} and multiplying by C .

7.3.3 Accurate flux density determination

In all three of the above procedures, we assume that the contribution to T_{sys} from the sky background and spillover terms is the same when observing the calibrator source and the pulsar. In practice this may not be correct, even approximately, and the resulting flux densities may contain systematic errors. A more robust approach is to use a semiconductor diode to inject white noise into the receiver system at the waveguide. If the corresponding antenna temperature of the noise diode (T_{cal}) can be measured, then it can be used to establish the flux density scale rather than T_{sys} . Returning to the above measurement of T_{sys} shown in Figure 7.4, we can establish T_{cal} by making one additional measurement of the counts when the noise diode is added during the

off-source pointing (OFFCAL). By the same logic as before,

$$\frac{T_{\text{cal}}}{T_{\text{sys}}} = \frac{\text{OFFCAL} - \text{OFF}}{\text{OFF}}. \quad (7.13)$$

Combining this with Equation (7.11) to eliminate T_{sys} , we find

$$\frac{S_{\text{cal}}}{S_{\text{src}}} = \frac{T_{\text{cal}}}{T_{\text{src}}} = \left(\frac{\text{OFFCAL} - \text{OFF}}{\text{ON} - \text{OFF}} \right), \quad (7.14)$$

where S_{cal} and S_{src} are the (corresponding) equivalent flux densities of the calibration signal and source, respectively. Based on the known value for S_{src} , S_{cal} can be determined readily from these simple measurements that are independent of the gain and system temperature.

In practice, there are a number of ways the calibration signals can be used to establish the flux density scale for pulsar observations. Three commonly used variants are:

- (i) *Carry out multiple observations with the diode switched alternately on and off.* The counts/Jy scaling factor can be readily determined from the difference in the DC levels of pulse profiles when the calibration signal is on and off. This technique is used routinely at Jodrell Bank (see, for example, Gould and Lyne (1998)).
- (ii) *Pulse the noise diode at a fixed frequency and fold the signal as if it were a pulsar.* This produces a square-wave profile where the required counts/Jy scaling factor again is simply the difference between the on- and off-pulse levels. These ‘pulsed cals’ are in fairly common use at telescopes such as Arecibo and Parkes.
- (iii) *Pulse the noise diode synchronously at the pulsar period.* Normally this is arranged so that the calibration signal occupies a part of the profile at which no pulsed emission is expected. The area under the pulsar’s waveform can be calculated directly from the known area under the calibration signal. This system is used at the Effelsberg telescope (Seiradakis *et al.* 1995).

7.3.4 Polarisation calibration

As reviewed in Chapter 1, pulsars are highly polarised radio sources. Polarisation measurements can yield a wealth of information, not only about the emission process itself, but also about the medium through which it propagates. One example is the structure of the Galactic magnetic field through Faraday rotation measurements. Before discussing

such observations, we outline first the considerations required to calibrate the data properly.

As summarised in Appendix 1, the polarisation state of the signal can be described fully by the four Stokes parameters: I , Q , U and V . These may be expressed conveniently as a column matrix known as the Stokes vector:

$$\mathcal{S} = \begin{bmatrix} I \\ Q \\ U \\ V \end{bmatrix}. \quad (7.15)$$

In practice, the measured Stokes vector $\mathcal{S}_{\text{measured}}$ will be different from the intrinsic vector \mathcal{S}_{int} for a number of reasons related to the telescope and observing system. Before discussing specifics, we can summarise the combination of these effects by the Mueller matrix \mathcal{M} (Mueller 1948) which acts as a transfer function between the measured and true Stokes parameters:

$$\mathcal{S}_{\text{measured}} = \mathcal{M} \times \mathcal{S}_{\text{int}}. \quad (7.16)$$

By calibrating the observing system, we can determine \mathcal{M} and, hence, solve this equation for the true Stokes vector \mathcal{S}_{int} . Following a number of authors (see, for example, Heiles *et al.* (2001)), we can express the Mueller matrix as a set of independent matrices:

$$\mathcal{M} = \mathcal{M}_{\text{Amp}} \times \mathcal{M}_{\text{CC}} \times \mathcal{M}_{\text{Feed}} \times \mathcal{M}_{\text{PA}}, \quad (7.17)$$

where the various terms will be outlined next. Note that, due to the non-commutative nature of matrix algebra, the ordering of the terms here is important! Therefore we proceed from right to left in this expression to follow the order in which the various effects take place.

The first effect applies to any ‘alt-azimuth’ radio telescope tracking a source across the sky and occurs because the feed rotates with respect to the plane of polarisation by the *parallactic angle*

$$\text{PA} = \arctan \left(\frac{\sin \text{HA} \cos \phi}{\sin \phi \cos \delta - \cos \phi \sin \delta \cos \text{HA}} \right), \quad (7.18)$$

where HA is the hour angle of the source of declination δ and ϕ is the latitude of the observatory. The effect of a change in PA during the observation is a phase rotation of the Stokes vector by 2PA. The

associated Mueller matrix

$$\mathcal{M}_{\text{PA}} = \begin{bmatrix} 1 & 0 & 0 & 0 \\ 0 & \cos 2\text{PA} & \sin 2\text{PA} & 0 \\ 0 & -\sin 2\text{PA} & \cos 2\text{PA} & 0 \\ 0 & 0 & 0 & 1 \end{bmatrix}. \quad (7.19)$$

Although elliptical feeds are possible, the incoming radiation is in general sampled by either linear or circular probes. In general, we can write the Mueller matrix for the feed as follows

$$\mathcal{M}_{\text{Feed}} = \begin{bmatrix} 1 & 0 & 0 & 0 \\ 0 & \cos 2\gamma & 0 & \sin 2\gamma \\ 0 & 0 & 1 & 0 \\ 0 & -\sin 2\gamma & 0 & \cos 2\gamma \end{bmatrix}, \quad (7.20)$$

where $\gamma = 0^\circ$ is the case for a dual linear feed and $\gamma = 45^\circ$ implies a dual circular feed. In general, however, the feeds are not perfect, so that the output from the two supposedly orthogonal probes is coupled. We can express this *cross-coupling* effect by the following Mueller matrix

$$\mathcal{M}_{\text{CC}} = \begin{bmatrix} 1 & 0 & A & B \\ 0 & 1 & C & D \\ A & -C & 1 & 0 \\ B & -D & 0 & 1 \end{bmatrix}, \quad (7.21)$$

where the constants are defined in the magnitude and phase (ϵ and ϕ) of the cross coupling from probe 1 to probe 2, i.e.

$$A = \epsilon_1 \cos \phi_1 + \epsilon_2 \cos \phi_2 \quad (7.22)$$

$$B = \epsilon_1 \sin \phi_1 + \epsilon_2 \sin \phi_2 \quad (7.23)$$

$$C = \epsilon_1 \cos \phi_1 - \epsilon_2 \cos \phi_2 \quad (7.24)$$

$$D = \epsilon_1 \sin \phi_1 - \epsilon_2 \sin \phi_2. \quad (7.25)$$

Finally, the two signals pass through slightly different amplifier chains that introduce different gains and phases on the signals. Considering just the differential gain and phase, ΔG and $\Delta\psi$, following Heiles *et al.* (2001) we can write to first order:

$$\mathcal{M}_{\text{Amp}} = \begin{bmatrix} 1 & \Delta G/2 & 0 & 0 \\ \Delta G/2 & 1 & 0 & 0 \\ 0 & 0 & \cos \Delta\psi & -\sin \Delta\psi \\ 0 & 0 & \sin \Delta\psi & \cos \Delta\psi \end{bmatrix}. \quad (7.26)$$

With the above set of Mueller matrices, it is possible to describe the

variation of measured Stokes parameters as a function of parallactic angle. Determination of the matrix parameters requires expanding Equation (7.16) into four simultaneous equations for the measured Stokes parameters that can then be solved for the system parameters by least-squares fits to data observed over a wide range of parallactic angles.

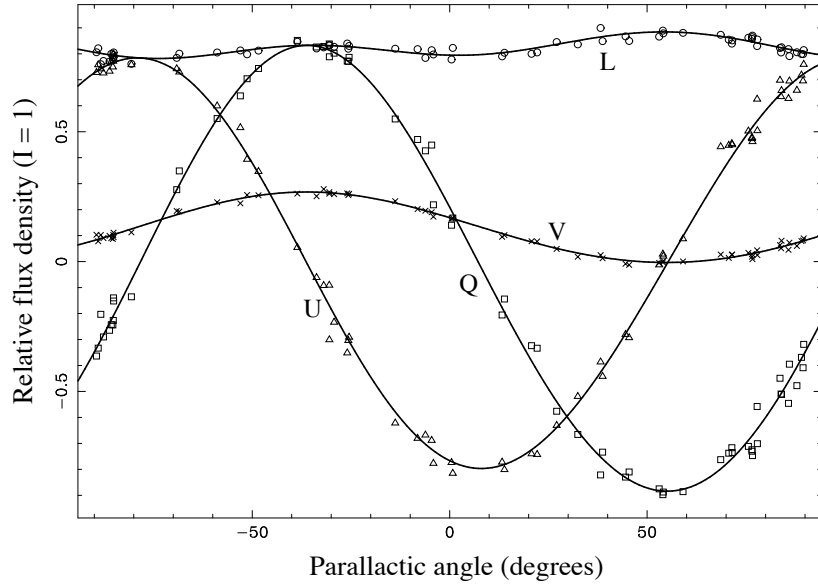


Fig. 7.5. The data points show measured Stokes parameters Q , U and V as well as the linear polarisation $L = \sqrt{Q^2 + U^2}$ for PSR J1359–6038 as a function of parallactic angle (Johnston 2002). The fitted curves define the Mueller matrix of the system allowing the true Stokes parameters to be inferred. Figure and analysis provided by Simon Johnston.

Early attempts to determine the Mueller matrix parameters (see, for example, Stinebring *et al.* (1984)) were hampered somewhat by the computational power required to perform the fitting and matrix inversion process and a number of simplifications were often made. However, as pointed out by Johnston (2002), modern computers can solve Equation (7.16) easily and without loss of generality. As an example, we show Johnston's fits to calibration data in Figure 7.5. In this case, the highly polarised pulsar J1359–6038 is used effectively to self-calibrate the system relative to the total intensity, I . The resulting Mueller matrix parameters then can be applied to subsequent observations in order to derive reliable polarimetric information for other pulsars. Flux cali-

bration to convert I and, hence, the other three Stokes parameters to a Jy scale is achieved ideally by using a noise diode and a radio source of known flux density as described in Section 7.3.3.

7.4 Various pulsar observing modes

Now we consider more routine pulsar observations, in which it is assumed that we have a well-calibrated system and suitable ephemerides with which the data can be folded to obtain pulse profiles.

7.4.1 Profile stabilisation analyses

The stability of the integrated profile is an important consideration in timing studies in which it is assumed that the integrated pulse profile has a characteristic shape once sufficient pulses have been accumulated. The simplest way to investigate profile stability is to take long integrations (preferably several thousand pulse periods) and compute the correlation coefficient between the integrated profile p and the accumulated profile a formed from the addition of n pulse periods. Deriving a is a simple extension of the folding algorithm discussed in Section 7.1 to write out the accumulated profile after the appropriate number of pulses added. Helfand *et al.* (1975) were the first to perform an analysis of this kind. Forming integrated and accumulated profiles, they examined the behaviour of $1 - \rho_r$ as a function of n , where

$$\rho_r = \frac{\sum_i (a_i - \bar{a})(p_i - \bar{p})}{\sqrt{\sum_i (a_i - \bar{a})^2} \sqrt{\sum_i (p_i - \bar{p})^2}} \quad (7.27)$$

is the familiar linear correlation coefficient (see, for example, Press *et al.* (1992)). In order to minimise the effect of off-pulse noise in this calculation, it is usual to perform this calculation over just the on-pulse bins. As noted by Helfand *et al.* (1975), we expect that $(1 - \rho_r) \propto n^{-0.5}$ for uncorrelated individual pulses. Deviations from this behaviour are common and indicate the presence of non-random behaviour from pulse to pulse, e.g. due to nulling or mode changing. As such, this simple analysis can be useful for the single-pulse studies discussed next.

7.4.2 Single-pulse analyses

Although most pulsars are weak sources, there are a significant number (of the order of 100 out of the 1600 currently known) that are strong

enough so that their individual pulses can be studied in detail. Producing single pulses from a de-dispersed time series is a simple extension of the basic folding algorithm in which the accumulated pulse profile is stored after each period. In addition to making excellent illustrations of pulsar emission behaviour (see, for example, Figs. 1.1, 1.5 and 1.6) quantitative studies of the individual pulse properties provide valuable input to theoretical models of the pulsar emission process (see Chapter 3). In the following, we outline some relevant techniques for carrying out single-pulse analyses. For the purposes of this discussion, it is convenient to represent the sampled pulses as a two-dimensional array of pulse intensity $I(j, k)$, where j denotes the pulse phase bin number and k is the pulse number, i.e. $k = 1$ denotes the first pulse, etc. Each profile has n_{bins} phase bins and there are n_{pulses} pulses in total. We shall also assume that each profile has had a DC offset subtracted, i.e. for any k , the off-pulse values of I have a zero mean.

7.4.2.1 Nulling fraction analysis

As discussed in Section 1.1.4.3, it is of interest to determine the fraction of time the pulsar spends in a null state, i.e. its *nulling fraction*, NF. Following earlier studies that used to quantify nulling from histograms of the area under the pulse (i.e. *pulse energy*; see Smith (1973)), Ritchings (1976) proposed a simple procedure that we summarise below and apply to an observation of the nulling pulsar B1944+17. This is shown in Figure 1.6, for which $\text{NF} \sim 55$ per cent (Deich *et al.* 1986). As a control experiment, we also analyse an observation of the pulsar B1933+16 for which very little nulling is observed, i.e. $\text{NF} < 0.25$ per cent.

The first step is to fold the time series and, from the resulting pulse profile, determine suitable on- and off-pulse ‘windows’, each of width W bins, denoting the starting on-pulse bin number as ON and the starting off-pulse bin number as OFF. Single pulses are then formed in the usual way and the on- and off-pulse energies E_{ON} and E_{OFF} are calculated:

$$E_{\text{ON}}(k) = \sum_{j=\text{ON}}^{\text{ON}+W-1} I(j, k) \quad (7.28)$$

$$E_{\text{OFF}}(k) = \sum_{j=\text{OFF}}^{\text{OFF}+W-1} I(j, k). \quad (7.29)$$

In order to minimise the effects of short-term variations due to scintillation (see Chapter 4), the resulting pulse energies corresponding to contiguous 2–3 min blocks of data are analysed separately. Within each

block, the mean on-pulse energy $\langle E_{\text{ON}} \rangle$ is calculated and used to normalise the individual values of E_{ON} and E_{OFF} .

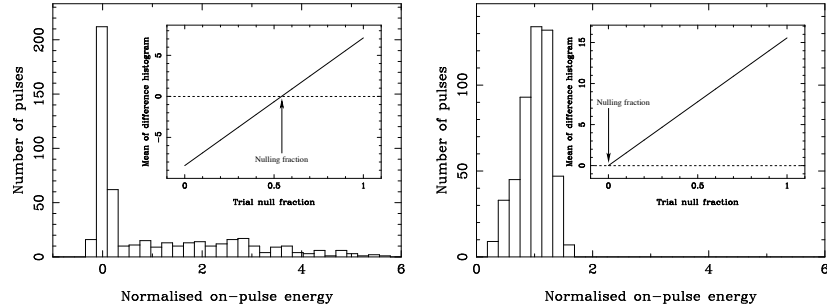


Fig. 7.6. (a) Simple nulling analysis for PSRs B1944+17; (b) B1933+16. The histograms show on-pulse distributions of pulse energy for each pulsar. The mean of the ‘residual histogram’ between the on- and off-pulse data is shown inset as a function of trial nulling fraction (see text).

Histograms of the resulting normalised on-pulse energies are shown in Figure 7.6. The on-pulse energy distribution for B1944+16 is broad and shows a clear excess at zero, indicating significant nulling. The distribution for B1933+16 is much narrower, showing no significant excess at zero. In order to calculate the nulling fraction, we need to account for the contribution of the system noise in these histograms. The on-pulse distributions represent the distribution of the pulse intensities convolved with the system noise. The off-pulse data represent just the probability distribution of the system noise. Although in principle a Fourier deconvolution technique could be used to recover the true on-pulse distribution, it is sufficient, following Ritchings (1976), simply to subtract the off-pulse histogram from the on-pulse histogram. The resulting ‘residual histogram’ accounts for the sensitivity limit caused by noise in the observing system.

For an extreme nulling pulsar with $\text{NF} \sim 100$ per cent, the residual histogram would be smooth and continuous with a zero mean. This is not the case for either pulsar, and we need to adjust the fraction of the noise distribution that we subtract from the on-pulse distribution until the mean of the residual histogram is zero. In the case of B1933+16, and as shown in Figure 7.6, the fraction of the noise distribution subtracted indicates that $\text{NF} \sim 0$ as expected. For significant nulling pulsars like B1944+17, we can place a lower limit on NF by reducing the fraction of the subtracted noise distribution until the mean of the residual his-

togram again deviates from zero. From the plot of shown in Figure 7.6, we find $\text{NF} \sim 55$ per cent, in excellent agreement with Deich *et al.* (1986).

7.4.2.2 Microstructure analyses

As mentioned in Chapter 1, single pulses reveal structure on microsecond and even smaller timescales when studied with sufficient time resolution. In analyses of such microstructure, we are interested primarily in establishing: (a) whether any periodicities are present; (b) a characteristic timescale for the micropulses. Now we outline the techniques to measure these quantities starting from our two-dimensional array $I(j, k)$ defined above, where j is the pulse phase bin and k is the pulse number.

A typical microstructure analysis is shown in Figure 7.7. It is of particular interest to identify and quantify any periodicities and characteristic timescales of micropulses present in the data. From each high-resolution single pulse, the first step (see, for example, Hankins (1972)) is to form the autocorrelation function (ACF). In general, the ACF of the k^{th} pulse

$$\text{ACF}(k, l) = K_k \sum_{j=1}^{n_{\text{bins}}} I(j, k)I(j + l, k), \quad (7.30)$$

where l is the lag and K_k is a normalising constant, usually chosen such that $\text{ACF}(k, 0) = 1$ as shown in Figure 7.7(a).

In order to quantify any periodicities present, the power spectrum of the data (PSD) is usually calculated. Given the ACF, it follows from the autocorrelation theorem (see, for example, Bracewell (1998)) that the PSD of a given pulse is simply the Fourier transform of its ACF. As shown in Figure 7.7(b), the PSD identifies a clear peak in the data with a fluctuation frequency of 2 kHz. Lange *et al.* (1998) introduced a more sensitive means of identifying periodicities by Fourier-transforming the time derivative of the ACF and forming its power spectrum. The advantage of this resulting quantity, known as the ACF derivative power spectrum or ADP, is that low-level features present often can be masked by the overall slope of the ACF. Taking the time derivative before the Fourier transform effectively removes the slope. Figure 7.7(d) shows the ADP as a function of fluctuation frequency and identifies the 2 kHz periodicity with greater significance. As shown by, for example, Cordes *et al.* (1990), these quasi-periodicities are not stable and vary from pulse to pulse. Often it is useful to investigate this behaviour via a histogram of periodicities identified from PSDs or ADPs of individual pulses.

In order to determine the timescale for microstructure, following Hankins (1972), it is standard practice to plot the average ACF over all

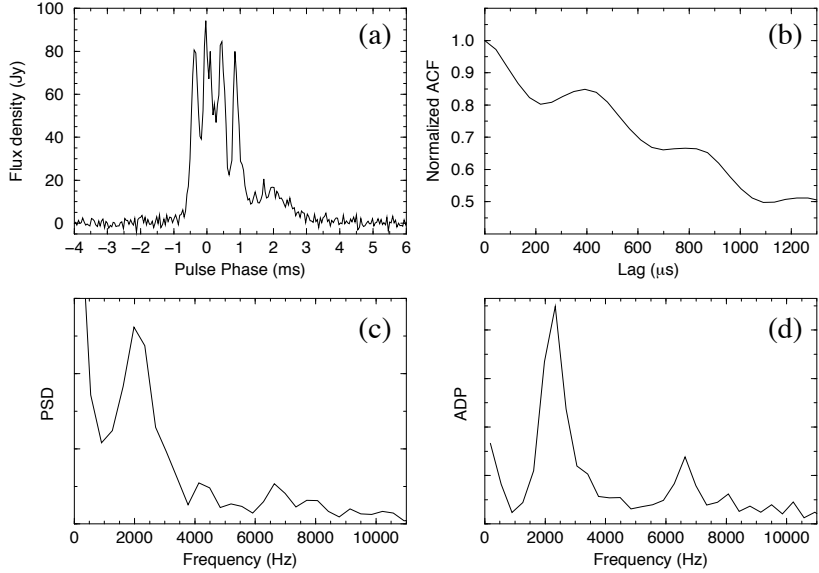


Fig. 7.7. Examples of microstructure analyses for a single pulse from the Vela pulsar (Kramer *et al.* 2002) shown in panel (a). Panels (b), (c) and (d) show respectively the ACF, PSD and ADP of the pulse (see text).

pulses. The average ACF typically is made up of two straight-line components with a characteristic break-point or flattening which represents the typical duration (i.e. width) of the micropulses (Rickett *et al.* 1975) and is defined to be the microstructure timescale. Lange *et al.* (1998) proposed an extension of this simple approach, known as the ‘turn-off point method’, that searches automatically for changes in the slope due to flattening (see Appendix A of Lange *et al.* (1998) for details of this procedure).

We note in passing that in low-frequency microstructure analyses (see, for example, Kuzmin *et al.* (2003)) multiple breaks are observed in the ACFs due to other effects, e.g. digitisation and sky background variations across the band. In order to identify the intrinsic microstructure timescale in these cases, Kuzmin *et al.* (2003) form the ACFs of on- and off-pulse regions separately and take the difference of the two functions to subtract the instrumental effects common to both regions. The only remaining features are due then to the intrinsic timescale of the microstructure.

7.4.2.3 Drifting subpulse analyses

The highly ordered structure of the drifting subpulses discussed in Chapter 1 (see, for example, Figure 1.6) clearly is a phenomenon that needs to be explained by any viable emission process. As shown schematically in Figure 1.6, in addition to the pulse period $P = P_1$, we identify the characteristic spacing between sub-pulses, P_2 , and the period at which a pattern of pulses crosses the pulse window, P_3 . Now we discuss briefly ways in which P_2 and P_3 can be determined.

For P_2 , Sieber and Oster (1975) devised a method in which successive pulses $I(j, k)$ and $I(j + l, k + 1)$ were cross-correlated as a function of different phase lags l . The resulting correlation coefficients then are averaged over all pulses, and a plot of correlation coefficient versus l reveals two peaks separated in phase by P_2 . The classical determination of P_3 was pioneered by Backer (1970b). In this scheme, data are selected in the same phase bin of each of the individual pulses to form a time series at a fixed pulse longitude. A straightforward one-dimensional Fourier transform (see, for example, Section 6.1.3) of this time series can be applied to form the power spectrum as a function of cycles per pulse period (C/P_1). This so-called *fluctuation spectrum* may be averaged over a range of pulse longitudes to increase S/N if desired. The fluctuation spectrum shows three main features: (a) a strong low-frequency ‘red-noise’ component caused by a combination of interstellar scintillation, receiver fluctuations and intrinsic variations in intensity; (b) a constant ‘white noise’ component corresponding to independent pulse-to-pulse fluctuations; (c) spectral features at $1/P_3$ and harmonics thereof caused by the drifting sub-pulses.

Advances in computational power now favour two-dimensional analyses to determine P_2 and P_3 simultaneously. Two related techniques have recently been proposed: (a) the harmonic-resolved fluctuation spectrum method of Deshpande and Rankin (1999; 2001); (b) the two-dimensional fluctuation spectrum approach of Edwards and Stappers (2002). As pointed out by the latter authors, both techniques are equivalent. The two-dimensional fluctuation spectrum \mathcal{S} is simply the power spectrum of the two-dimensional Fourier transform, i.e.

$$\mathcal{S}(u, v) = \left| \frac{1}{K} \sum_{j=0}^{n_{\text{bins}}-1} \sum_{k=0}^{n_{\text{pulses}}-1} I(j, k) \exp[-2\pi i(uj + vk)] \right|^2, \quad (7.31)$$

where the normalisation factor $K = n_{\text{bins}} \times n_{\text{pulses}}$, u is in cycles per radian of pulse longitude and, as for the one-dimensional fluctuation

spectrum, v is in cycles per pulse period. The signature of P_2 is detectable in u as harmonics of $P_1/(2\pi P_2)$, while P_3 shows up in v as harmonics spaced by $1/P_3$ as before.

7.4.3 Polarisation profiles

In addition to total intensity, Stokes' I , we have three further profiles: Stokes' Q , U and V . Following the application of a polarisation calibration procedure such as the one outlined in Section 7.3.4, we can dedisperse and fold all four Stokes parameters separately. It is customary usually to display total intensity, I , circular polarisation V , linear polarisation $L = \sqrt{Q^2 + U^2}$ and the associated position angle $\Psi = \frac{1}{2} \arctan(\frac{U}{Q})$.

7.4.3.1 Considerations for linear polarisation

While the individual Stokes parameters are observed to follow Gaussian noise statistics with standard deviations σ_I , σ_U , σ_V and σ_Q , this is not true for the linearly polarised intensity, L . Due to the quadrature summation $L = \sqrt{Q^2 + U^2}$, the probability density function of L is non-Gaussian (see below). In addition, there exists a positive bias in the measured values at low L (see, for example, Wardle and Kronberg (1974)). In the extreme case, in which L is zero, we may infer erroneously a non-zero value simply from the quadrature sum of the noise in U and Q ! Following Everett and Weisberg (2001), we recommend the following correction scheme to remove the bias and calculate the true value of linear polarisation:

$$L_{\text{true}} = \begin{cases} \sigma_I \left[\left(\frac{L}{\sigma_I} \right)^2 - 1 \right]^{\frac{1}{2}} & \text{if } \left(\frac{L}{\sigma_I} \right) \geq 1.57 \\ 0 & \text{otherwise,} \end{cases} \quad (7.32)$$

where σ_I is the off-pulse standard deviation in Stokes' I .

Similarly, the probability density function of the linear polarisation angle about the true value Ψ_{true} is not a Gaussian distribution. As a consequence, the uncertainty in this angle σ_Ψ does not follow strictly the simple result derived from Gaussian error propagation:

$$\sigma_\Psi = 28.65^\circ \left(\frac{\sigma_I}{L_{\text{true}}} \right). \quad (7.33)$$

This is only useful when $L_{\text{true}}/\sigma_I \gtrsim 10$. For lower values of L , following

Everett and Weisberg (2001), we recommend use of the correct probability density function for Ψ . After Naghizadeh-Khouei and Clarke (1993), this is given by

$$G(\Psi) = \frac{\exp(-L_{\text{true}}^2/2\sigma_I^2)}{\sqrt{\pi}} \left(\frac{1}{\sqrt{\pi}} + \eta \exp(\eta^2)[1 + \text{erf}(\eta)] \right), \quad (7.34)$$

where $\eta = L_{\text{true}} \cos 2(\Psi - \Psi_{\text{true}})/(\sqrt{2}\sigma_I)$ and the error function $\text{erf}(x) = (2/\sqrt{\pi}) \int_0^x \exp(-x^2) dx$. To derive a ‘1- σ ’ uncertainty σ_Ψ , we need to integrate numerically $G(\Psi)$ to encompass 68.26 per cent of the total area about the peak value. Everett and Weisberg (2001) recommend that this is carried out for values of Ψ where $L_{\text{true}}/\sigma_I < 10$. For more significant detections, Equation (7.33) may be used. This procedure is particularly useful when fitting the position angle data as described next.

7.4.3.2 Fits to the rotating vector model

As discussed in Chapter 3, the rotating vector model of Radhakrishnan and Cooke (1969) predicts the following relationship between the position angle of linear polarisation Ψ and pulse phase ϕ :

$$\tan(\Psi - \Psi_0) = \frac{\sin \alpha \sin(\phi - \phi_0)}{\sin(\alpha + \beta) \cos \alpha - \cos(\alpha + \beta) \sin \alpha \cos(\phi - \phi_0)}, \quad (7.35)$$

where α is the angle between the rotation and magnetic axes and the ‘impact parameter’ β is the angle between the line of sight and the centre of the emission beam (see Section 3.4.4 for further details).

Fits of the position angle swing predicted by this function to the observed values therefore offer a way to determine a pulsar’s beam geometry. Again, following Everett and Weisberg (2001), we recommend that care should be taken to weight appropriately the position angles by the uncertainties estimated above. With this in mind, two important additional caveats should be noted: (a) as mentioned in Chapter 1, the position angle data do not always follow the predicted model; (b) even if a statistically good fit is obtained, the often narrow pulses mean that only a small range of pulse longitude is sampled and therefore α and β can be highly covariant. Further details can be found in Section 3.4.4. Software to perform these fits on appropriately calibrated pulse profiles is available on the book web site (see Appendix 3).

7.4.3.3 Faraday rotation measurements

As discussed in detail in Chapter 4, the magnetic field of our Galaxy acts effectively as a Faraday screen that rotates the position angle of

linear polarisation of the pulsar signal by an amount proportional to the square of the observing wavelength. The constant of proportionality, known as the *rotation measure* (RM) is the integral of the component of the Galactic magnetic field along the line of sight to the pulsar weighted by electron density (see Equation (4.13)).

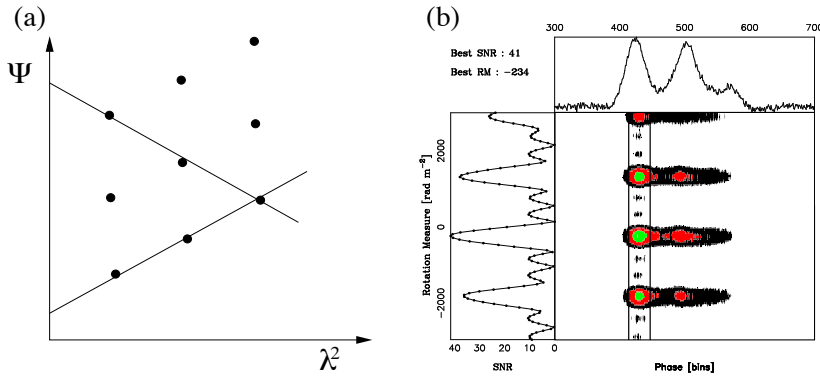


Fig. 7.8. (a) Schematic showing how position angle ambiguities may lead to an incorrect determination of RM. (b) A search for RM by maximising the linearly polarised profile. Figure provided by Dipanjan Mitra.

Measurements of RM are carried out in two main ways. The simplest approach (see, for example, Rand and Lyne (1994)) is to calculate the linearly polarised flux L in each bin of the pulse profile as described in Section 7.4.3.1. For values of L that exceed the standard deviation of the off-pulse noise σ_L by a certain amount (usually 3–5 times σ_L), the mean value of Ψ is calculated from the vector addition of the linear polarisation across the pulse. Each vector in this sum has components U and Q and is weighted by its S/N in L , i.e. L/σ_L . For bright pulsars, multiple measurements of Ψ as a function of frequency may be possible by splitting the band into several sub-bands and measuring the mean value of Ψ in each band. For fainter pulsars, measurements at multiple frequencies are required. In both cases, RM is derived by fitting to

$$\Psi(\lambda) = \Psi_\infty + \text{RM} \lambda^2, \quad (7.36)$$

where Ψ_∞ is the position angle at infinite frequency. Since, by definition, Ψ is periodic on π rather than 2π , care should be taken to ensure that the frequency spacing is not too large so that position angle ambiguities lead to an incorrect value of RM coming from the fit, as shown in Figure 7.8a.

The second technique, shown in Figure 7.8b, is to perform a search

in RM by splitting the band into a number of independent frequency channels that are phase-rotated separately in U and Q before combining to form the average profile in L over the whole band. Rather like the DM search discussed in Chapter 6, a plot of S/N for the resulting L profile versus trial RM should show a maximum at the true value. This method gives consistent results with the simple $\Psi - \lambda$ fit, but with the advantage that it can be applied to weaker pulsars in which S/N prohibits use of the first approach. For further details, see, for example, Mitra *et al.* (2003).

7.4.4 Measuring scintillation parameters

As described in Chapter 4, the observed intensity variations of pulsars tell us much about the structure of the interstellar medium. Here we explain how to measure the basic scintillation parameters.

7.4.4.1 Creating a dynamic spectrum

The characteristic time and frequency scales due to diffractive interstellar scintillation, Δt_{DISS} and Δf_{DISS} , often can be resolved by a single observation with good frequency resolution by forming the *dynamic spectrum* – a two-dimensional image of pulse intensity as a function of observation time and frequency. In order to create a dynamic spectrum, all the individual frequency channels are folded separately and accumulated pulse profiles representing contiguous sub-integrations are saved. The length of each sub-integration depends on the available S/N, but ideally should be ~ 30 s in order to resolve scintillation structure on short timescales. Here, only the relative intensity is of interest, and it is sufficient to calculate the area under the pulse and subtract the mean of the off-pulse emission. The resulting two-dimensional array represents pulse energy as a function of observation frequency f and time t , i.e. $E(f, t)$. An example spectrum is shown in Figure 7.9 for PSR B0834+06.

Although often discernible by eye from the dynamic spectrum, Δf_{DISS} and Δt_{DISS} are more robustly obtained from a two-dimensional autocorrelation analysis. Following Cordes (1986), we first compute the covariance function

$$\text{CF}(\Delta f, \tau) = \sum_{f=1}^{n_f - |\Delta f|} \sum_{t=1}^{n_t - |\tau|} E(f, t)E(f + \Delta f, t + \tau), \quad (7.37)$$

where n_f is the number of frequency channels, n_t is the number of subintegrations and f and t are integer values in the range $1 < f < n_f$ and

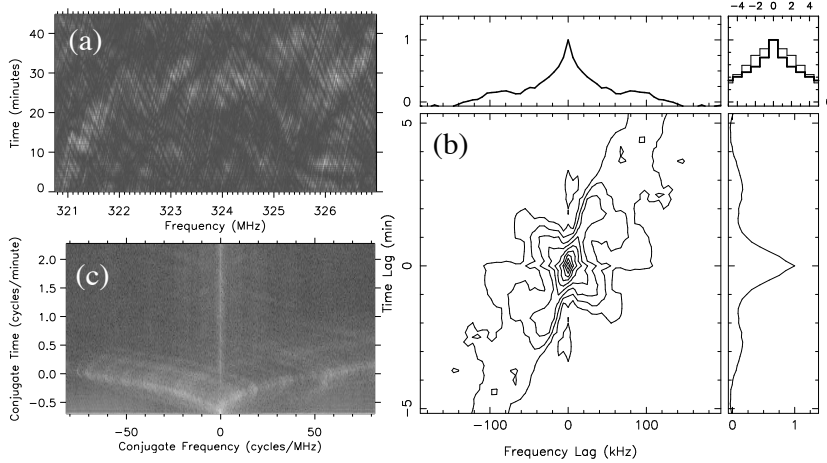


Fig. 7.9. (a) Dynamic spectrum for a 324 MHz observation of PSR B0834+06. (b) Autocorrelation analysis showing the characteristic scintillation timescale and bandwidth. (c) Secondary spectrum of the data showing symmetric arc-like features. Data and analysis provided by Maura McLaughlin.

$1 < t < n_t$. Likewise, the frequency and time lags are integers in the range $-n_f/2 < \Delta f < n_f/2$ and $-n_t/2 < \tau < n_t/2$. The autocorrelation function (ACF) then is just the covariance function normalised by the zero-lag in both time and frequency, i.e.

$$\text{ACF}(\Delta f, \tau) = \frac{\text{CF}(\Delta f, \tau)}{\text{CF}(0, 0)}. \quad (7.38)$$

In practice, care should be taken to exclude parts of the dynamic spectrum corrupted by occasional bursts of interference, or where no pulses are present due to nulling. The bandwidth and timescale Δf_{DISS} and Δt_{DISS} are then determined by fitting a two-dimensional Gaussian function to the ACF. Following Cordes (1986), the standard practice is to measure Δf_{DISS} as the half width at $\text{ACF}(\Delta f, 0)/2$, and Δt_{DISS} as the half width at $\text{ACF}(0, \tau)/e$. From such an analysis of the data for PSR B0834+06 in Figure 7.9, we infer $\Delta f_{\text{DISS}} = 42$ kHz and $\Delta t_{\text{DISS}} = 87$ s.

Recalling the relationship from Chapter 4, we can infer the scintillation speed V_{ISS} from these measurements

$$V_{\text{ISS}} = A \left(\frac{d}{\text{kpc}} \right)^{1/2} \left(\frac{\Delta f_{\text{DISS}}}{\text{MHz}} \right)^{1/2} \left(\frac{f}{\text{GHz}} \right)^{-1} \left(\frac{\Delta t_{\text{DISS}}}{\text{s}} \right)^{-1}, \quad (7.39)$$

where d is the distance to the pulsar and the constant A depends on the

geometry, location of the scattering screen and form of the turbulence spectrum. For this choice of units, $A = 3.85 \times 10^4 \text{ km s}^{-1}$ (Gupta 1995) or $2.53 \times 10^4 \text{ km s}^{-1}$ (Cordes & Rickett 1998). Adopting the latter value for the data shown in Figure 7.9, we find $V_{\text{ISS}} = 148 \text{ km s}^{-1}$ for a dispersion measure based distance $d = 0.65 \text{ kpc}$.

7.4.4.2 Application to binary pulsars

An elegant application of the dynamic spectrum is to track the changing orbital velocity of a binary pulsar viewed on the plane of the sky as a change in the scintillation pattern as a function of orbital phase. This was first devised by Lyne (1984) who applied it to dynamic spectra of the binary pulsar B0655+64 in order to determine its velocity and the inclination angle between the plane of the orbit and the plane of the sky. Now we outline briefly this technique, closely following the more detailed description given by Ord *et al.* (2002a).

We begin by assuming that we have a dynamic spectrum from which we can obtain measurements of V_{ISS} as described above at regular intervals across the orbit. Then we construct a graph of V_{ISS} versus orbital phase. For the purposes of the model, it is convenient to display orbital phase in terms of true orbital anomaly A_T , rather than mean anomaly (see Section 8.3.1.1 for details of computing A_T). The model scintillation speed $V_{\text{ISS}}^{\text{model}}$ is the sum of two orthogonal components:

$$V_{\text{ISS}}^{\text{model}} = \kappa \sqrt{V_1^2 + V_2^2}, \quad (7.40)$$

where κ is a free parameter reflecting the uncertainties in the scattering geometry and the terms

$$V_1 = (V_r \cos \phi - V_A \sin \phi) + V_{\parallel} \quad (7.41)$$

$$V_2 = (V_A \cos \phi + V_r \sin \phi) - V_{\perp} \quad (7.42)$$

relate the radial component of the *orbital* velocity V_r in the direction of the focus of the orbital ellipse, its perpendicular component V_A and the components of the pulsar's *space* velocity along and perpendicular to the line of nodes (see Section 8.3.1), respectively V_{\parallel} and V_{\perp} . The orbital phase $\phi = \omega + A_T$ is measured with respect to the ascending node, where ω is the longitude of periastron. (See Section 8.3.1 and in particular Figure 8.3 for definitions of the various angles.) In this framework, the orbital velocity components are

$$V_r = V_{\text{orb}} e \sin A_T \quad \text{and} \quad V_A = V_{\text{orb}} (1 + e \cos A_T), \quad (7.43)$$

where

$$V_{\text{orb}} = \frac{2\pi xc}{\sin i \sqrt{(1-e^2)} P_b} \quad (7.44)$$

is the mean orbital velocity expressed in terms of observables and the unknown inclination angle i to be determined. The observables are orbital eccentricity e , projected semi-major axis of the orbit x in light seconds, and the orbital period P_b (see Section 8.3.1.1).

The geometrical model above provides a description of V_{ISS} in terms of five free parameters: κ , i , ω , V_{\parallel} and V_{\perp} . In practice, ω should be known already to high precision along with the other Keplerian parameters P_b , x and e from timing measurements (Chapter 8). As noted by Lyne (1984), fits of this model to the data cannot distinguish between the case of a fast-moving pulsar in an orbit viewed nearly edge on, and a slow-moving pulsar in a more face-on orbit. As a result, two degenerate solutions for different values of i are obtained.

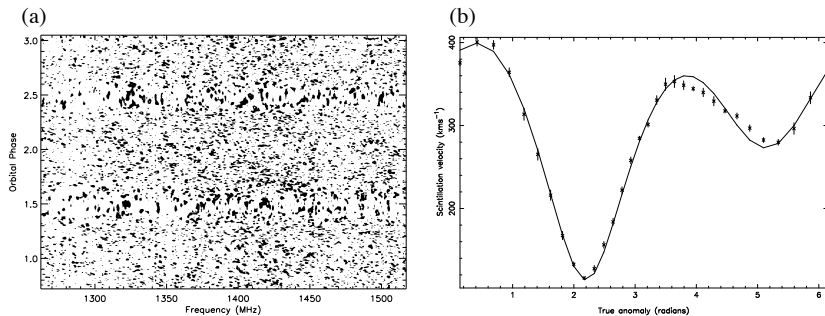


Fig. 7.10. (a) Dynamic spectrum for the relativistic binary pulsar J1141–6545 (Ord *et al.* 2002a). The change in relative speed of the pulsar due to its orbital motion stretches and condenses the scintillation timescales. (b) Model fit to the observed scintillation speeds as a function of true anomaly. Figure provided by Steve Ord.

A stunning application of this technique, as applied recently to the relativistic binary J1141–6545 by Ord *et al.* (2002a), is shown in Figure 7.10. In this case, the more edge-on solution ($i = 76 \pm 3^\circ$) is favoured, since the implied pulsar mass ($1.29 M_\odot$) is more in line with neutron star mass measurements (Thorsett & Chakrabarty 1999). The implied transverse component of the binary system’s space velocity $V_T = \sqrt{V_{\perp}^2 + V_{\parallel}^2} \sim 115 \text{ km s}^{-1}$ supports the notion that the neutron star received a ‘kick’ during its formation in a supernova. Subsequent timing

observations (Bailes *et al.* 2003) provide an independent confirmation of this more edge-on solution. Similarly, Ransom *et al.* (2004) have applied this technique to PSR J0737–3039A.

7.4.4.3 Secondary spectrum

In some cases, as for the data in Figure 7.9, a ‘criss-cross’ pattern of fringes can be seen in the dynamic spectrum. In order to investigate these structures in more detail, following Cordes and Wolszczan (1986), we can form the *secondary spectrum* by taking the two-dimensional Fourier transform of the dynamic spectrum. When viewed as a grey-scale image in the conjugate frequency ($\mathcal{F} = 1/f$) and conjugate time ($\mathcal{T} = 1/t$) plane, one often sees beautiful parabolic arc-like features as shown in Figure 7.9.

As pointed out by Stinebring *et al.* (2001), the curvature of these *scintillation arcs*, in the simple thin-screen model for scintillation introduced in Chapter 4, is a function of the location of the screen between the observer and the pulsar. When the scintillation pattern is dominated by V_{ISS} , Stinebring *et al.* (2001) find that

$$\mathcal{F} = \frac{\lambda^2 d}{2cV_{\text{ISS}}^2} \left(\frac{s}{1-s} \right) \mathcal{T}^2, \quad (7.45)$$

where s is the distance to the screen expressed as a fraction of d , λ is the observing wavelength and c is the speed of light. For pulsars for which d and V are known or constrained from proper motion and parallax measurements, a measurement of arc curvature can be used to infer the effective distance to the scattering screen.

7.4.5 Neutral hydrogen measurements of pulsar distances

As mentioned in Chapter 1, one way of constraining the distances to pulsars is by measuring absorption and emission features caused by the neutral hydrogen (HI) distribution along the line of sight. This technique was pioneered by Guelin *et al.* (1969) and is shown schematically in Figure 7.11. The aim of the observation is to detect *absorption by a region of HI in front of the pulsar and emission from HI behind the pulsar with no corresponding absorption*. As with all spectral-line astronomy, the detected frequencies are Doppler-shifted from their rest-frame values by differential motion between the source and the observer. The relative velocity therefore can be inferred directly from the observed frequency of the line. The frequency shift, for these observations, is dominated by

differential Galactic rotation. Hence, using a model Galactic rotation curve, the inferred velocities of the absorption and emission features can be converted to distances along the line of sight that correspond to lower and upper bounds on the pulsar distance.

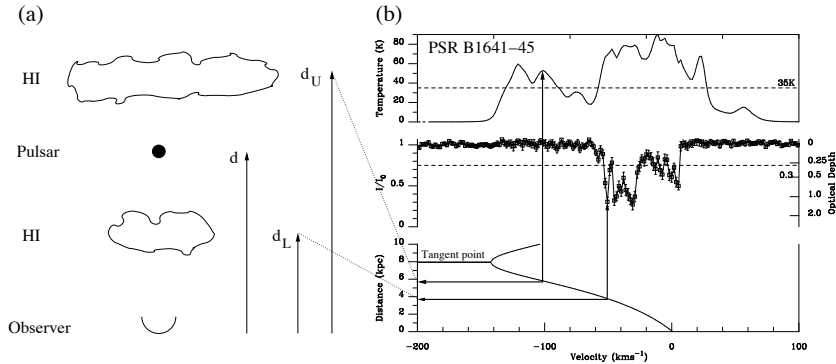


Fig. 7.11. (a) Schematic showing a pulsar bounded by regions of HI. (b) HI emission (top) and absorption (middle) spectra towards the pulsar B1641–45 (Ord *et al.* 2002b). The lower panel shows the expected velocity assuming the Galactic rotation curve of Fich, Blitz and Stark (1989). Figure adapted from the original spectrum provided by Steve Ord.

From Figure 7.11, we note that the sizes of typical spectral features are a few km s⁻¹ while the range of velocities is 250 km s⁻¹. For the HI rest frequency (1420.406 MHz), we note that $1 \text{ km s}^{-1} \equiv 4.74 \text{ kHz}$. Hence, this velocity range corresponds to a total bandwidth of just under 1.2 MHz which needs to be covered with good spectral resolution (10 kHz or better). This type of observation therefore is ideal for a narrow-band correlator or software filterbank (see Chapter 5).

The very nature of pulsars makes them particularly well suited to spectral line observations, since their on- and off-pulse regions can be used to derive on- and off-source spectra. In practice, the data are folded modulo the predicted pulse period and spectra are accumulated into a number of phase bins. The width of these bins is chosen usually so that the on-pulse emission occupies several phase bins. Each bin is weighted according to its S/N ratio (see, for example, Koribalski *et al.* (1995)).

The resulting spectra in the off-pulse bins normally are averaged to form a single HI emission spectrum as shown in the upper panel of Figure 7.11. The integral under this curve gives the total HI column density along the line of sight, N_{HI} . In the usual optically thin approximation

(see, for example, Rohlfs and Wilson (2000)):

$$N_{\text{HI}} = 1.8 \times 10^{18} \int_{-\infty}^{+\infty} T_{\text{B}}(v) \, dv \, \text{cm}^{-2}, \quad (7.46)$$

where v (km s $^{-1}$) is the relative velocity and the brightness temperature T_{B} (K) can be related directly to the spin temperature of the HI emission. Conversion of the initially uncalibrated ordinate axis to a brightness temperature usually is achieved by normalising the area under the spectrum to N_{HI} determined from dedicated Galactic HI surveys for the particular line of sight (see, for example, Weaver and Williams (1973) and Kerr *et al.* (1986)). The error in T_{B} using this approach is about 5 K (Koribalski *et al.* 1995). The middle panel of Figure 7.11 is the difference between the on- and off-pulse spectra normalised by the pulsar's intensity I_0 . This represents the HI absorbed by clouds in between the observer and the pulsar. An absorbed feature I relative to I_0 also can be expressed in terms of the optical depth $\tau = -\ln(I/I_0)$.

Some care should be taken when interpreting distance bounds from emission and absorption spectra. Frail and Weisberg (1990) recommend setting the lower distance limit from the centre of the farthest absorption feature with $\tau > 0.3$ and the upper distance limit from the first emission peak with $T_{\text{B}} > 35\text{K}$. As shown by Weisberg *et al.* (1979), the reason for this choice is that HI emission features with $T_{\text{B}} > 35$ K rarely result in optical depths less than 0.3 at the corresponding point in the absorption spectrum. Adopting this procedure for the example spectra for PSR B1641–45 shown in Figure 7.11 and applying the rotation curve of Fich, Blitz and Stark (1989), we find $d = 4 \pm 1$ kpc.

While we have considered an almost ‘text-book’ example for the HI technique, several caveats are worth noting for less clear-cut cases: (a) both emission and absorption features are not always detectable, so that only upper or lower bounds may be possible (for examples, see Koribalski *et al.* (1995)); (b) Galactic rotation curves do not account for random streaming motions of the HI – this results in an uncertainty of about 7 km s $^{-1}$, which should be taken into account when using the rotation curves to convert to distance bounds; (c) care should be taken when combining spectra from two polarisations to make sure that the spectra are appropriately weighted by their S/N ratio. These issues are discussed further by Frail and Weisberg (1990).

7.5 Interference excision

As for the search observations discussed in Chapter 6, radio-frequency interference (RFI) is an ever-increasing problem for routine pulsar observations. However, with some care, the effects of RFI on the data can be minimised to a large extent. One example of this is shown in Figure 7.12, a 29 min observation of the relativistic binary B1534+12 by Stairs *et al.* (2000a) which shows numerous bursts of RFI. Since the pulse is generally much weaker than the interference, it is clearly affected by the bursts that modulate the baseline of the integrated pulse profile.

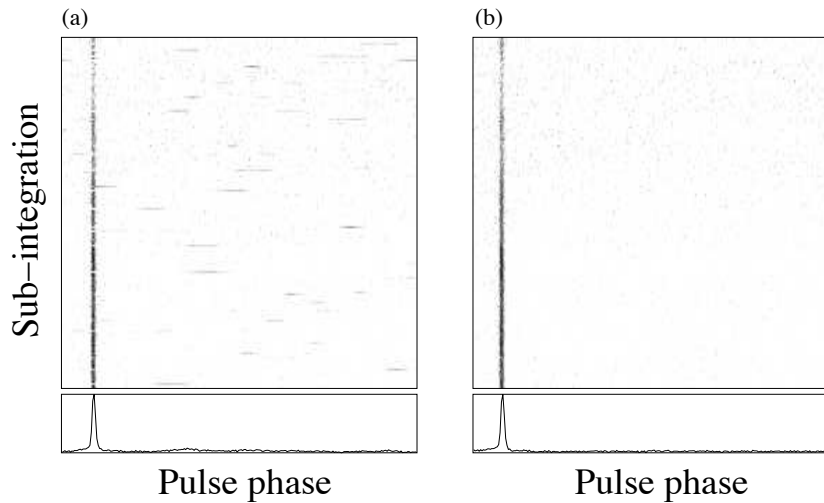


Fig. 7.12. (a) Integrated pulse profile and 10 s sub-integrations for an observation of PSR B1534+12. The raw data are clearly affected by intermittent bursts of RFI at random pulse phases. (b) The same data after including a broad-band excision scheme (see text). The baseline of the integrated pulse profile is significantly flatter and the profile S/N ratio is increased. Figure provided by Ingrid Stairs.

This type of interference (strong, short-duration bursts) is relatively easy to excise by keeping track of the statistics of the de-dispersed time series. Useful quantities are the mean, median and standard deviation, σ of short segments of data. Bursts of RFI will show up as significant differences between the mean and median in noisy segments. In the example shown in Figure 7.12, Stairs *et al.* (2000a) employed a simple algorithm which excised short blocks of data if: (a) an individual sample exceeded the median by 30σ ; (b) a number of bins exceeded the median by 15σ ; (c) the median power of a block exceeded the running median

of previous blocks by 10 per cent. The result of excising blocks of data in this way are shown on the right-hand side of Figure 7.12 and show a clear improvement in data quality.

The above example was a broad-band excision scheme. It is often well worth checking individual frequency channels in a similar way to excise narrow-band features. In some cases, rejecting only a small fraction of the total band can result in dramatic improvements in data quality. Since no single RFI excision algorithm is guaranteed to work, experimentation is required to optimise the rejection scheme.

7.6 Further reading

We have attempted in this chapter to review the most commonly used techniques encountered in single-dish observations of pulsars. We have placed, where possible, the emphasis on areas not commonly covered in the literature, e.g. pulse profile statistics, confirmation observations and period optimisation issues. On more conventional areas, some overlap can be found in the reviews by Hankins and Rickett (1975), Bhattacharya (1998) and Cordes (2002). Calibration of pulsar polarimetry is discussed in detail by a number of authors, including Stinebring *et al.* (1984), Xilouris (1991), Britton (2000) and Johnston (2002). Our treatment closely followed the recent work by Heiles *et al.* (2001). An excellent introduction to polarimetry in general can be found in Heiles (2002).

Further discussion on single-pulse techniques can be found in Backer (1973), Ritchings (1976), Deshpande and Rankin (1999; 2001) and Edwards and Stappers (2002). The careful study of Everett and Weisberg (2001) provides a good starting-point for further information about polarimetry analyses. Likewise, the papers by Rand and Lyne (1994) and Mitra *et al.* (2003) should be consulted for further discussions of rotation measure determinations. Much of the techniques concerning scintillation speed measurements were pioneered by Lyne and Smith (1982). A more detailed reference can be found in Cordes (1986), while Stinebring *et al.* (2001) discuss scintillation arcs in more detail. An excellent review of neutron hydrogen measurements can be found in Frail and Weisberg (1990). Further discussion is also given in Koribalski *et al.* (1995).

7.7 Available resources

A number of useful resources are available via the book web site (see Appendix 3) for the analysis of pulsar observations. Most data analysis routines rely on programs to fold and de-disperse the often significant amounts of data. A number of such programs are freely available as part of the SIGPROC, PRESTO and PSRCHIVE packages (Lorimer (2001), Ransom (2001) and Hotan *et al.* (2004), respectively) are now capable of reading raw data in a variety of formats. All these packages require the TEMPO timing program (see Chapter 8) to produce sets of polynomial coefficients (known as *polyco* files) in their period calculations. In order to enhance the functionality of TEMPO, the web site contains a number of useful scripts to generate, read and interpret polyco files. This includes a particularly useful utility to convert topocentric pulse periods and epochs to the equivalent values at the SSB. Software to fit barycentric periods and epochs to a binary model ephemeris are also available, as are packages to perform some of the basic single-pulse and polarisation analyses discussed in Section 7.4. These are part of the European Pulsar Network (EPN) software package designed to work on any pulse profiles in EPN format (Lorimer *et al.* 1998).